

Department of Pure and Applied Chemistry

**DEVELOPMENT OF GOLD
SUPRAPARTICLES FOR
NANOMEDICINE APPLICATIONS
BY
SUREYYA PATERSON**

A thesis submitted to the Department of Pure and Applied Chemistry, University of Strathclyde, in part fulfilment of the regulations for the degree of Doctor of Philosophy in Chemistry.


NOVEMBER 2018

Declaration

This thesis is the result of the author's original research. It has been composed by the author and has not been previously submitted for examination which has led to the award of a degree.

The copyright of the thesis belongs to the authors under the terms of the United Kingdom Copyright Acts as qualified by University of Strathclyde Regulation 3.50. Due acknowledgement must always be made of the use of any material contained in/or derived from this thesis.

Signed:

A handwritten signature in black ink, appearing to read 'W. Kelly', is written over a light blue grid background. The signature is stylized with large loops and a long horizontal stroke extending to the right.

Date: 15/01/2019

Sometimes I lie awake at night, and I ask, "Where have I gone wrong?"

Then a voice says to me, "This is going to take more than one night."

- Charles M. Schulz

Acknowledgements

Firstly, I would like to thank my supervisor Prof. Duncan Graham for the opportunity to allow me to continue exploring such an engaging field. Thank you for providing me with support and guidance over the years. I would also like to thank Dr. Roberto de la Rica for his advice and valued knowledge throughout the years and the opportunity to do a PhD. I would like to extend a special thanks to Prof Rein. Ulijn for his continued guidance and the amazing opportunity to live in New York and allowing me to use all the amazing facilities within the ASRC.

Secondly, I would like to thank Prof. Karen Faulds and Dr. Alistair Wark for providing me with help and advice throughout the years. I would like to thank Dr. Sharon Kelly from the University of Glasgow for allowing me to use the CD instrumentation.

Next, I would like to thank everyone in the Centre for molecular nanometrology, old and new, who have made the past 3 years so much fun and exciting. Special thanks to Dr Lauren Jamieson, the other Post-Docs, Steve, Hayleigh and Stacey, and Corinna for all your help and to Rachael, Emma, Iona, Kirsty, Alex and Jenny for their constant support of listening to me and the continuous supply of drinks, food and Ark nights. To Fay for always having someone who understands and being there and to Craig for endless gins, polo nights and being the best GBF.

I would also like to extend a thanks to Dr. Matt Baker for letting me to use the IR and the Baker group especially Angela and Holly for putting up with my constant moaning, questions and providing me with endless coffee, cake and chat. I would also like to thank members of the Ulijn group and Dr. Jugal Sahoo for all your help and to Mari and Ines who took me in with open arms.

I would like to also show my gratitude to Sam who has had to put up with my endless mood swings throughout the years and has helped me with everything from experiments and setting up instruments to listening to my woes. I could not have completed this without you and I am hugely grateful for your continued support and encouragement.

Last but not least I would like to dedicate this thesis to my parents who have always believed in me and provided me with unconditional love and support throughout all my degrees. Thank you for always being there for me through difficult times this would not have been possible without you.

Abstract

Gold nanoparticles are widely used in bionanotechnology due to their unique optical properties and ease of surface modification with biomolecules. By assembling these gold nanoparticles into ordered structures their physiochemical properties can be fine-tuned. Gold nanoparticle assemblies have shown a remarkable increase in surface enhanced Raman signals (SERS) which can be further used for biological sensing applications. In addition, their efficient conversion of light to heat energy allows them to be promising candidates for photothermal therapies.

A new method for assembling citrate capped gold nanoparticles into crystallographically aligned supraparticles is reported. These are biocompatible and have a strong SERS response. Additionally, these have been shown to convert light to heat more efficiently than their nanoparticle building blocks.

Furthermore, gold nanoparticles were assembled onto a superparamagnetic iron oxide (SPION) core. These anisotropic assemblies called suprashells have a plasmon band in the near-infrared (NIR) region which makes them suitable candidates for biological applications. They also make efficient thermal transducers and promising SERS substrates due to the enhancement of signal.

Finally, self-assembled structures of monomer fluorenylmethyloxycarbonyl (Fmoc) protected amino acids are used as potential templates for gold nanoparticle assemblies. Each Fmoc-amino acid assembles into its own unique structure depending on the intrinsic property of its side chain. These soft templates are used to guide the assembly of gold nanoparticles. It has been found that there is a symbiotic relationship between the gold nanoparticle and amino acid side chain which can dictate the final degree of order.

Publications (chronological order)

1. Thompson, S. A., **Paterson, S.**, Azab, M. M. M., Wark, A. W., & de la Rica, R. (2017). Light-Triggered Inactivation of Enzymes with Photothermal Nanoheaters. *Small*, 1603195, 1603195.
2. ***Paterson, S.**, Thompson, S. A., Wark, A. W., & de la Rica, R. (2017). Gold Suprashells: Enhanced Photothermal Nanoheaters with Multiple Localized Surface Plasmon Resonances for Broadband Surface-Enhanced Raman Scattering. *The Journal of Physical Chemistry C*, 121(13), 7404–7411.
3. Rucinskaite, G., Thompson, S. A., **Paterson, S.**, & de la Rica, R. (2017). Enzyme-coated Janus nanoparticles that selectively bind cell receptors as a function of the concentration of glucose. *Nanoscale*, 9(17), 5404–5407.
4. ***Paterson, S.**, Thompson, S. A., Gracie, J., Wark, A. W., & de la Rica, R. (2016). Self-assembly of gold supraparticles with crystallographically aligned and strongly coupled nanoparticle building blocks for SERS and photothermal therapy. *Chem. Sci.*, 7(9), 6232–6237.
5. O'Connor, E. F., **Paterson, S.**, & de la Rica, R. (2016). Naked-eye detection as a universal approach to lower the limit of detection of enzyme-linked immunoassays. *Analytical and Bioanalytical Chemistry*, 408(13), 3389–3393.
6. **Paterson, S.**, & de la Rica, R. (2015). Solution-based nanosensors for in-field detection with the naked eye. *The Analyst*, 140(10), 3308–3317.

* Publications related to this thesis

Abbreviations List

0D	Zero Dimensional
1D	One-Dimensional
2D	Two Dimensional
3D	Three Dimensional
A	Alanine
AFM	Atomic Force Microscopy
AuNPs	Gold Nanoparticles
C	Cysteine
CA	Calcium Acetate
CD	Circular Dichroism
Cps	Counts per seconds
CT-PEG ₁₂	CT(PEG) ₁₂ Carboxy-PEG-Thiol
CW	Continuous Wave
D	Aspartic Acid
DFM	Dark Field Microscopy
E	Glutamic Acid
F	Phenylalanine
FBS	Fetal Bovine Serum
Fmoc	Fluorenylmethyloxycarbonyl chloride
FTIR	Fourier-Transform Infrared Spectroscopy
G	Glycine
H	Histidine
I	Isoleucine
IR	Infrared
K	Lysine
L	Leucine
Laser	Laser Amplification by Stimulated Emission of Radiation
LSPR	Localised Surface Plasmon Resonance
M	Methionine
N	Asparagine
NIR	Near Infrared
P	Proline
PC3	Prostatic Small Cell Carcinoma
PDDA	Poly(diallyl-dimethylammonium)
PEG	PEGylated
PEG12-AuNP	PEGylated Gold nanoparticles
PES	Polyethersulfone
PMMA	Poly (methyl methacrylate)
Q	Glutamine
R	Arginine
RTP	Room Temperatures
S	Serine
SEM	Scanning Electron Microscopy
SERS	Surface Enhanced Raman Scattering
SPION	Superparamagnetic Iron Oxide Nanoparticles

STEM	Scanning Transmission Electron Microscopy
SNR	Signal to Noise Ratio
T	Threonine
TEM	Transmission Electron Microscopy
UV	Ultraviolet
UV-Vis	UV-visible Spectrophotometry
V	Valine
W	Tryptophan
Y	Tyrosine

Table of Contents

Declaration	i
Acknowledgements	iii
Abstract	iv
Publications (chronological order)	v
Abbreviations List	vi
1. Introduction	1
1.1. Motivation for thesis	2
1.2. Thesis overview	2
1.3 Introduction to self-assembly	3
Non-covalent interactions driving self-assembly	5
1.3. Self-assembly incorporating nanoparticles	8
DNA self-assembly: Initial use of biomolecules for nanoparticle assembly	9
Alternative templating methods.....	13
Self-assembly using an external stimulus	16
Other chemical and biological assemblies	19
1.4. Gold nanoparticles	22
1.5. Techniques applied to the application of self-assembled AuNPs	25
Raman spectroscopy.....	25
SERS	28
Photothermal applications.....	30
2. Self-assembly of gold supraparticles with crystallographically aligned and strongly coupled nanoparticle building blocks for SERS and photothermal therapy.	33

2.1	Abstract.....	34
2.2	Introduction	35
2.3	Experimental.....	37
2.3.1	Materials.....	37
2.3.2	Synthesis of nanoparticle building blocks and assembly of gold supraparticles.....	37
2.3.3	Electron microscopy imaging.....	37
2.3.4	Dark field microscopy (DFM) and SERS experiments	37
2.3.5	Cell culture and supraparticle/nanoparticle internalization	39
2.3.6	Photothermal experiments	39
2.4	Results and Discussion	40
2.5	Conclusions and Further Work.....	58
3.	Gold suprashells: enhanced photothermal nanoheaters with multiple LSPR for broadband SERS.....	59
3.1	Abstract.....	59
3.2	Introduction	61
3.3	Experimental.....	64
3.3.1	Materials.....	64
3.3.2	Suprashell Assembly:.....	64
3.3.3	SERS.....	64
3.3.4	SERS Mapping	65
3.3.5	Scanning electron microscopy	65
3.3.6	Cell culture and Nanoparticle Internalization.....	66
3.3.7	Cell accumulation and photothermal experiments.....	66
3.4	Results and Discussion	68
3.5	Conclusion and Further Work.....	83
4	Self-assembled structures of the Fmoc protected amino acids and their potential use as templates for gold nanoparticle assembly.	84
4.1	Abstract.....	85
4.2	Introduction	86

4.3	Experimental.....	90
4.3.1	Materials.....	90
4.3.2	Fmoc amino acid assembly.....	91
4.3.3	PEGylated gold nanoparticles	91
4.3.4	PEGylated gold nanoparticles with the Fmoc-monomers	91
4.3.5	Fourier Transform Infra-red Spectroscopy (FTIR).....	92
4.3.6	Circular Dichroism (CD)	92
4.3.7	UV-vis spectroscopy	92
4.3.8	Atomic Force Microscopy (AFM)	93
4.3.9	Transmission Electron Microscopy (TEM).....	93
4.3.10	Scanning Electron Microscopy (SEM).....	94
4.3.11	Coarse-grained simulations	94
4.3.12	Raman experiments.....	94
4.4	Systematic study of Fmoc-amino acids.....	94
4.5	Aromatic Amino Acids.....	97
4.6	Hydrophobic amino acids	106
4.7	Hydrophilic amino acids	115
4.8	Charged Amino Acids.....	121
4.9	'Other' amino acid.....	131
4.10	Conclusions and Further work.....	142
5	Conclusions and Future Work.....	145
6	References	148

1. Introduction

1.1. Motivation for thesis

The motivation for this thesis was to develop self-assembled structures containing gold nanoparticles with enhanced physiochemical properties. With current economic constraints, there is a need for a cost effective and facile approach to assembling particles of higher order. Creating ordered plasmonic structures was first achieved through assisted self-assembly using an external stimulus then further structures were created through templated assembly. Moreover, templates created using the molecular self-assembly of the amino acids are also investigated as an alternative to current DNA-based methods. The applications of these particles are further explored through sensing techniques such as surface enhanced Raman scattering (SERS) and photothermal therapy with cells.

1.2. Thesis overview

This thesis is split into four individual chapters. The first chapter is a literature review of recent research in self-assembly, predominantly nanoparticle self-assembly. Initially, there is an overview of the general self-assembly and the non-covalent interactions that govern self-assembly and how these are important for structures to be realised. Then recent advances in nanoparticle assembly through surface modification and templated self-assembly are discussed with further examination into the gold nanoparticle building blocks, their synthesis and optical properties. The literature review will also include a background of Raman spectroscopy and surface enhanced Raman spectroscopy with gold nanoparticles. To conclude, the potential photothermal applications of these structures will also be explored.

The experimental chapters 2, 3 and 4 are presented separately with their own abstract, introduction, material and methods, results and discussion and conclusions. This layout allows the reader to consult each chapter individually.

Chapter 2 describes the formation of gold supraparticles from individual nanoparticle building blocks. Inspired by mesocrystals observed in nature, the

building blocks are crystallographically aligned and biocompatible. Their sensing capabilities were further examined with SERS and their potential bioapplications for photothermal therapy was also carried out *in vitro*.

Chapter 3 reports a new type of self-assembled nanostructure called suprashells which consists of anisotropic collections of nanoparticles assembled onto a superparamagnetic core. These nanoparticles assembled onto a magnetic core have coupled plasmon resonances which are similar to individual anisotropic nanoparticles such as nanorods. They also have an extinction within the near-infrared region (NIR) which can be advantageous in biological tissues due to deeper light penetration, reduced absorbance and scattering of NIR light. Heating properties of the suprashells were carried out as well as a proof of concept experiment demonstrating the photothermal application to kill prostate cancer cells.

Chapter 4 is the final experimental chapter which explores the concept of both molecular self-assembly and nanoparticle self-assembly. First, there is a systematic study of the molecular self-assembly of Fmoc amino acids. These self-assembled structures are further used as potential templates for nanoparticle assembly. It is proposed that each amino acid will assemble into a unique structure due to the intrinsic properties of their side chain thus will create nanoparticle assemblies with varying degrees of order.

1.3 Introduction to self-assembly

Self-assembly is the autonomous process by which simple molecules spontaneously organise into highly ordered systems.¹⁻³ These ordered systems are an integral part of many scientific disciplines such as chemistry, biology and materials science which has allowed it to evolve into a dynamic field of research. The vast complexity and diversity of self-assembled processes make them an appealing area to study therefore, it comes as no surprise that the number of publications for 'self-assembly' has grown exponentially over the past twenty years.⁴ Self-assembly can be classed as dynamic or static. Dynamic self-assembly is a process of self-assembly in which

the formation of molecules requires the dissipation of energy into its surroundings, this is still a relatively new area of research that is still in its infancy. Static self-assembly is the most common form of assembly that is studied, structures that form from static self-assembly reach an equilibrium that is at the local/global minimum. Some common examples of static self-assembly are ribosome crystal structures or the self-assembly of peptide amphiphiles into fibres (Figure 1.1).⁵ At the centre of these ordered structures are functional building blocks which dictate the overlying characteristics of the structure therefore it is imperative that we are able to tune their arrangement with fine control. For self-assembly to be realised the molecules must overcome the entropic constraints of the system. One commonality of all spontaneous self-assembly is that it is a thermodynamically driven process which is governed by non-covalent interactions. These include; hydrogen bonding; electrostatic interactions; van der Waals; and π - π stacking.⁶

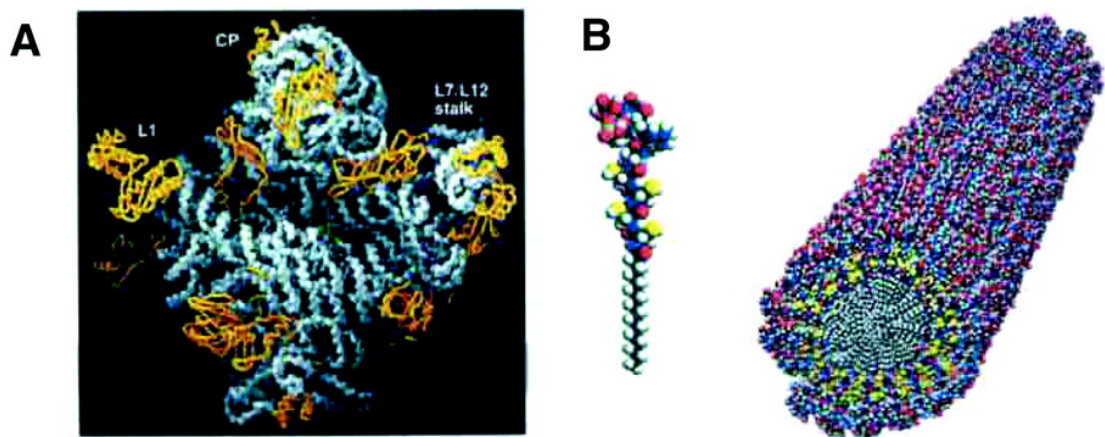


Figure 1.1 Examples of static self-assembly. (A) crystal structure of a ribosome. (B) Self-assembled peptide amphiphile. Figure taken from Ref. 5

Non-covalent interactions driving self-assembly

Spontaneous self-assembly is a thermodynamically governed process in which the system is driven to a state of equilibrium. This results in a decrease in Gibbs' free energy (ΔG). A simple Gibbs' free energy equation can be used to represent the thermodynamics of the system:

$$\Delta G = \Delta H - T\Delta S$$

Eq. 1.1 Gibbs Free Energy

For the reaction to move forward the Gibbs' free energy must be negative ($\Delta G < 0$) and for it to be spontaneous the change in enthalpy must also be negative ($\Delta H < 0$).⁷ The intermolecular forces between the assembling moieties determine the change in enthalpy; The change of entropy (ΔS) is associated with the organization of molecules; the molecules go from a disordered state to an ordered state ($\Delta S_{\text{system}} < 0$). When considering the system as a whole, there is an entropic gain ($\Delta S_{\text{surrounding}} > 0$) from the surrounding water molecules, a phenomenon termed the *hydrophobic effect*. Self-assembly is driven by contributions from both entropy and enthalpy, however, the synergistic effects of the interactions between the molecules usually dominates over the entropic effects of the solvent.

Electrostatic interactions are based on the Coulombic interactions between two charged groups. They can be of opposing charges, which results in attraction, or of the same charge, which causes repulsion. The magnitude of force (F) between the atoms can be calculated using a variation of Coulomb's law which accounts for solvent effects:

$$F = \frac{q_i q_j}{4\pi\epsilon r_{ij}^2}$$

Eq. 1.2 Coulombs Law

where q_i and q_j are the charges on the atoms, ϵ is the permittivity of a vacuum ($8.854188 \times 10^{-12} \text{ J}^{-1} \text{ C}^2\text{m}^{-1}$) multiplied by the dielectric constant of the solvent, r_{ij} is the distance between the atoms. As the distance between the atoms decreases, the magnitude of force will increase. There are three types of electrostatic interactions; ion-ion, ion-dipole, and dipole-dipole. Of these three interactions, ion-ion interactions are the strongest (*ca.* 100 - 350 kJ mol^{-1}), they are non-directional, highly dependent on the surrounding medium and have the longest interaction range. Ion-dipole interactions are also non-directional but are weaker than ion-ion interactions (*ca.* 50 - 200 kJ mol^{-1}) and have medium range interactions. The weakest and shortest-range interaction is dipole-dipole (*ca.* 5 - 50 kJ mol^{-1}), which is somewhat directional and occurs between molecules that have permanent dipoles.⁸

van der Waals forces are the weakest of all the noncovalent electrostatic interaction, ($< 5 \text{ kJ mol}^{-1}$) and arise from transient induced dipoles originating from the electron cloud which surrounds the atom. Van der Waals can be split into the attraction term known as the London dispersion force and the exchange-repulsive term. Initially, the attractive forces increase at short distances, however when the atoms get too close, the strong repulsive forces become dominant due to the overlap of the outer electron clouds.⁹

Hydrogen bonding arises from electrostatic interactions that can occur between a hydrogen that is covalently attached to a highly electronegative atom (such as N, O or F) and another electronegative atom. This is due to the covalently bound electronegative atom pulling electron density away from the hydrogen thus causing the hydrogen to bear a partially positive charge. Moreover, hydrogen bonds are somewhat directional with the strong bonds occurring when a hydrogen bond acceptor (e.g. N-H) is 180° to the hydrogen bond donor (e.g. C=O). The strength of hydrogen bonds can vary from 8 kJ/mol up to 169 kJ/mol in $\text{FH}\cdots\text{F}$.¹⁰

π - π stacking is the bonding attraction between the π orbitals on aromatic rings. The simplest of aromatic groups is benzene. Due to the pi electron density on the ring, this creates a quadrupole moment which causes the periphery of the ring to be

partially positive and the faces of the aromatic ring to be negative. Therefore, π stacking is usually preferred as off centred face-edge, or edge-face perpendicular rather than face centred stacking. π stacking is commonly seen in biological self-assembly such as peptides which contain aromatic moieties or between DNA nucleobases.

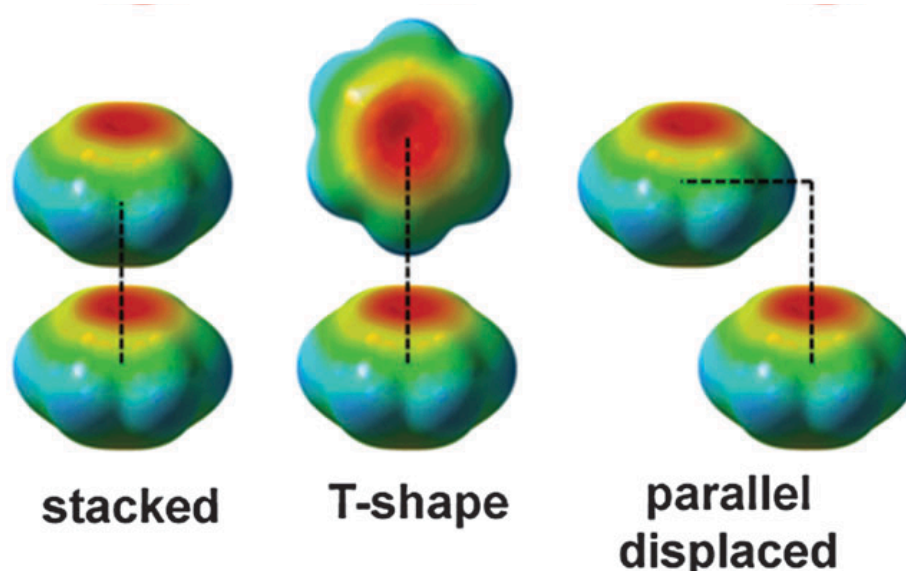


Figure 1.2 Different orientations of aromatic interactions. Figure adapted from Ref. 11

Hydrophobic effect is an occurrence that is observed when nonpolar molecules are added to a polar solvent such as water. Most biomolecule reactions take place in aqueous solutions. Water is good at creating hydrogen bonds with itself therefore when a nonpolar molecule is added to the mixture, it is not capable of forming hydrogen bonds with the water thus disrupts the H-bond network and the water molecules have to rearrange around the nonpolar molecule to accommodate it. When two or more nonpolar molecules are added to a solution, they will self-associate, thus minimising the overall contact of water with the molecule, this is deemed the hydrophobic effect.¹¹ Initially the water forms an ordered cage around the nonpolar molecule which is locally energetically unfavourable as the molecules come closer together. However, as the water is released into the bulk solution and the overall entropy of the solution will increase. The hydrophobic effect is thought to be a major effect in driving the self- assembly of micelles and fibres.

1.3. Self-assembly incorporating nanoparticles

In recent times metallic nanoparticles have been utilised as nanoscale building blocks due to their exceptional physicochemical properties. However, nanoparticles alone cannot create structures of order. More so it is the surface modifications and surrounding media that control the final morphology. For stabilisation and functionality, nanoparticles are usually covered by ligands whose chemical group and/or charge may dictate the final outcome of the arrangement. Siegal also broadly classified nanostructures into four different dimensionalities¹²

- Zero dimensional structures (0D), have all dimensions in the nanoscale level (<100nm), typically atom clusters such as nanoparticles.
- One-dimensional structures (1D) have two dimensions on the nanoscale level, and one into the macroscale level, nanowires and nanotubes are typically observed as 1D structures
- Two-dimensional structures (2D) have one dimension in the nanoscale level and two in the macroscale level, these exhibit flat plate-like structures such as nanodisks or heterostructures
- Three dimensional structures (3D) have all three dimensions out with the nanoscale level, such as nanoparticle crystals or nanofiber bundles.

There are a multitude of ways that nanoparticle structures can be assembled these include, templates, the use of a directing field, and direct intermolecular interactions of the capping agents.¹³ Templated strategies use a scaffold to guide the self-assembly. Nanoparticles can be arranged around a template that forms the basis for the final structure. For example, helical nanoparticle superstructures can be obtained using self-assembled peptide amphiphiles as templates.¹⁴ The use of an external stimuli such as light, magnetic or physical force can also be used to facilitate nanoparticle arrangements.^{15,16} A good example of this type of self-assembly is the formation of 1D nanoparticles chains after the application of an electric field.¹⁶ Lastly, direct assembly can be achieved through surface modification of the nanoparticles whereby assembly is mediated through straight forward

intermolecular interactions of the capping ligand, for example, through complementary DNA-DNA interactions. Nanoparticle assemblies are promising candidates for a range of applications these include but are not limited to: biosensors,¹⁷⁻¹⁹ drug delivery systems,^{20,21} catalysis¹⁶ and electronic devices.²²

DNA self-assembly: Initial use of biomolecules for nanoparticle assembly

DNA was the first biomolecule employed to create nanoparticle structures of defined geometries. Two methods derived employing DNA functionalisation include direct assembly and templated assembly. Chad Mirkin was one of the first pioneers in this field by creating a method for obtaining reversible 3D aggregates of gold nanoparticles modified with DNA.²³ The oligonucleotides were grafted onto the nanoparticles by thiol groups which were designed to have “sticky” complementary ends that triggered the aggregation of the nanoparticles. This caused the solution to change from dark red to purple due to the coupling of the nanoparticles localised plasmon resonance (LSPR). By heating up the solution the DNA strands would dehybridise and the solution would return back to red. Mirkin further developed this method to create 3D superlattices using DNA modified nanoparticles.²⁴ The DNA sequences were carefully constructed so their pairing would cause the nanoparticles to assemble into either of face-cubic centred or body centred cubic crystal structures (Figure 1.3).

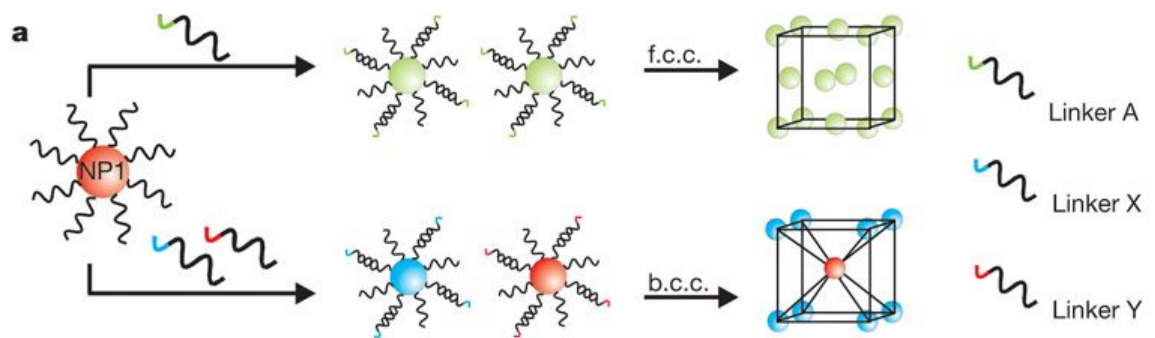


Figure 1.3 Gold nanoparticle superlattices which can be programmed into different crystal lattice arrangements by changing the DNA linker. Figure adapted from ref 23.

Around the same time, Oleg Gang also developed a method for assembling thermally responsive 3D nanoparticle crystalline structures using complementary sets of DNA functionalised onto nanoparticles.²⁵ Moreover, Gang *et al* also engineered DNA origami frameworks which have ‘sticky ends’ complementary to strands functionalised onto nanoparticles.²⁶ DNA origami is a method of folding a single strand of DNA into any target structure. By using sticky ends complementary to the DNA functionalised onto the nanoparticles, the nanoparticles can be arranged into exquisite lattice arrangements whose final structure is dictated by the DNA framework (Figure 1.4).

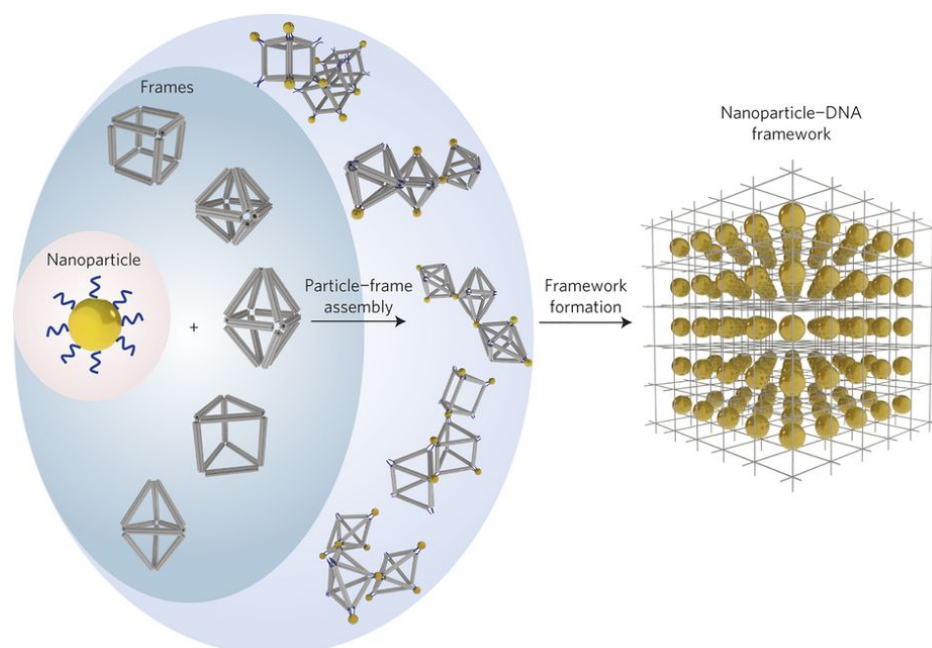


Figure 1.4 DNA origami frames designed with complementary DNA strands at the vertices that will bind with the nanoparticles. The final shape of the nanoparticles assembly is dictated by the framework produced by DNA. ²⁶

Other approaches have also utilised DNA as frameworks for templates or modified directly onto the nanoparticles. Nanoparticles bound onto the surface of DNA bundles were chirally active. They found by toggling the direction of the nanoparticle-DNA bundles, the chirality would switch from right handedness to left handedness.²⁷ Nanoparticles have also been hybridised onto DNA nanotubes to create a high yield of 1D arrays is a promising route for nanodevices which incorporate DNA-based arrays as one of the limitations of DNA based nanoparticle assemblies have typically low yield.²⁸ Another approach has been to modify nanoparticles directly with DNA. DNA molecules are functionalised and are arranged into ‘petals’ onto gold nanoparticles so the DNA/nanoparticle structure appears as nanoflowers. There are linker DNA molecules that extend out from the petals which direct the lattice structure shape. The gold nanoparticles can therefore be arranged as chains, square lattice and hexagonal lattices.²⁹

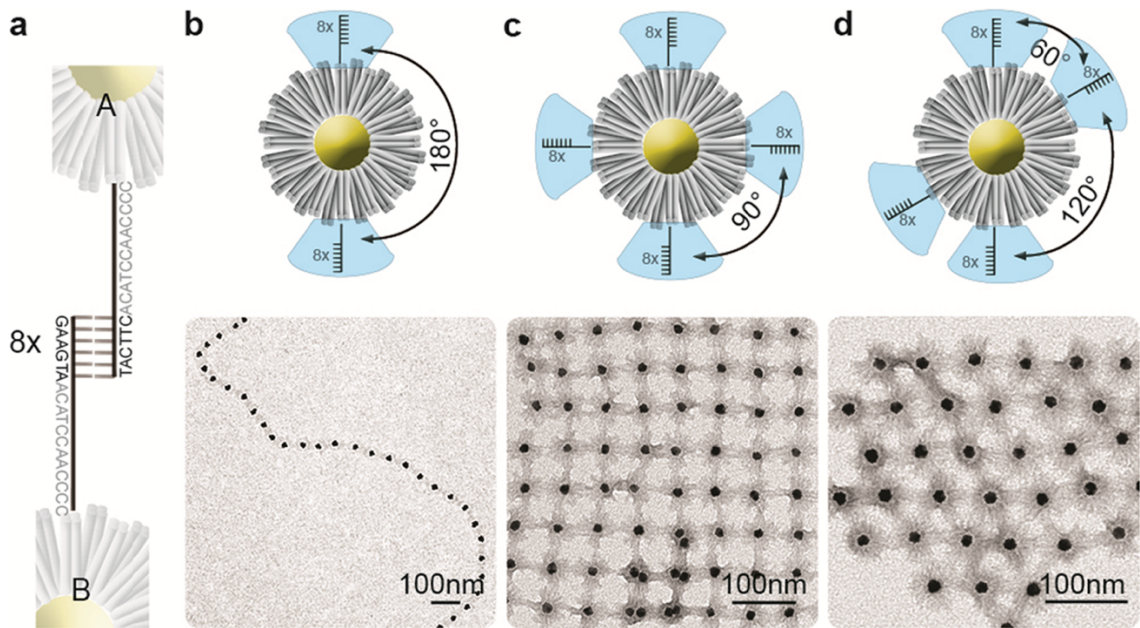


Figure 1.5 DNA origami flowers with a) extended linker DNA molecules that can be arranged in b) chain c) square lattice d) hexagonal lattices.²⁹

Although DNA is a useful tool for assembling nanostructures, it is not without its limitations as the structure is confined by the length of the scaffold and there is typically a low yield.^{30,31}

Alternative templating methods

Templating methods that do not use DNA interactions have also been reported.³²⁻³⁵ These include co-templating techniques which allow the nanoparticles to arrange onto a prefabricated surface or soft templates which have an affinity for reactive sites on the nanoparticle thus creating structures of higher order. Materials for the frameworks include other metallic surfaces such as titanium dioxide³⁶ or carbon which has been arranged into tubules.³³ A poly(methyl methacrylate) (PMMA) substrate has also been used to facilitate assembly of 1D chains of polyethylene glycol (PEG) covered gold nanoparticles with tailorable plasmon resonances in the near-infrared region (Figure 1.6).³⁷ In this approach, negatively charged PEG-gold nanoparticles are added to a PMMA mask with positively charged trenches. The nanoparticles assemble within these trenches that determine the final size of the 1D arrays.

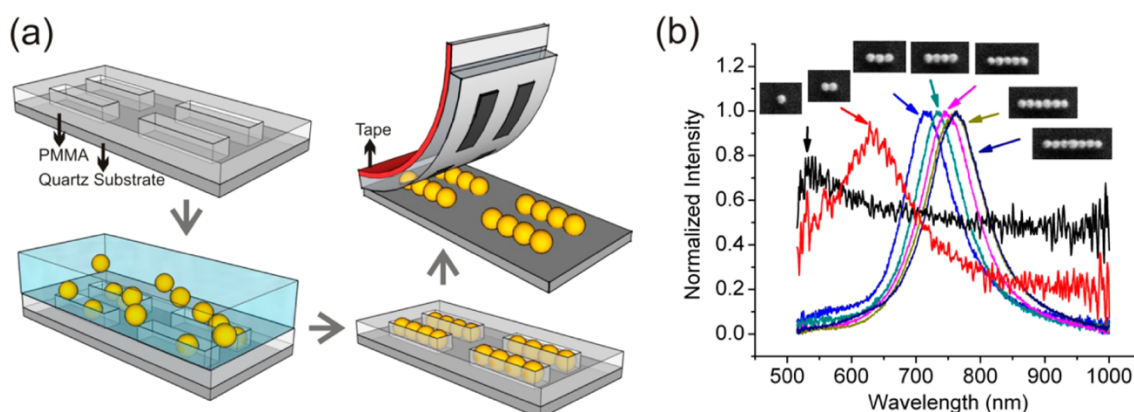


Figure 1.6 a) Schematic flowchart of the PMMA substrate templates which are used to facilitate 1D chains of nanoparticles and b) UV-vis spectra with corresponding SEM images of the 1D chains.³⁷

Gold ions have even been reduced onto hydrophilic and hydrophobic surfaces such as PDMS, glass and 96 well plates to create a gold nanoparticle film which can be used as a colorimetric sensing platform for the flu virus.³⁸ The gold nanoparticle film was used as an anchor for a capture antibody specific to the target virus. A secondary antibody conjugated with HRP is functionalised onto another nanoparticle and this is used as the detection molecule. 3,3',5,5'-Tetramethylbenzidine (TMB) is used as the substrate which converts HRP from colourless to blue which produces a colorimetric signal (Figure 1.7). Other gold nanoparticle films have also been utilised as SERS substrates.³²

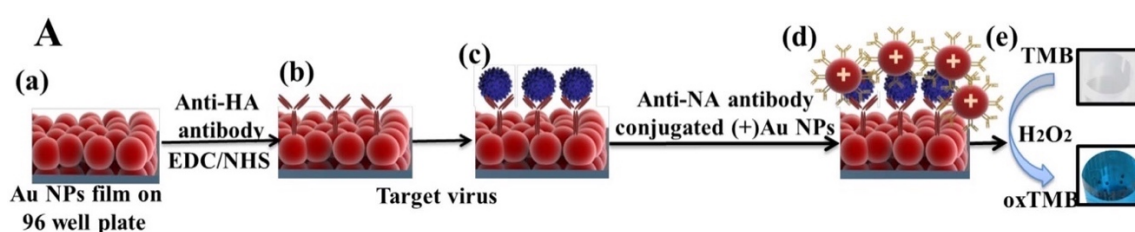


Figure 1.7 Schematic representation of the immunoassay from the gold nanoparticle film. Figure adapted from Ref. 36

Nanoparticles can also be elegantly arranged via a pseudorotaxane host-guest binding motif.³⁹ A pseudorotaxane is a group of compounds which are interlaced through a macrocyclic compound. Nanoparticles were functionalised with the guest unit (tetrathiafulvalene) and the symmetry of the host unit (tetracationic cyclophane) could be varied which dictated the final configuration of the nanoparticles into dimers, trimers and tetramers (Figure 1.8). Other templated crosslinkers have included pyridine-based structures, likewise the shape of and size of the pyridine compound dictates the final degree of assembly of the nanoparticles and the plasmon resonance.⁴⁰

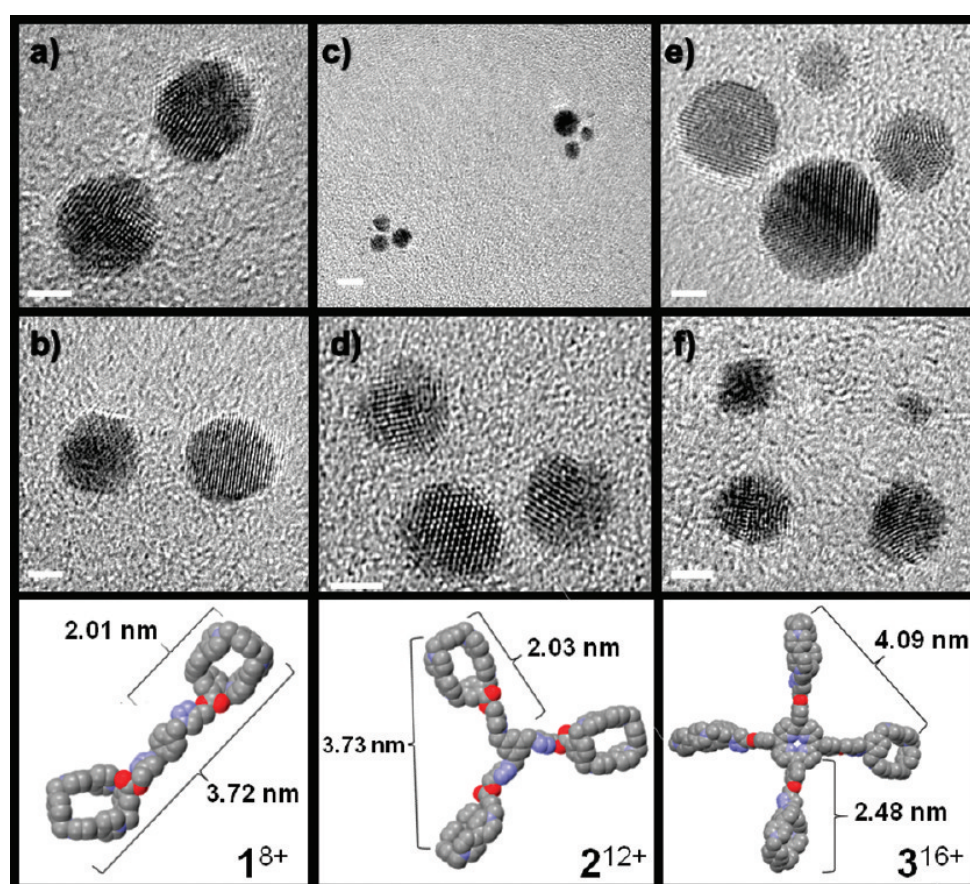


Figure 1.8 TEM images of the assembled nanoparticles from the pseudorotaxane compounds into (a, b) dimers, (c, d) trimers and (e, f) tetramers. Scale bar = 2 nm (a, b, d, and f). Scale bar = 5 nm (c). Bottom row is the geometries.³⁹

Self-assembly using an external stimulus

The use of an external force can often aid the assembly of nanoparticles, these include UV irradiation, magnetic fields and fluid interfaces. UV light can be used as an assembling aid through photoresponsive ligands which are capped on the surface of the nanoparticle. One assembling mechanism includes conjugating the nanoparticles with an azobenzene derivative. When irradiated with UV light the isomerisation of the azobenzene changes from trans to cis, thus controlling the interparticle distance of the nanoparticles and they come in close contact which also causes a red-shift in the UV-vis spectrum (Figure 1.9).⁴¹ Interestingly, UV-light can also aid intermolecular interactions where non polar molecules become polar when irradiated with UV light, i.e. sipropyran. This causes dipole interactions to occur between the molecules functionalised onto the nanoparticle, aiding assembly.⁴²

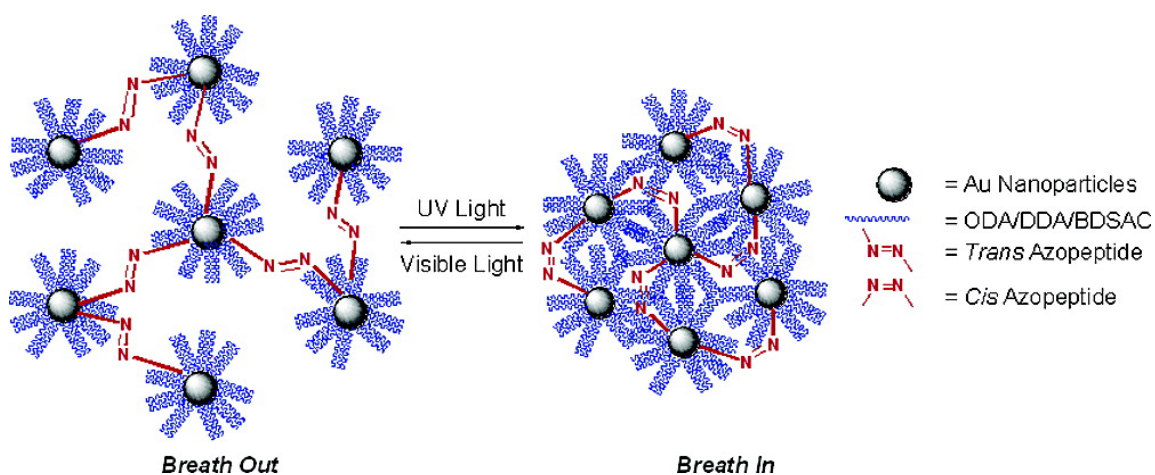


Figure 1.9 Assembly of gold nanoparticles with a UV-responsive ligand. Adapted from ref 41

Magnetic materials have also been utilised to assist nanoparticle assembly. Core-shell gold-cobalt nanoparticles are assembled onto a substrate into long chains or rings, then the cobalt shell is dissolved using hydrochloric acids which leaves the gold assemblies.⁴³ Other magnetic approaches use a magnetic core and a gold nanoparticle shell.⁴⁴ One example of the production of an iron oxide-gold core-shell assembly is the use of an oil-in-water microemulsion techniques which produces dense nanoclusters. This method produces particles with strong plasmon resonances in the NIR region and with an outer gold nanoparticle shell the surface is easily modified with biomarkers (Figure 1.10).

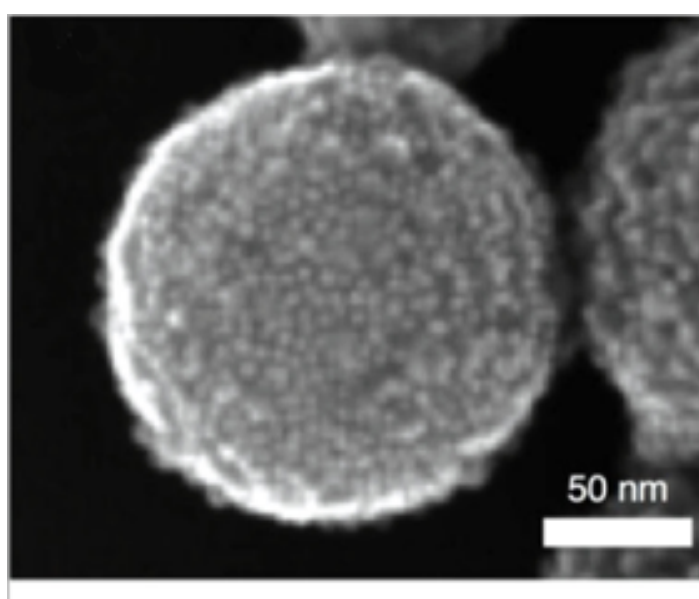


Figure 1.10 TEM image of the magneto-plasmonic nanoclusters Adapted from ref 43.

Self-assembly can also occur at liquid interfaces where nanoparticles can be trapped, this tool is known as the Pickering-Ramsden emulsions.⁴⁵ There are number of methods that have utilised this.⁴⁶⁻⁴⁸ However, one method combines the use of light and force, a solution of chloroform with triarylamine is irradiated with a halogen lamp, this creates helical fibres. This solution is further mixed with a solution of gold nanoparticle in water, at the interface where water and chloroform meet the nanoparticles diffuse onto the fibres. Further centrifugation causes the nanoparticles to align along the fibres in an orderly manner (Figure 1.11).⁴⁹

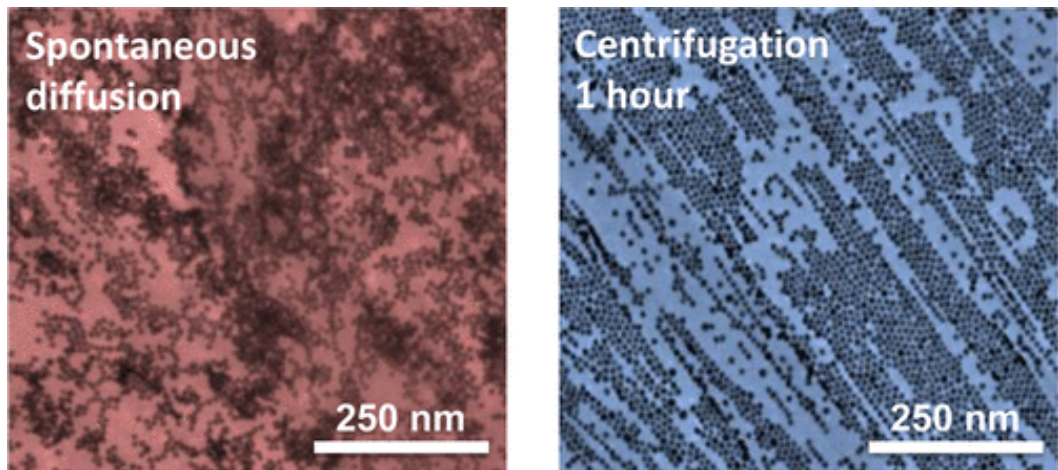


Figure 1.11 Ordering of nanoparticles before and after centrifugation on the polymer film. ⁴⁹

Another example using an interface to encourage assembly is the production of colloidosomes. These are hollow gold nanoparticle assemblies made from spherical nanoparticles closely packed at the water/oil interface. Water droplets containing the gold nanoparticles are suspended in 1-butanol, this causes the nanoparticles to be adsorbed at the liquid-interface driven by the minimisation of the free energy. With time, water is slowly diffused into the 1-butanol which compacts the nanoparticle layer which produces a closely packed shell of nanoparticles (Figure 1.12).^{35,50}

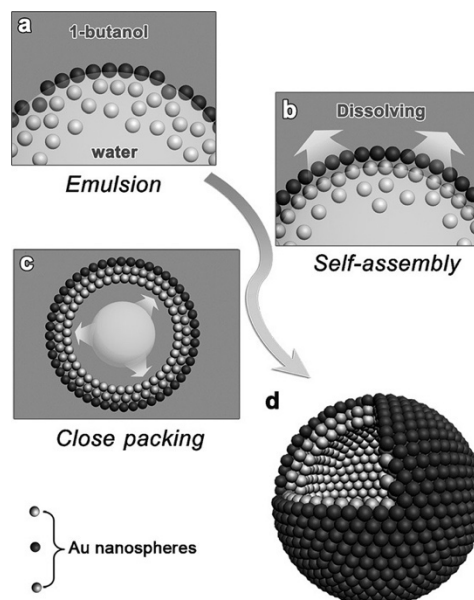


Figure 1.12 Mechanism of the production of colloidosomes. ³⁵

Other chemical and biological assemblies

As previously observed the capping ligand used to modify the surface of nanoparticles is perhaps the most important factor for self-assembly to be realised. Although self-assembly can be aided with the use of a template or stimulus, there are some methods which are more straight forward and exploit the intermolecular forces between molecules.

Nanoparticle amphiphiles have been used to assemble dimers, chains and extended clusters.⁵¹ 11-mercaptoundecanoic acid (MUA) and 1-dodecanethiol (DDT) were functionalised onto the nanoparticle. By controlling the ratio of the mixed monolayer of hydrophobic and hydrophilic, the desired length of nanoparticle assembly could be achieved.

Biological capping agents such as protein and amino acids are excellent tools for use in applications where the assembled structure must be biocompatible. Citrate capped nanoparticle formed anisotropic assemblies in the presence of cysteine, these assemblies caused a bathochromic shift of the absorption band towards the NIR region.⁵² Other amino acid based triggers include the use of cysteine and glutathione to facilitate assembly of nanorods, sphere and bipyramids into nanonecklaces (Figure 1.13).⁵³ Equal concentrations of nanorod and nanospheres were added to a mixture of glutathione and end-end alternating assembly was found between the nanorod and nanoparticles. The same method was used for the bipyramids and spheres with cysteine. Since the nanorods and bipyramids are encapsulated in a layer of CTAB, the glutathione and cysteine bind preferentially to the ends where the CTAB is less ordered and curved. However, it should be noted that CTAB is toxic to cells therefore this type of assembly is not compatible in biological conditions.⁵⁴

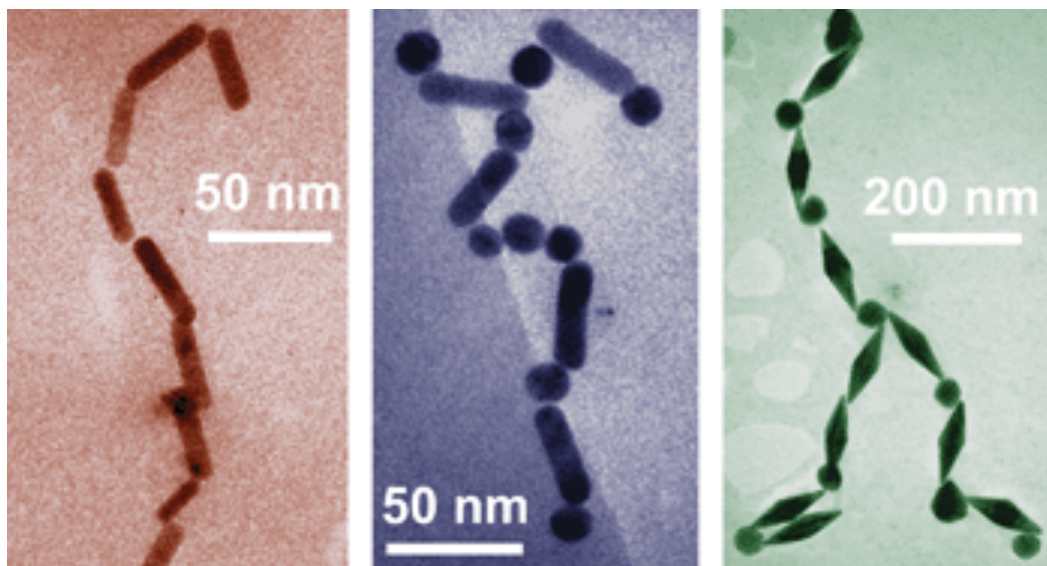


Figure 1.13 Nanonecklaces produced from a mixture of nanorods, spheres and bipyramids with either glutathione or cysteine.⁵³

Another amino acid which has been used as crosslinker for nanoparticle aggregation is lysine.⁵⁵ Lysine binds to gold nanoparticles in solution. Under acidic conditions, lysine binds preferentially via the α -amino group, however under basic conditions this is suppressed due to the ionisation of the α -carboxylic acid group which induces repulsion against the negatively charged gold nanoparticles. Assembly is therefore mediated through zwitterions. Nanoparticle films have also been produced using protein pairing of artificially designed complementary amino acid sequence.⁵⁶ The peptides functionalised onto the gold nanoparticles are rigid but also have 3D architecture. This process was also found to be reversible by adding an excess of one free protein.

Another one-step fabrication approach with proteins includes functionalising citrate capped nanoparticles with varying concentrations biotin-binding proteins, avidin, neutravidin and streptavidin in acidic conditions.⁵⁷ These assemblies retain their biotin-binding capabilities and are LSPR tuneable (Figure 1.14). The biotin-streptavidin interaction is a commonly used biological interaction as the interactions are rapid, highly specific and strong. Further gold nanoparticle assemblies have also made use of these interactions to create nanowires, 3D cubes and clusters.⁵⁸⁻⁶¹

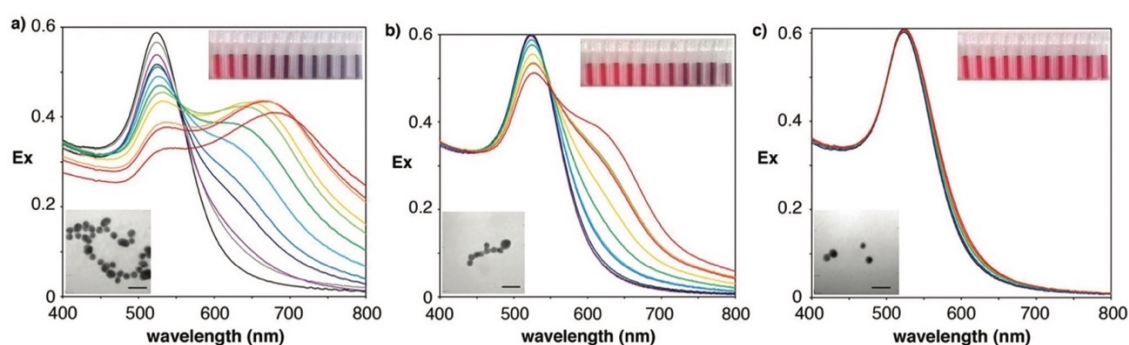


Figure 1.14 Extinction spectra of the gold nanoparticle suspensions with varying concentrations of avidin in a) 2.5 mM citrate buffer at pH 6 b) in 2.5 mM bicarbonate buffer at pH 9 and c) in 2.5 mM bicarbonate buffer at pH 11. Right corner inset is a photograph of resulting gold nanoparticle solutions with increasing avidin concentrations from left to right and left corner inset is TEM images of nanoparticles upon addition of 0.22 nM avidin.⁵⁷

1.4. Gold nanoparticles

As discussed previously nanoparticles play an important role as building blocks in self-assembly. Much of the work carried out by other research groups has centred on the use of gold nanoparticles, and the work exhibited in this thesis also uses the same coinage metal particles. Therefore, it is important to discuss them in more detail. Gold nanoparticles have exceptional optical properties that makes them useful building blocks for self-assembly. These properties are due to the oscillation of valence electrons delocalised around the metal conduction band known as the LSPR (Figure 1.15).^{62,63}

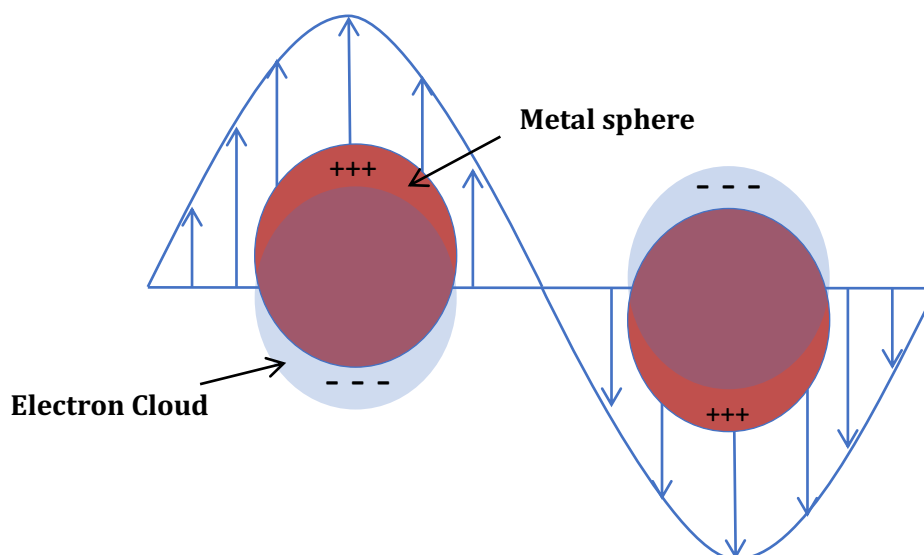


Figure 1.15 Oscillation of the electron cloud surrounding the metal sphere.⁶⁴

Spherical gold nanoparticles show a strong LSPR band in the visible region. Nanoparticle LSPR is affected by their size, composition and aggregation state, as well as the dielectric constant of the surrounding medium.^{65,66} Gustav Mie described the scattering of light using the dielectric constants of spherical nanoparticles in 1908.⁶⁷ This has since become known as Mie's theory, a derivative of Maxwell's equation.

$$C_{ext} = \frac{24\pi^2 r^3 \epsilon_m^{\frac{3}{2}}}{\lambda} \frac{\epsilon''}{(\epsilon' + 2\epsilon_m)^2 + \epsilon''^2}$$

Eq. 1.3 Mie's Theory

Mie's theory is based on the radius of the particle (r), the wavelength of light, ϵ_m is the dielectric constants from the surroundings and ϵ is the dielectric constant from the particle. There are two parts of ϵ - the real, ϵ' , and the imaginary part ϵ'' . The position of the LSPR peak depends on the real part of the dielectric constant ϵ' and the imaginary part, ϵ'' determines the width of the band. This plasmon peak is affected by the size, distribution and shape of the nanoparticle.⁶⁵ Both scattering and absorbance contribute to the overall extinction of the particle seen in a UV-Vis-NIR spectrum.⁶⁸ For smaller particles total extinction is mostly due to absorption and as the nanoparticle size increases, the contribution from scattering will become more evident. The larger the diameter of particle, less energy is needed to oscillate the valence electrons hence scattering becomes a significant factor thus a red-shift of the LSPR is observed (Figure 1.16).⁶⁹

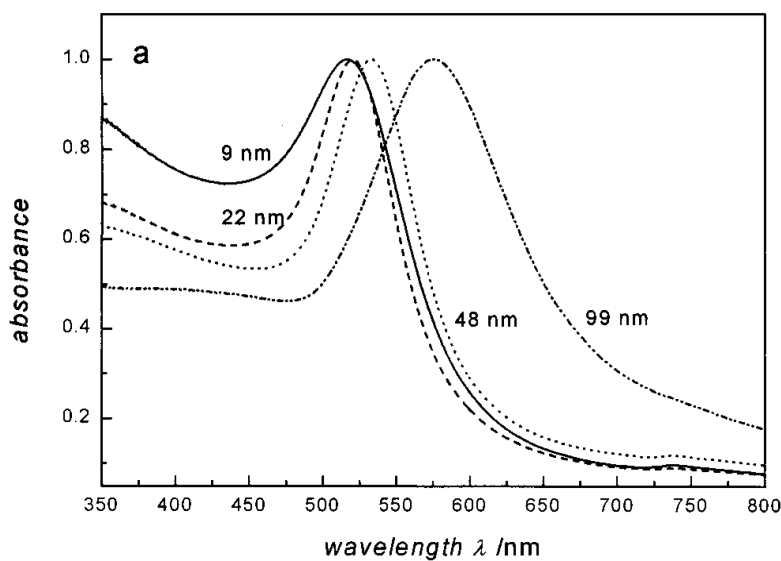


Figure 1.16 Normalised extinction spectra of gold nanoparticles of different sizes. Adapted from ref. 68

Gold nanoparticles are commonly synthesised using the Turkevich method,⁷⁰ which consists in the addition of citrate to a boiling solution of sodium tetrachloroaurate. The size of gold nanoparticles is controlled by carefully altering the ratio of the citrate to gold salt.⁷¹ When citrate is added to the gold solution, gold atoms are formed and their concentration rises until this exceeds the critical supersaturation level, the gold atoms then begin to coalesce and a nucleation period occurs (Figure 1.17). When the concentration of gold atoms drops below the supersaturation level,

nucleation of the gold atoms will stop, and number of particles will no longer increase and the concentration of gold ions will continue to grow onto the particles until all the gold in the solution has been depleted.⁶⁵ The metal sphere is then capped by the citrate producing a negatively charged surface.

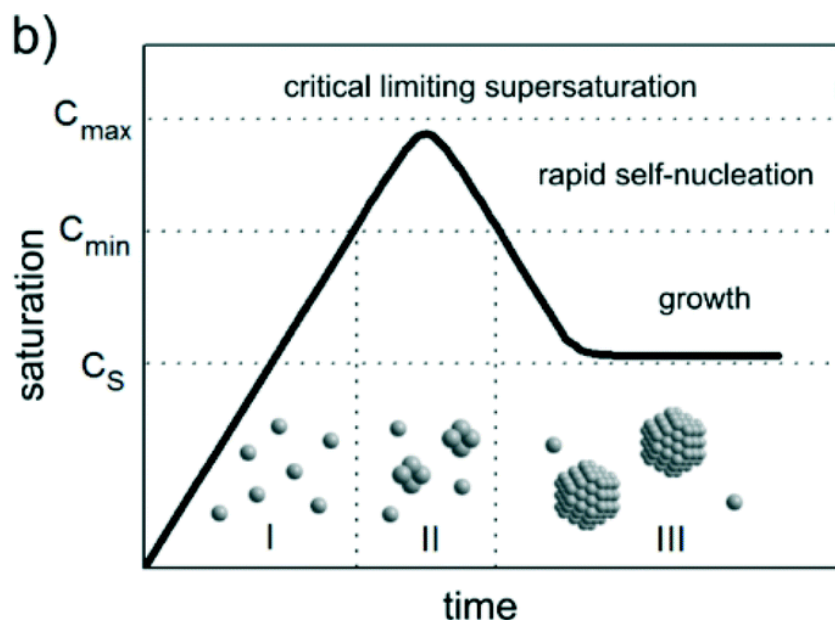


Figure 1.17 Schematic diagram of the synthesis and mechanism of gold nanoparticles⁶⁵

When nanoparticles assemble, their plasmons couple, this coupling causes an enhancement of their electromagnetic fields as well as a red-shift of LSPR which can be advantageous for further biomedical applications such as sensors which utilise surface enhanced Raman spectroscopy (SERS) and photothermal applications.⁷²

In order to appreciate the applications of gold nanoparticles it is necessary to give an overview of techniques such as Raman spectroscopy, SERS and light-to-heat (photothermal) conversion.

1.5. Techniques applied to the application of self-assembled AuNPs

Raman spectroscopy

In 1928 C.V. Raman was the first person to experimentally observe the inelastic scattering of light from molecules. This phenomenon gives information about the vibrational modes of a molecule and is now fittingly termed Raman scattering.⁷³

Quantized photons used to irradiate a sample are either scattered or absorbed. Raman spectroscopy focusses on the analysis of scattered light carrying unique molecular information. Scattering can be separated into two different categories, elastic (Rayleigh) and inelastic (Raman). Elastic scattering occurs when there is no exchange in energy between the photon and the molecule, whilst inelastic involves either a net loss or gain of energy from the photon to the molecule or vice-versa. Raman scattering can be further subdivided into two more categories; Stokes and anti-Stokes. The two types of Raman scattering are shown in Figure 1.18. Stokes scattering occurs when a molecule starting at the ground state absorbs energy from the incident photon and is promoted to a higher energy vibrational state. Anti-Stokes scattering occurs when the molecule is already in the excited state i.e. due to thermal energy, after scattering the molecule returns to the ground state due to a transfer of energy to the scattered photon.⁷⁴

For Raman scattering to occur there must be, a distortion of the electron cloud causing it to become polarised. This causes the electron cloud to be raised to an 'virtual' energy state (shown in Figure 1.18), this is an unstable and short-lived state which causes the photon to be quickly re-radiated. Raman scattering is a weak process in which only 1 in every 10^6 - 10^8 photons are scattered inelastically which makes Rayleigh scattering the dominant process.⁷⁵

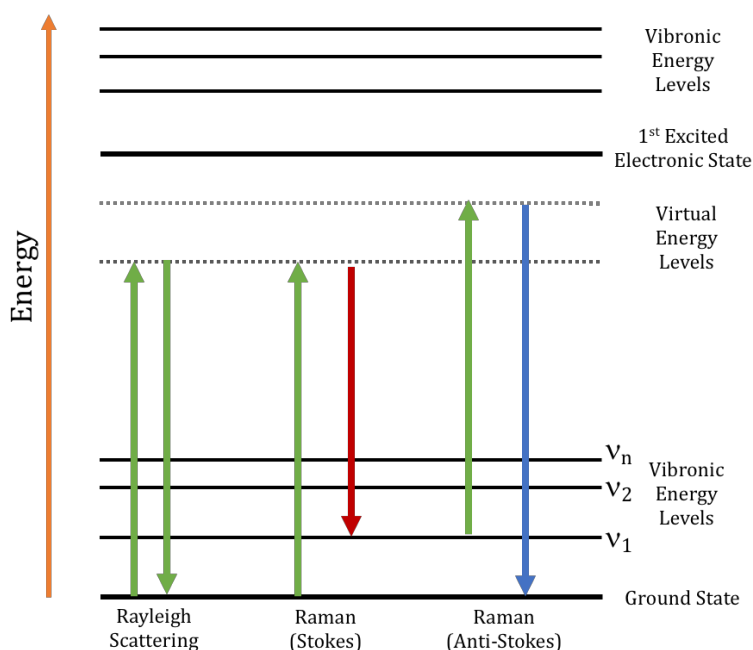


Figure 1.18 Diagram illustrating the Rayleigh and Raman scattering processes.

At ambient temperatures, most molecules will be at ground state, therefore the majority of Raman scattering will be due to Stokes scattering. The ratio of the intensities between the Stokes and anti-Stokes scattering can be calculated from the Boltzmann equation.⁷⁵ The intensities are dependent on the number of molecules at the ground and excited vibrational levels.

$$\frac{N_n}{N_m} = \frac{g_n}{g_m} \exp \left[\frac{-(E_n - E_m)}{kT} \right]$$

Eq. 1.4 Boltzmann equation

N_n = number of molecules in the excited vibrational energy level

N_m = number of molecules in the ground vibrational state

g = degeneracy of the energy levels

$E_n - E_m$ = the difference in the energy between the vibrational energy levels

k = the Boltzmann's constant ($1.3807 \times 10^{-23} \text{ JK}^{-1}$)

T = temperature (K)

However, not all molecules and vibrations are Raman active. For Raman scattering to occur there must be a change in polarizability. Equation 1.5 shows that the dipole

moment (P) is induced by an external electric field (E) and the polarizability of the molecule (α).

$$P = \alpha E$$

Eq. 1. 5 Induced Dipole

The strongest Raman scatterers are therefore symmetric molecules that have an evenly distributed electron cloud which can easily be distorted with an external electric field. Raman is therefore thought to be a complementary technique to infrared spectroscopy (IR) where vibrations with the existing dipoles give the strongest absorption signals i.e. asymmetric vibrations. The intensity of the Raman signal can be given by the following equation⁷⁴:

$$I_R \propto \nu^4 I_0 N \left(\frac{\partial \alpha}{\partial Q} \right)^2$$

Eq.1.6 Intensity of Raman signal I_R

I_0 = incident laser intensity

N = number of scattering molecules in a given state

ν = frequency of the exciting laser

α = polarizability of the molecule

Q = vibrational amplitude

Raman is a very weak phenomenon which can lead to low sensitivity and makes it difficult to measure samples of low concentration especially for samples in solution. However, over the past 30 years or so surface enhanced Raman scattering (SERS) has emerged as a technique which offers major improvements in Raman sensitivity.

SERS

Raman enhancement (SERS) can occur when a molecule of interest is adsorbed or in close proximity to the surface of a metal, particularly noble metals such as gold and silver which have nanoscale features. There are currently two widely accepted theories about how SERS is realised. One theory is termed electromagnetic (EM) enhancement, whilst the other is termed chemical enhancement (CM). The latter occurs when a bond forms between a molecule and the surface of the metal, this allows the conduction of electrons between the metal surface and the molecule. The formation of this metal-electron adsorbate complex increases the polarizability of the molecule thus the enhancement is thought to proceed via a new electronic state.⁷⁶

The EM enhancement is due to an interaction between the analyte and the electrons which oscillate across the particles dielectric surface (plasmons). When the particle is excited with a laser close to its plasmon resonance, the excitation of the surface plasmon greatly increases the local field. Any molecule that is adsorbed onto the surface of the metal or is confined to the oscillating electric field will benefit from the enhanced polarisation arising from the freely moving electron cloud of the metal nanoparticle known as the 'EM factor'.⁷⁵

However, areas of increased electron density can be formed by bringing the nanoparticles together (aggregating) causing the plasmons to couple. This leads to greater scattering from molecules confined at these sites. These areas are known as 'hot spots' and can be purposely created by employing nanoparticle self-assembly (Figure 1.19).⁷⁷

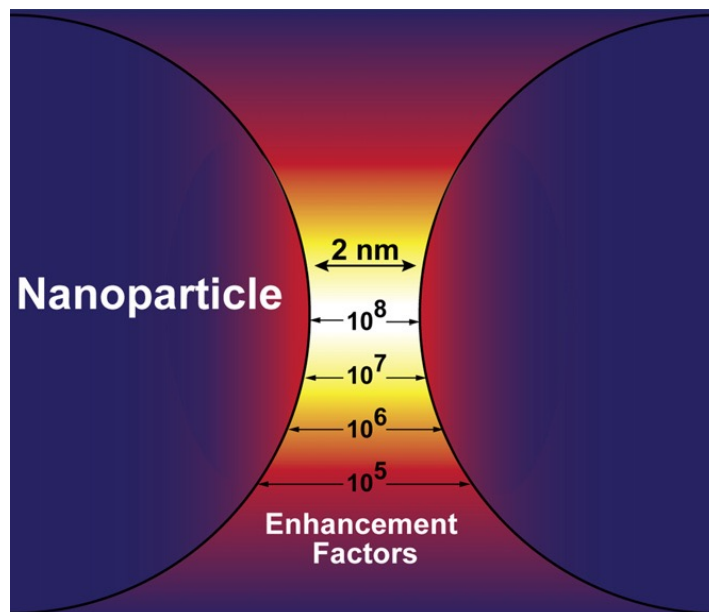


Figure 1.19 An illustration of a 'hot spot' formed when nanoparticles are in close contact with each other and the change in enhancement factor due to distance of the particles.⁷⁷

Self-assembly can greatly enhance the Raman signal due to an increase in formation of 'hot spots' which is advantageous in SERS sensing applications. The nanoparticle assemblies can be functionalised with a Raman reporter which can be tracked biologically or used as probes to give an enhanced Raman signature of the surrounding biological environment and molecules.⁷⁸⁻⁸² The production of 'hot spots' also red-shifts the plasmon, this is advantageous in biological applications where tissues have minimal absorption close to the NIR region.^{44,83}

By using SERS, we enable the monitoring of nanoparticle assemblies and as mentioned above can then utilise self-assembly in a number of healthcare applications. However, whilst tracking the nanoparticles is essential, it is also possible to realise secondary effects such as light-to-heat conversion (photothermal conversion) in order to give the nanoparticles a therapeutic application.

Photothermal applications

For photothermal applications, gold nanoparticles are mainly used due their biocompatibility, ease of surface modification with a desired molecule, their tuneable plasmon and their efficient light-to-heat conversion.

Gold nanoparticles can convert light into heat through a nonradiative process. El-Sayed studied the photothermal properties of gold.⁸⁴ By using femtosecond transient absorption spectroscopy, they found that when a particle is excited with a laser, a heated electron gas is formed, this then cools rapidly by exchanging the energy with the nanoparticle lattice. The nanoparticles then cool down by transferring energy to the surrounding medium. Furthermore, if the lattice heats up faster than it cools, structural changes of the nanoparticles can be observed due to the accumulation of heat in the lattice.⁸⁵ Although the nanoparticles are capable of converting light to heat efficiently, the current methods for calculating this conversion rate are not robust at the moment and require further investigation (Figure 1.20).⁸⁶ For nanoparticle clusters, the distribution of light energy is not homogeneous which means that 'hot spots' absorb an immense amount of light heat and the absorbance frequency has been shown to increase.⁸⁷ One other advantage of assembling nanoparticles is that the LSPR can be tuned into the NIR region. This is advantageous for biological applications as there is deeper penetration of the tissue therefore less absorption from the surface haemoglobin, melanin and water.

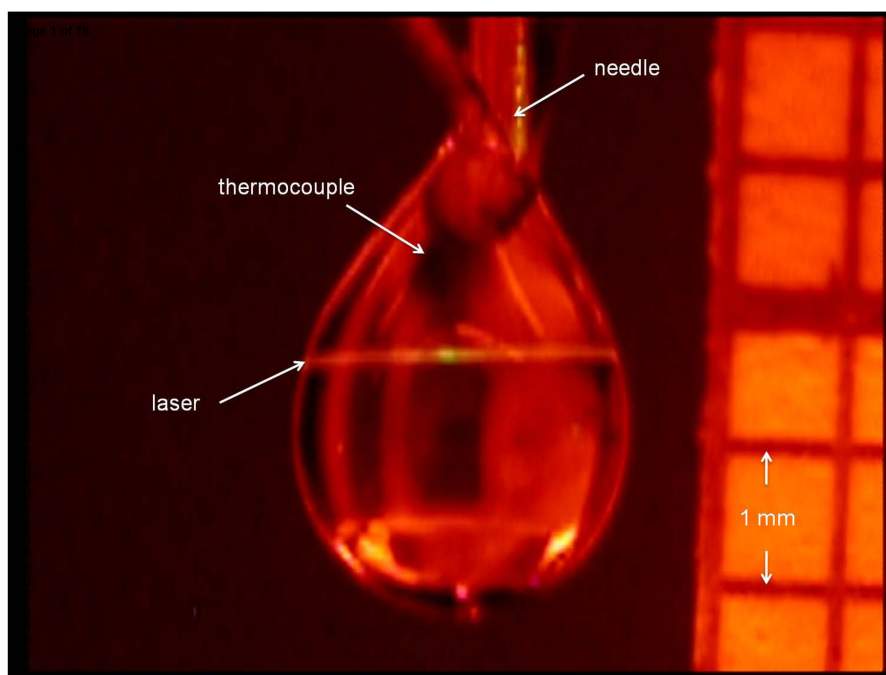


Figure 1.20 An image taken from Ref. 86 of a typical water droplet. This is one of the experimental set ups that can be used to test for the light to heat efficiency.

There are a few examples in the literature of photothermal therapy using self-assembly of gold nanoparticles to irradiate cancer cells. Thermally sensitive elastin-like polypeptides (ELP) were functionalised onto 20 nm gold nanoparticles (AuNP) (Figure 1.21).⁸⁸ When heated with a laser, the nanoparticles would assemble and their plasmon resonance would shift towards the NIR region. Photothermal studies of *in vitro* models with cancerous cells showed that the presence of these ELP-AuNPs nanoparticles caused the cancerous cells to die compared to no cell death shown in PEGylated nanoparticles of the same size. Furthermore, thermal imaging of *in vivo* modelling showed that these NIR photo transducers heated up by 28 °C compared to just 10°C in the PEGylated nanoparticles. Moreover, *in vivo* photothermal therapy with the ELP-AuNPs showed that the tumours were abolished after 7 mins of irradiation with the laser.

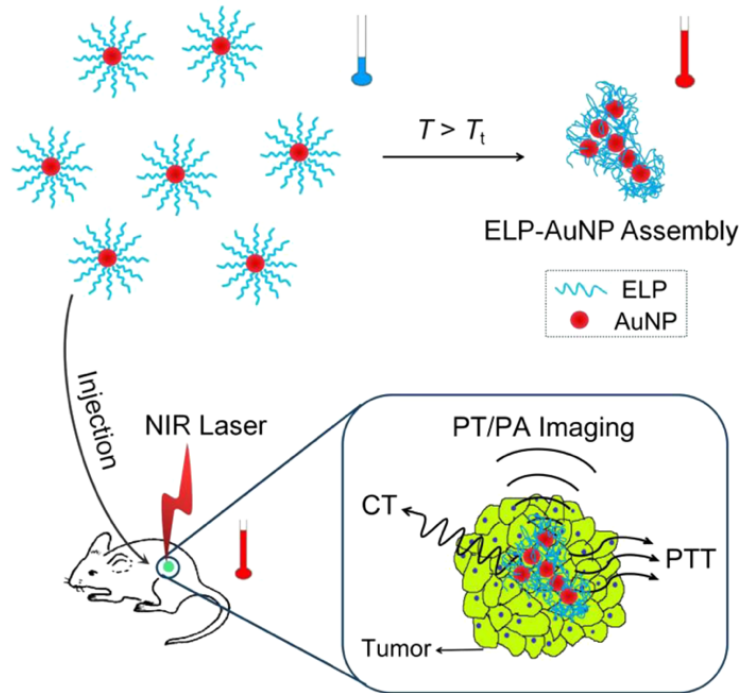
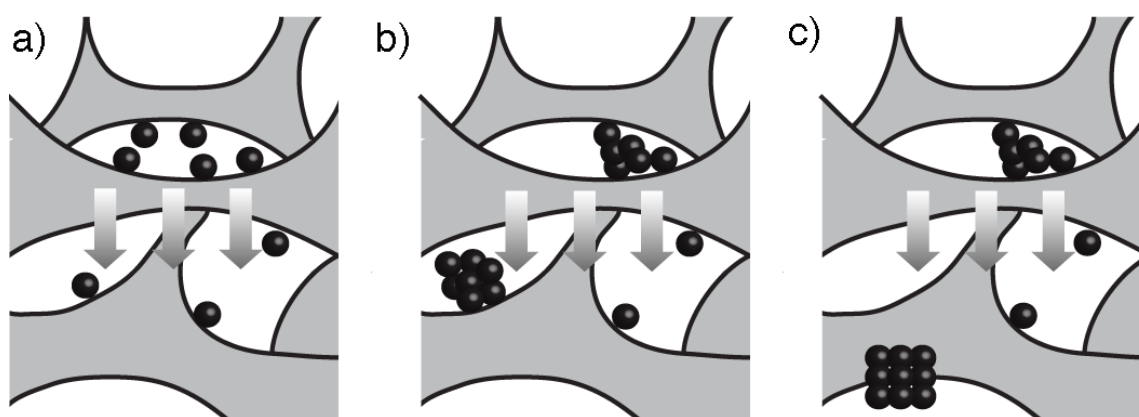


Figure 1.21 Schematic representation of the thermally triggered nanoparticles in vitro and in vivo.⁸⁸

Another group showed that small nanoparticles (<5 nm) could be assembled into chains from a DNA template and functionalised with a cancer cell receptor binding peptide.⁸⁹ These particles had superior photoacoustic properties and a comparable heat conversion rate compared to nanorods. The advantage of using small nanoparticles over larger ones is that eventually the DNA linkers would disintegrate in the body and thus the smaller nanoparticles can be cleared through the renal system.

These are great examples of how combining self-assembly with gold nanoparticles is a promising tool for use in theranostic therapies as they have both photoacoustic and photothermal properties.

2. Self-assembly of gold supraparticles with crystallographically aligned and strongly coupled nanoparticle building blocks for SERS and photothermal therapy.



This work has been published in part to Chemical Science.

Contributing authors and their roles:

S.A Thompson²: Provided and cultured cells and assisted in photothermal therapies with cells

J. Gracie¹: Undergraduate student that synthesised initial starting nanoparticles

A.W. Wark¹: Completed the SERS and Raman experiments of the supraparticles and nanoparticle building blocks

R. de la Rica¹: Principal Investigator

¹ Department of Pure and Applied Chemistry, WestCHEM, University of Strathclyde, Technology and Innovation Centre, 99 George Street, Glasgow, G1 1RD, Scotland, UK.

² Department of Chemistry and Biochemistry, Hunter College-City University of New York, New York 10065, USA

2.1 Abstract

A new method is shown for self-assembling citrate-capped gold nanoparticles into supraparticles with crystallographically aligned building blocks. It consists of confining gold nanoparticles inside a cellulose acetate membrane. The constituent nanoparticles are in close contact in the superstructure, and therefore generate hot spots leading to intense surface-enhanced Raman scattering (SERS) signals. They also generate more plasmonic heat than their individual nanoparticle building blocks. The supraparticles are internalized by cells and show low cytotoxicity but can kill cancer cells when irradiated with a laser. This, along with the improved plasmonic properties arising from their assembly, makes the gold supraparticles promising materials for applications in bioimaging and nanomedicine.

2.2 Introduction

It has been discussed that gold nanoparticles are excellent building blocks for biomedical devices as their remarkable plasmonic properties allow them to be used in a wide range of applications such as diagnostic sensing and photothermal therapy.^{90,91} By assembling the particles into compact structures, the LSPR of neighbouring particles couple leading to the enhancement of the surrounding electromagnetic fields. This enhancement has been found to increase the signal of SERS,⁹² which has been utilized for in-vivo sensing. One added feature of gold nanoparticles is their capability to generate heat when irradiated with a monochromatic light source. When nanoparticles reside in close proximity to each other as observed in supraparticles, less energy is needed from the laser to heat up the particles thus the side effects from the incident light is minimized.⁹³ The combinations of these properties make gold supraparticles promising tools for use in theranostics.⁹⁴

Previous procedures for assembling supraparticles include drop-cast methods and methods of functionalizing the surface of the gold nanoparticles. Liao *et al* formed supercrystals by drop-casting gold nanoparticles onto a silicon wafer or an indium tin oxide glass chip and the substrate was placed into a moisture-saturated environment.⁹⁵ This was either left to dry for 12 h at room temperature (RTP) or in the oven for 3 h. Although the process created diverse well-defined shapes, limitations included the removal of the supercrystals from the substrate surface, without causing disruption of the self-assembled nanoparticles, as well as the need for dispersion into an aqueous solution. Other approaches include modifying the gold nanoparticles with biomolecules and assembling them through biospecific reactions. For example, gold nanoparticles which have previously been modified with streptavidin, are then added to a biotinylated peptide framework. By utilizing the affinity of streptavidin for biotin, crystalline cubes of gold nanoparticles could be formed.⁵⁹ The construction of these crystalline cubes give an outstanding degree of control over the structure however, the inter-particle separation is several nanometres and their surface functionalisation adversely affects their plasmon coupling more than the drop-casted supraparticles.

In this chapter, a new method for assembly of gold nanoparticles into supraparticles is reported. This simple and effective method yields supraparticles with crystallographically aligned building blocks that are also biocompatible. This process was inspired by the mesocrystals commonly found in nature such as the skeletal plates in the sea urchin spine. Mesocrystals is a shortened term for 'mesoscopically structured crystal'. These suprastructures are not formed through classical crystalline formation but go through particle-mediated growth where their structure is made up of nanoparticle building blocks that are crystallographically aligned.^{96,97} These particles exhibit scattering properties similar to that of a single crystal. The primary particles go through a precursor stage where there is usually a polymer or organic matrix that facilitates the nucleation, growth and the oriented attachment of the nanoparticle building blocks.⁹⁷ Previous research has shown that calcium carbonate supraparticles can be grown using calcium acetate (CA) scaffolds in the presence of poly(acrylic acid).⁹⁸ Furthermore, another group has found that calcium carbonate supraparticles can be grown through aggregation-mediated crystallization in the presence of a N-trimethylammonium derivative of hydroxyethyl cellulose.⁹⁹ Using these findings, it was proposed that supraparticles could be prepared by confining citrate capped gold nanoparticles through a CA membrane. The supraparticles produced have shown enhanced plasmonic properties, desirable for SERS and photothermal therapy applications.

2.3 Experimental

2.3.1 Materials

All materials were obtained from commercial sources such as Sigma Aldrich and VWR. Cell lines for cell studies were gifted from Dr. Eileen Gentleman, King's College London, UK

2.3.2 Synthesis of nanoparticle building blocks and assembly of gold supraparticles

Citrate-capped nanoparticles were obtained by adding 57.5 mg of sodium citrate dissolved in 7.5 mL of water to 500 mL of boiling water containing 60.5 mg of sodium tetrachloroaurate under continuous stirring. The mixture was boiled for 15 min. This method yields citrate-capped gold nanoparticles. The nanoparticle solution was left at room temperature for several days before assembling supraparticles. To obtain supraparticles, 40 mL of the nanoparticle solution was filtered with a syringe through a cellulose acetate membrane (0.2 mm cut-off, VWR) at room temperature (18–22 °C).

2.3.3 Electron microscopy imaging

1–2 mL of sample was dried on a carbon grid. TEM imaging was performed with a FEI Tecnai T20 TEM operating at an acceleration voltage of 200 kV. SEM imaging was performed with a FEI Quanta 250 FEG-ESEM. 20 mL of water was filtered through the membranes prior to SEM imaging in order to remove any salts and loosely bound nanoparticles.

2.3.4 Dark field microscopy (DFM) and SERS experiments

Glass slides were cleaned by ultrasonic treatment in acetone for 5 min followed by rinsing with ethanol, deionized water and drying with nitrogen. The slides were then immersed in Hellmanex™ for at least 1 h, rinsed with abundant water and dried with nitrogen. Subsequently the slides were then immersed in a 1% (v/v) solution of poly(diallyldimethylammonium chloride) (PDDA) for 30 min. The

slides were rinsed with deionized water and dried with nitrogen. 100 mL of nanoparticle solution (either containing supraparticles or a suspension of the smaller nanoparticle building blocks) was placed onto the substrates for 10 min. The nanoparticles were adsorbed onto the PPDA- covered slide due to the electrostatic interaction between the citrate-capped nanoparticles and positively charged glass surface. After 10 min the slides were rinsed with water first and then dried with nitrogen. This prevents the formation of drying- induced aggregates being present on the slide surface. The slides were then covered with 1 μ M malachite green solution (diluted from a 1M stock solution in ethanol) for 10 min, rinsed with water and dried with nitrogen.

Correlated dark-field and SERS imaging was performed on two different microscopes with reference marks on the slide surface used to identify different regions. Raman maps were obtained using a confocal WITec Alpha300R instrument at 633 nm excitation. All maps were acquired using a 100x objective (Olympus MPlan, NA=0.9). Areas up to 20 x 20 μ m in size were imaged in \sim 0.4 μ m steps. An incident laser power of \sim 0.9 mW and signal integration time of 0.15 s was used. The SERS maps were created by plotting the difference between the maximum and minimum intensities in the 1020–1185 cm^{-1} window, targeting the peak at 1172 cm^{-1} and a preceding background region of the spectrum. The same image acquisition conditions were used (e.g. incident light intensity, integration time) for both the supraparticle and control slides when performing the SERS measurements to enable a direct comparison of relative Raman intensities. However, to prove that the nanoparticle building blocks are present on the slide an integration was increased to 0.75 s.

Dark-field images were acquired using a Nikon Eclipse LV100 with a 50x objective (Nikon CFI LU Plan BD ELWD, NA $\frac{1}{4}$ 0.55) in an epi dark-field configuration. Images were acquired using a Coolsnap camera and using the same source light intensity and exposure times.

2.3.5 Cell culture and supraparticle/nanoparticle internalization

The nanoparticles and supraparticles were modified with thiolated PEG (MW = 5000) in order to avoid their aggregation in cell media. Cells were incubated with nanoparticles or supraparticles at the same nanoparticle concentration (same absorbance at 400 nm). GFP-expressing bone cancer MG-63 was kindly gifted from Dr. Eileen Gentleman, King's College London, UK. Both cell lines were grown in Dulbecco's modified Eagle's medium supplemented with 10% Fetal bovine serum (FBS). Cells were maintained at 37 °C in a 5% CO₂ humidified environment. Cells were trypsinized and placed on glass slides or Petri dishes two days prior to imaging or photothermal cell experiments. For imaging experiments, cells were incubated with nanoparticles or supraparticles for 36 hours (10 µL in 2 mL of medium). Incubations were performed in medium supplemented with 0.05% FBS. On the day of the experiment, the medium was removed and replaced with a new medium. Cytotoxicity and cell death assays were performed using trypan blue following common protocols described elsewhere.¹⁰⁰ Dark-field and florescent images were obtained with a Nikon Eclipse LV100 with a 20x objective.

2.3.6 Photothermal experiments

The day of the experiments, PC3 cancer cells were trypsinized and centrifugated 3x for 5 min at 1000 rpm. After the last centrifugation, the supernatant was removed, and cells were re-suspended in 50 mL of PBS. 2 µL of nanoparticles or supraparticles were added to the cell solution before irradiation (2 mL of PBS was added to the control cells). A green continuous wave He-ion laser (515 nm, 27 mW at the focus point) was used to irradiate the different samples for 15 min. To measure the increase in temperature generated by plasmonic heat, 20 µL of nanoparticles or supraparticles were irradiated with the laser for 1 min. For the near IR photo thermal experiment, a 785 nm red laser was used (235 mW at the point of incidence) and the sample irradiated for 2 min 30 s. The temperature of the drop was measured with a thermocouple (Digital Meter, model 6802 II).

2.4 Results and Discussion

Fabrication of gold supraparticles

Gold supraparticles were formed by filtering 40 nm citrate capped gold nanoparticles (Experimental 2.3.2) through a CA membrane at RTP (Figure 2.1a). The CA membrane has a cut off pore size of 0.2 μm resulting from overlapping holes in the 3D mesh (Figure 2.1b). The initial λ_{max} of the nanoparticle building blocks is 531 nm this is typical of nanoparticles sized 40 nm.¹⁰¹

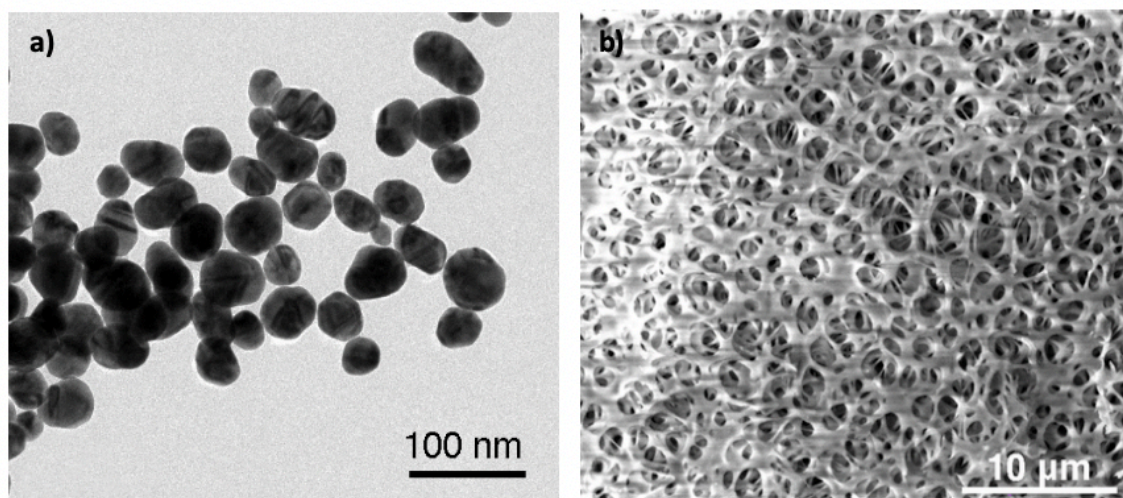


Figure 2.1 a) TEM image of citrate capped gold nanoparticle building blocks. The average diameter for the gold nanoparticle building blocks is 40 nm. b) SEM image of the cellulose acetate membrane.

After filtering through the membrane, the solution was centrifuged for 3 min at 1000 rpm, the supernatant was then removed and the remaining supraparticles were dispersed into deionized water. The extinction spectra of the nanoparticle building blocks compared to the supraparticles show a red- shift in λ_{max} and a broadening of the peak (Figure 2.2). This shift suggests that there is a population of larger particles has formed within the solution as aggregation would cause a complete dampening of the peak. The filtered nanoparticles were further analysed with transmission electron microscopy (TEM), which proved that a new population of larger nanoparticles were present in the solution that had not been observed prior to filtering (Figure 2.3a and Figure 2.3b).

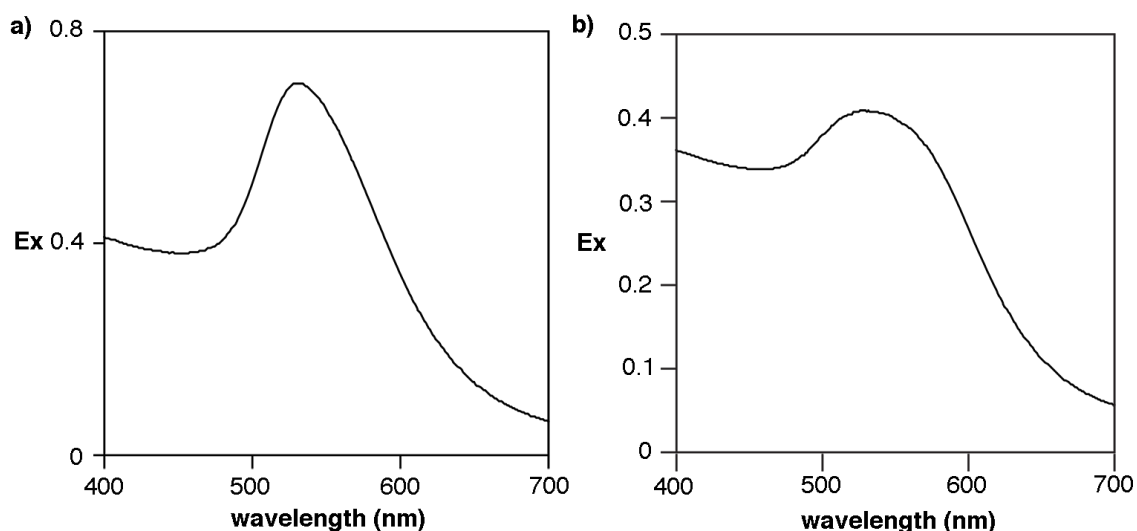


Figure 2.2 Extinction spectra of a) nanoparticle building blocks before filtering and b) gold supraparticles obtained from the solution after filtering. The supraparticle solution was centrifuged for 3 min at 1000 rpm, the supernatant was then removed and the remaining supraparticle solution was dispersed in MilliQ water.

The slow centrifugation of the sample resulted in a size separation between the larger heavier supraparticles and the smaller individual nanoparticles, although some smaller nanoparticles still remain in solution. A size distribution plot based on TEM analysis showed that the new larger particles ranged from 0.3 μm to 0.6 μm (Figure 2.3c). The selected area electron (SAED) pattern of one supraparticle gave a single spot diffraction which indicates that the new larger particles are made of gold (Figure 2.4a). This type of SAED patterning is also characteristic of a single crystal as polycrystalline and amorphous materials yield multi-dot and ring diffraction patterns respectively due to the multiple orientations of their crystalline faces with respect to the incident e-beam.^{102,103} High-resolution TEM imaging (Figure 2.3) and SEM images (Figure 2.4b and inset) of the supraparticle shows a roughened surface and areas of varying electron densities that is in agreement with the idea that the larger particles are composed of highly packed smaller nanoparticle building blocks.

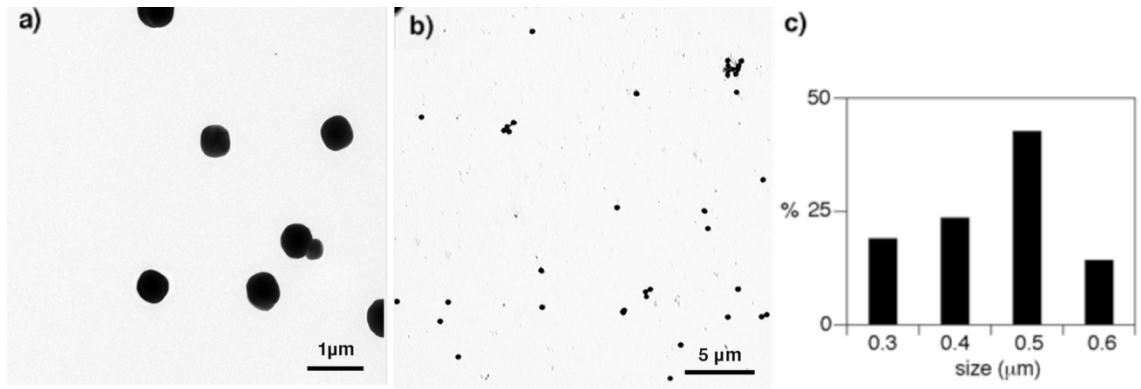


Figure 2.3 TEM images of the gold supraparticles at; a) 1 μm scale resolution and b) at 5 μm scale resolution c) size distribution plot of the supraparticles.

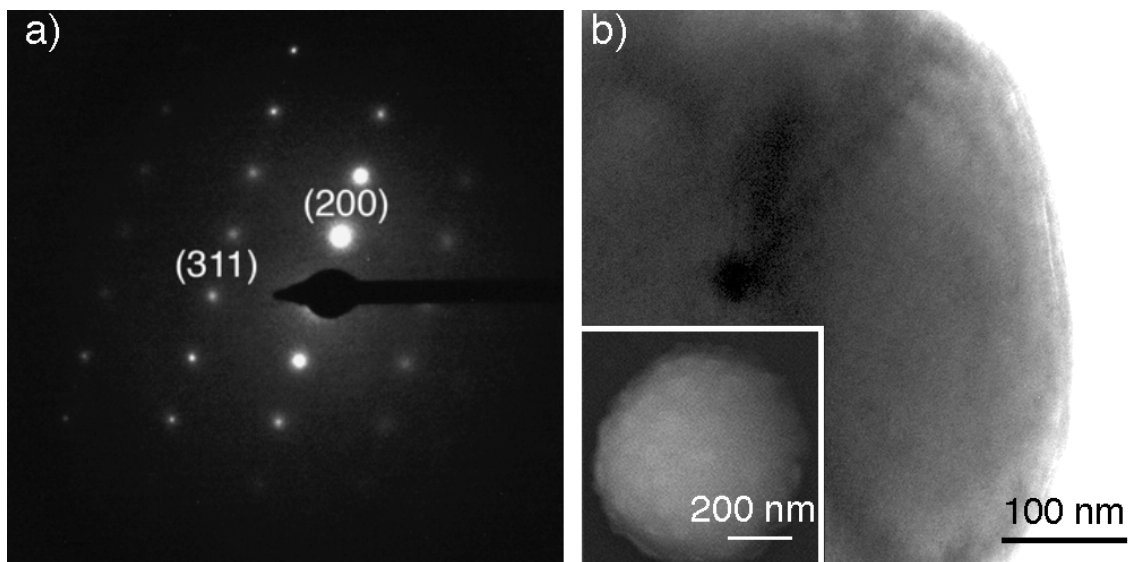


Figure 2.4 a) SAED pattern of a single supraparticle b) high-magnification of TEM image of a supraparticle. Scale bar 100 nm; inset: SEM image of a supraparticle. Scale bar = 200 nm

Two possible hypotheses were made on how the supraparticles were formed. The first hypothesis was that as the gold nanoparticle building blocks pass through the CA membrane, they go through an Ostwald ripening process inside the filter. This process requires the dissolution of the nanoparticles followed by their regrowth as a larger single-crystal particle. However, the process is carried out at room temperature (18°C – 22°C) therefore it is highly unlikely that this would happen as high temperatures are required for the Ostwald ripening of citrate capped gold nanoparticles.¹⁰⁴ Ostwald ripening also happens at longer timescales, the formation of supraparticles occurs within seconds of the nanoparticle passing through the

filer, thus another reason that Ostwald ripening is unlikely. The second hypothesis is that the gold nanoparticle building blocks have crystallographically aligned to form a mesocrystal. Mesocrystals can be identified by their single crystal diffraction pattern.⁹⁶ This hypothesis seems most likely as the supraparticle SAED pattern (Figure 2.4a) produced a single crystal diffraction pattern and the roughened surface of the supraparticle show smaller nanoparticle building blocks.

Raman characterization of gold supraparticles

Further analysis through surface enhanced Raman scattering (SERS) was undertaken. Figure 2.5 shows the bulk SERS spectra of malachite green isothiocyanate with the nanoparticle building blocks. Malachite green was chosen as the Raman dye as the thiol group of the molecule is known to interact strongly onto the surface of gold.

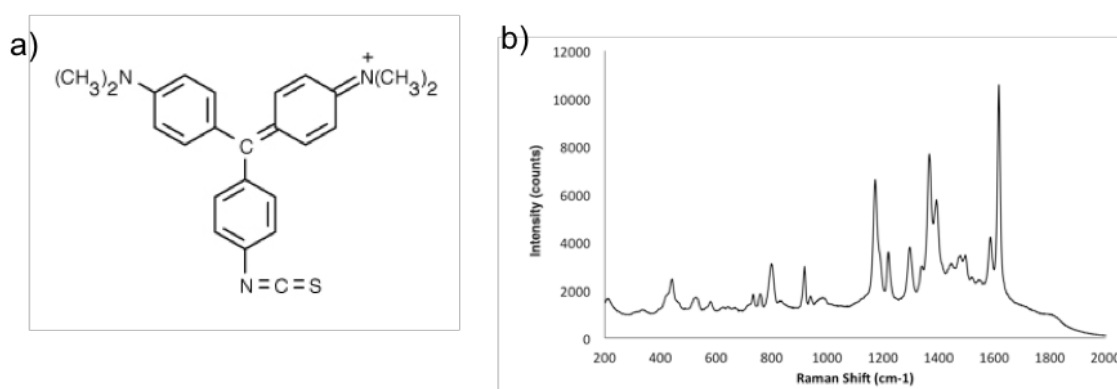


Figure 2.5 a) Molecular structure of malachite green isothiocyanate and b) Bulk Raman spectrum of a solution of 40 nm gold nanoparticle building blocks functionalized with 1 μM malachite green isothiocyanate, obtained through a Snowy Range Instrument (model Sierra 2.0, Excitation wavelength of 638 nm, acquisition time 3 s).

The SERS signal produced from the gold nanoparticle building units were compared against the supraparticles. It is predicted that there should be an enhancement of signal in the supraparticles due to the formation of 'hotspots' from the coupling of electromagnetic fields. Single particle analysis had to be undertaken between the supraparticles and the nanoparticle building blocks due to the difficulty in completely separating out the building blocks from the supraparticle solution. The colloids were functionalized with malachite green isothiocyanate (Figure 2.5) and then immobilized onto a PDDA-coated glass slide, a positively charged polymer. Careful consideration was made to not let the slides dry down therefore reducing the drying effects of uncontrolled aggregation. Dark-field microscopy images (DFM) and SERS maps of the supraparticles and the gold nanoparticle building blocks are shown in Figure 2.6 and Figure 2.7. These images were taken under the same conditions and the contrast unaltered unless stated. From the images, it is evident that the supraparticles are considerably more SERS active than their nanoparticle building blocks. The SERS spectra shown in Figure 2.6 shows that the supraparticles generate a signal several magnitudes higher than the individual 40 nm gold nanoparticles. This large increase in SERS signal agrees well with the formation of 'hot spots' that occur when the interstices of metallic nanoparticles are in close proximity of each other thus creating a region of highly localized enhanced electromagnetic fields. From the TEM images combined with the SERS results, this shows that the supraparticles are mesocrystals formed from strongly coupled smaller nanoparticle building blocks.

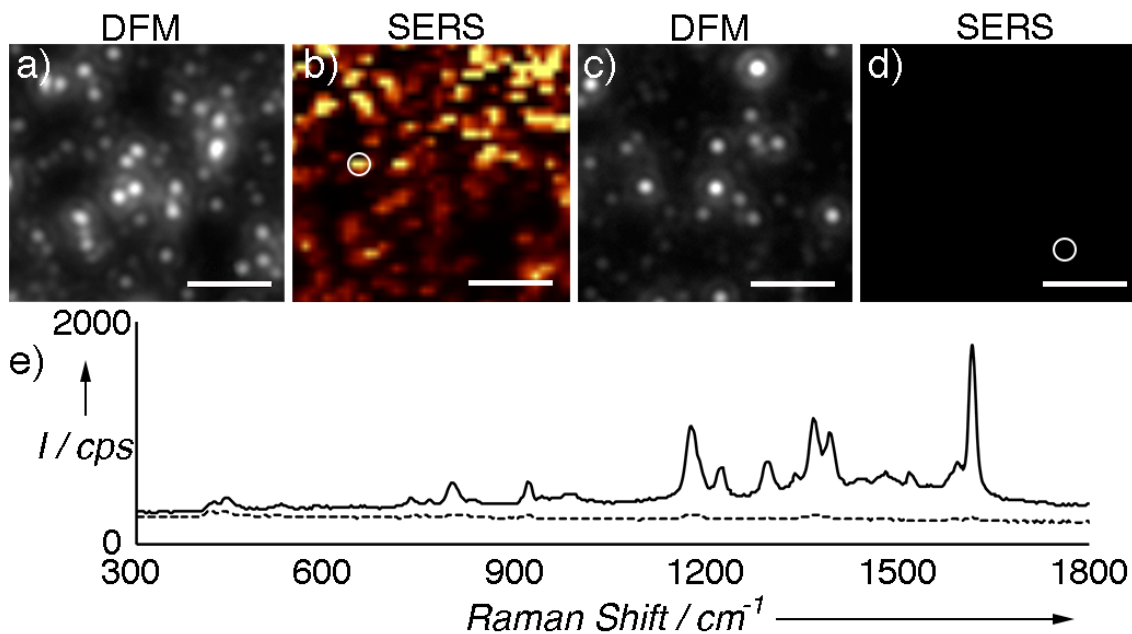


Figure 2.6 SERS analysis of the supraparticles and nanoparticle building blocks modified with malachite green isothiocyanate; a) dark-field microscopy image (DFM) and b) SERS map of the supraparticles immobilised onto a glass slide; c) DFM image of the 40 nm gold nanoparticles and d) SERS map of the nanoparticle building blocks; e) SERS spectrum of the supraparticles (solid black line, highlighted with a circle in b)) and the nanoparticle building blocks (dotted black line, highlighted with a circle d)). The SERS images generated were from the analysis of the peak intensity at 1172 cm^{-1} with respect to the background signal. The brightest spots correspond to an intensity of >300 counts per second (cps). Scale bars = 5 μm .

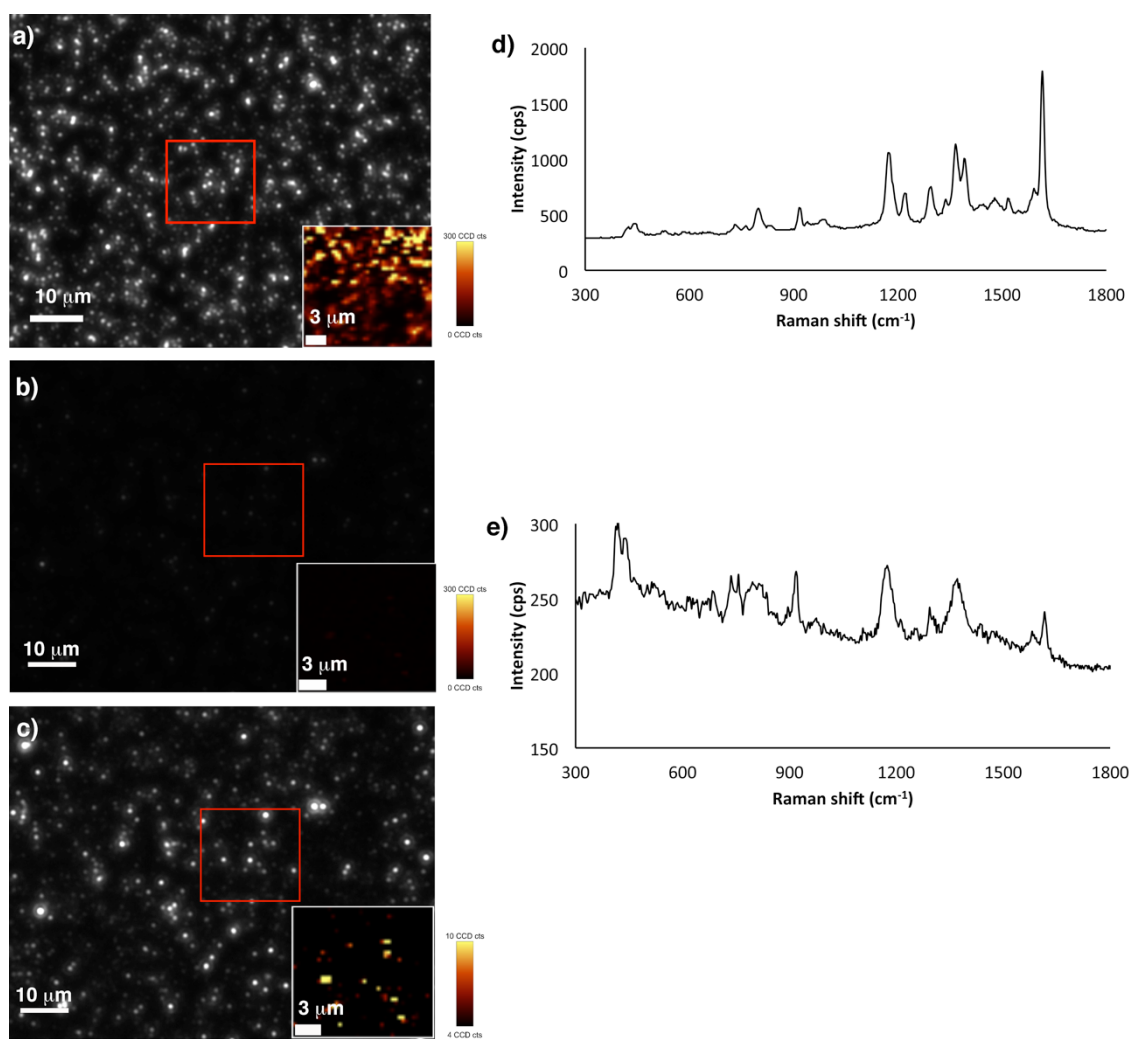


Figure 2.7 Dark field microscopy (DFM) and SERS maps (insets are taken from the red square area) of: a) sample containing supraparticles; b) and c) sample with nanoparticle building units; d) and e) shows SERS spectrums of a) and b) respectively. The images taken from a) and b) are under the same conditions. The lower scattering intensity shown in b) compared to a) is due to the nanoparticle building blocks being smaller than the supraparticles. In c) the integration time was increase from 0.15 s to 0.75 s and the contrast of the image enhanced. This allowed us to visualise the nanoparticles which are weaker scatterers due to their smaller size and non-assembly

Role of mechanism of supraparticles assembly

After demonstrating that the new population of larger particles are made up of smaller nanoparticles the mechanism of how the supraparticles assemble was studied. When a solution of 40 mL of 40 nm citrate-capped gold nanoparticles is pushed through the CA membrane, a residual red tint can be observed (Figure 2.8a). This suggests that the nanoparticles attach onto the surface of CA membrane. This correlates well with previous studies which have shown that citrate capped gold nanoparticles interact and attach to cellulose substrates via Van der Waals forces.¹⁰⁵⁻¹⁰⁹ The citrate-capped gold nanoparticles were then functionalized with carboxylated polyethylene glycol ligands (PEG). The PEG-capped gold nanoparticles also carry a negative charge but did not attach to the CA membrane (Figure 2.8c). For further analysis of possible interactions, citrate-capped gold nanoparticles were passed through a polyethersufone (PES) membrane that had a similar pore cut-off size of 0.2 μm but a different chemical composition. The nanoparticles did not interact with the PES membrane (Figure 2.8b) nor were there supraparticles found in the resulting solution (Figure 2.9). SEM imaging of the resulting solution shows that only unorganized aggregates are present which commonly occurs when gold nanoparticles are left to dry on a carbon grid (Figure 2.9a). The UV-Vis spectrum of the solution before and after filtering also remains unchanged suggesting that their morphologies have stayed constant (Figure 2.9b). These findings indicate that the interactions between the cellulose of the membrane and the citrate surrounding the gold nanoparticles play a crucial role in the formation of supraparticles.

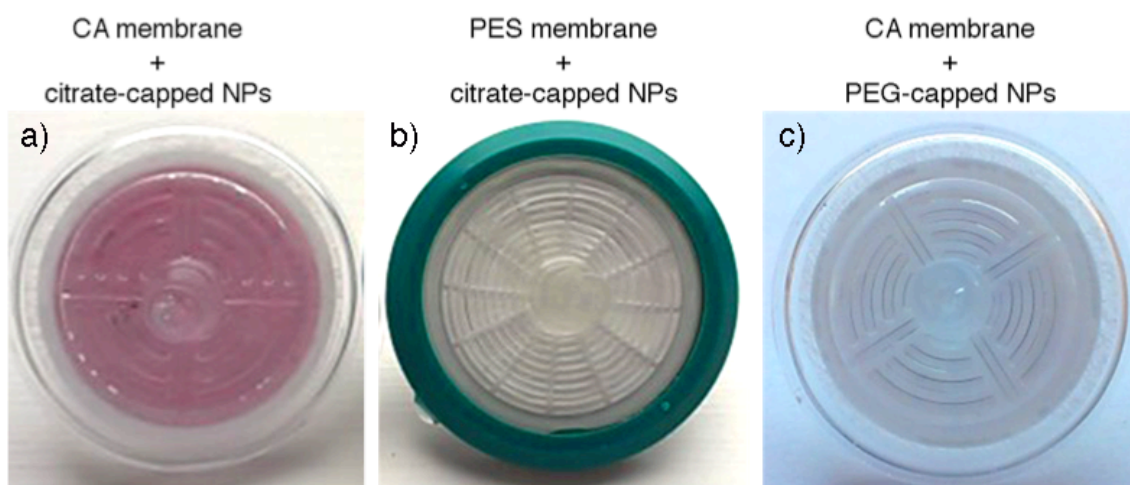


Figure 2.8 Images of the different membranes after filtering through 40 mL of citrate capped gold nanoparticles followed by 20 mL of deionised water; a) citrate-capped nanoparticles passed through cellulose acetate (CA) membrane; b) citrate-capped nanoparticles passed through a polyethersulfone (PES) membrane; c) carboxylated polyethylene glycol (PEG) functionalised nanoparticles passed through a CA membrane. Both filters have a cut-off pore size of 0.2 μm . The PEG-capped nanoparticles were obtained by adding 0.1 μM carboxy-PEG₁₂-thiol (ThermoFisher Scientific) to the citrate capped nanoparticles and left overnight.

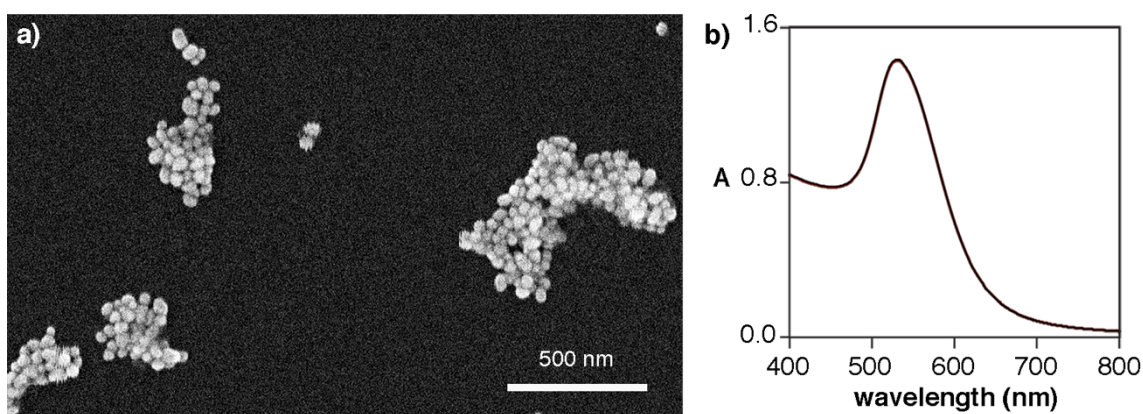


Figure 2.9 Analysis of the solution of 40 nm citrate-capped gold nanoparticles passed through the PES membrane; a) SEM image of the resulting solution; b) UV-Vis spectrum of the solution before filtering (black) and after filtering (red).

A section of the top and bottom of the saturated CA membrane was further investigated with SEM (Figure 2.10). From the images, small nanoparticle aggregates are observed on the top surface of the membrane (Figure 2.10a)

however, as the solution passes through the matrix, it is evident that larger more electron dense particles have formed accompanied with non-aggregated building blocks (Figure 2.10b). This suggests that the supraparticles form as the solution passes through the pores.

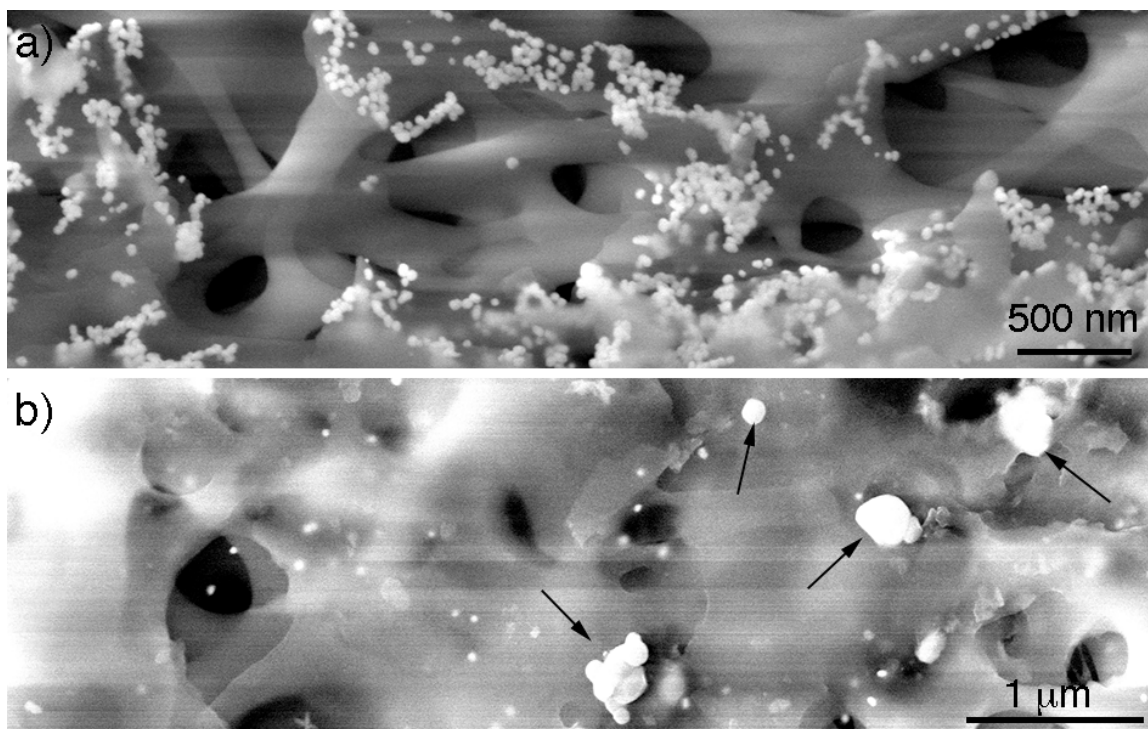


Figure 2.10 SEM of the CA membrane after filtering with the 40 nm citrate-capped gold nanoparticle building blocks; a) top of the CA membrane, the nanoparticle building blocks are seen interacting with the cellulose b) bottom of the CA membrane with arrows indicating the new population of larger particles.

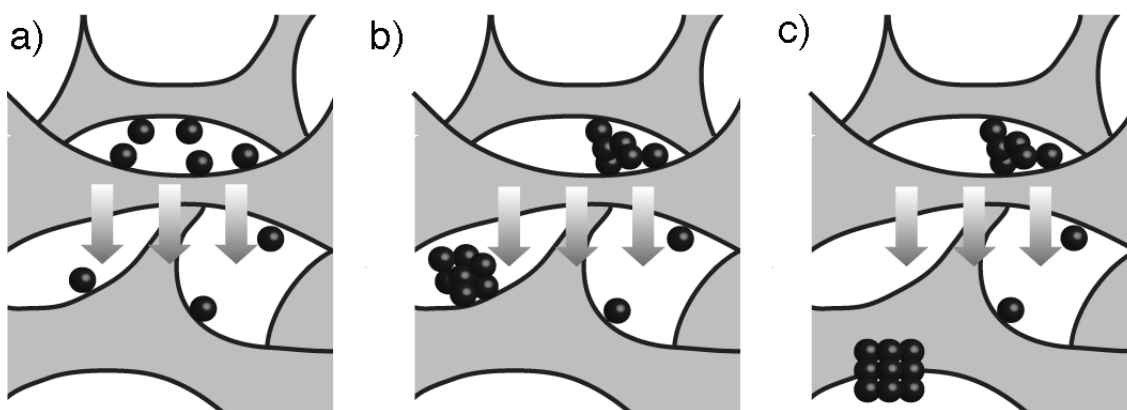


Figure 2.11 Schematic representation of supraparticle production; a) the nanoparticles are passed through the filter and attach onto the surface of the pores; b) the gradual increase in nanoparticle concentration leads to the formation of aggregates; c) the aggregates realign as they are passed through the matrix to generate crystallographically aligned supraparticles. The arrows represent the solution flow direction.

From the aforementioned observations, a proposed mechanism of gold supraparticle formation is schematized in Figure 2.11. As the gold nanoparticles pass through the filter they initially attach onto the surface of the membrane, this consequently reduces the pore size and the flow rate, which in turn increases the local concentration of nanoparticles around the pores. The increase in concentration leads to the formation of aggregates, which further reduces the pore size and flow rate. Eventually the pores become saturated; this is an important step for the formation of supraparticles as smaller 20 nm nanoparticles passing through the filter did not contribute to the production of supraparticles (Figure 2.12). While the aggregates are being pushed through the matrix, the nanoparticles align and reorganize into their crystal lattices to form mesocrystals evident from the SAED diffraction pattern of which is similar to that of a single crystal (Figure 2.4a). The nanoparticle building blocks are not perfectly spherical therefore they go through a self-selecting process as previous studies involving the self-assembly of nanocrystals have shown.^{110,111} When the free volume of the nanoparticle reduces, the slight repulsive interactions between the nanoparticles cause them to rearrange into a more energetically favourable configuration between the parallel surface facets.^{112,113} It has also been proposed that the orientated attachment of nanoparticles require a loss of ligand followed by lattice arrangement.^{114,115} The bulk solution SERS spectra of the supraparticles showed a less intense 1627 cm^{-1} peak (characteristic of citrate¹¹⁶) compared to a solution of gold nanoparticle

building blocks (Figure 2.13). Both solutions had a relatively similar concentration of nanoparticles which was estimated from the extinction at 400 nm. This decrease in intensity suggests that the supraparticles are assembled following a similar ligand displacement mechanism. The nanoparticle building blocks are also observed to arrange into dimers first then linear chains prior to the formation of supraparticles (Figure 2.10a) which suggests that one of the driving forces for self-assembly are dipole interactions.¹¹⁷

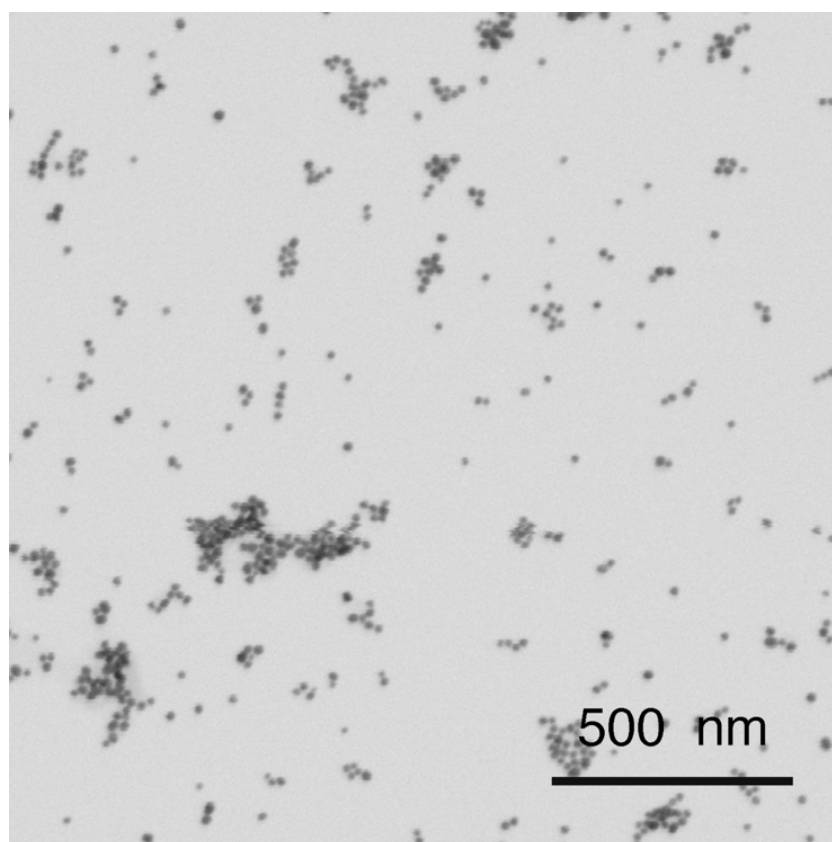


Figure 2.12 Electron microscopy image of 20 nm citrate-capped nanoparticles after filtering through the CA membrane. Only unorganized aggregates are observed, which occurs through drying of the sample.

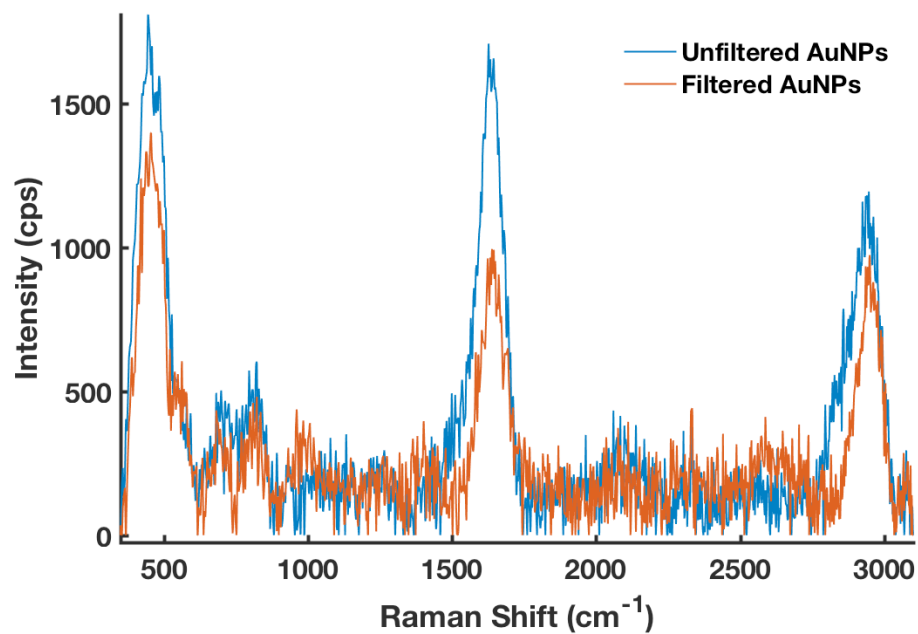


Figure 2.13 Bulk solution SERS spectra of the citrate-capped gold nanoparticles before (blue) and after (orange) through the CA membrane. Both samples had the same nanoparticle concentration estimated from the absorbance at 400 nm. Obtained through a Snowy Range Instrument (model Sierra 2.0, Excitation wavelength of 638 nm).

In vitro and photothermal studies with supraparticles

The supraparticles are formed through a biocompatible CA matrix; sub-micrometre in size; and dispersed in an aqueous solution. This makes them very promising candidates for further use in nanomedicine applications. However, before exploring their potential effectiveness in these applications, their cytotoxicity to cells was first studied. Prostate cancer cells expressing green fluorescent protein (GFP) were used because it was easy to visualize them using fluorescence microscopy. The cells were incubated with either supraparticles or nanoparticles and then washed three times (Figure 2.14). The particles were only visible in the cytoplasm of the cells thus indicating that they have been internalized. However, if they were attached to the outer membrane, they would also be visible in the nucleus. After 36 h the cells were stained with trypan blue to test cell viability. Only 1.7 ± 0.95 % of cell death occurred in the cells incubated with the supraparticles and 4.4 ± 1.8 % of cell death occurred in cells incubated with nanoparticles (Figure 2.15). This demonstrates that the supraparticles are highly biocompatible.

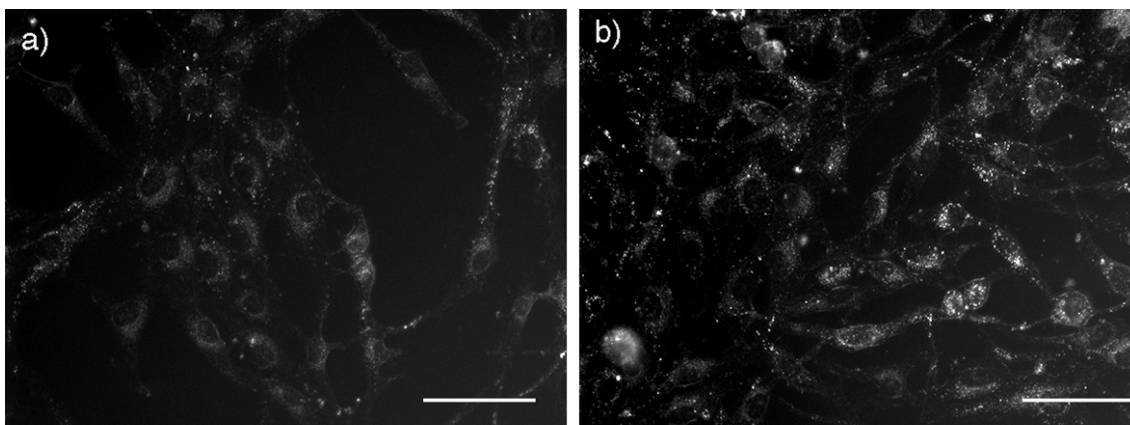


Figure 2.14 Supraparticle uptake by cells. Dark-field microscopy (DFM) images of prostate cancer cells, a) without supraparticles; b) with supraparticles; the increased contrast in b) compared to a) indicates that the supraparticles were internalized by the cells, the supraparticles are localized in the cytoplasm Scale bars: 100 μ m.

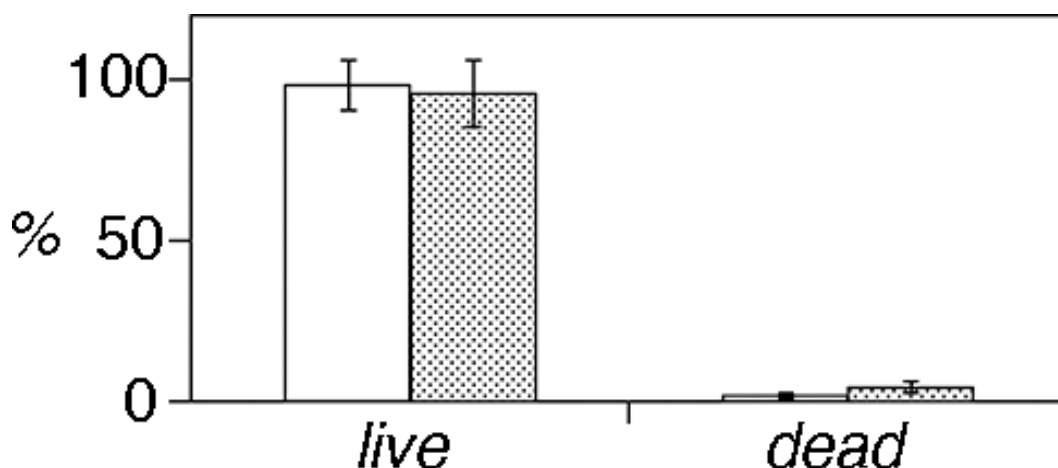


Figure 2.15 Cytotoxicity study of the supraparticles (white bars) and nanoparticles (dotted bars) after 36 h incubation with cancer cells after irradiating 20 mL of supraparticles or nanoparticle building blocks for 1 min with the 515 nm laser. The laser power incident onto the sample was 27 mW. Error bars are the standard deviation ($n \geq 3$).

Next, the photothermal properties of the supraparticles were compared to the nanoparticle building blocks. As both the nanoparticle building blocks and supraparticles absorb green light, a continuous-wave (CW) 515 nm laser was used to allow a direct comparison of the photothermal properties. Irradiating the plasmonic nanoheaters with the laser resulted in a linear increase in temperature followed by a plateau in which the temperature remained constant with time. Consequently, the samples of similar concentrations of gold were irradiated for only one minute where the change in temperature between the two samples changes linearly, this allows for a more accurate comparison. There was a 50% greater increase in temperature in the solution containing the supraparticles which demonstrates that the supraparticles are better photothermal transducers than their nanoparticle counterparts (Figure 2.17).

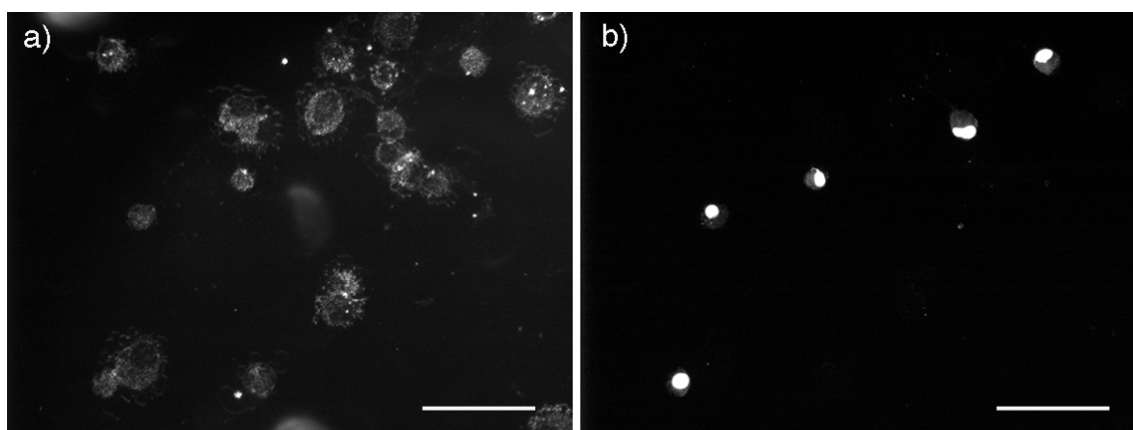


Figure 2.16 In-situ images of prostate cancer cells incubated with supraparticles after irradiating them in solution with a 515 nm laser for 15 minutes; a) dark-field microscopy images and b) correlated fluorescence microscopy images. Ethidium bromide was used to stain the nuclei in dead cells, the fluorescent cells in b) are dead. Scale bars: 100 μm .

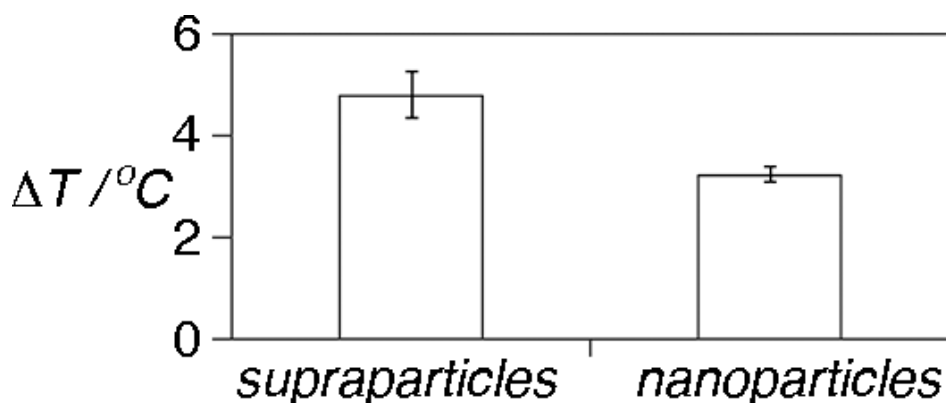


Figure 2.17 Increase in temperature measured after irradiating 20 μL of supraparticles or nanoparticle building blocks for 1 min with the 515 nm laser. The laser power incident onto the sample was 27 mW. Error bars are the standard deviation ($n \geq 3$).

After comparing the generation of heat from the supraparticles and nanoparticles, their ability to kill cancer cells via photothermal effects was studied further. The irradiation time was increased to 15 min to allow the supraparticles to reach their full photothermal effects. Supraparticles and nanoparticles building blocks of the same concentration were incubated with prostate cancer cells and the solution irradiated with the CW 515 nm laser. After 15 minutes, the cells that contained the supraparticles had 30% more cell death than the cells containing the nanoparticle building blocks ($13 \pm 3\%$ compared to $9 \pm 1\%$). It should be noted that as these experiments are carried out at room temperature ($22 - 23^\circ\text{C}$) therefore the overall solution temperature does rise above body temperature (37°C) therefore cell death

is attributed to localised heat produced from the nanoparticles. A control experiment was repeated without any particles present in the cells, only $5 \pm 1\%$ of cell death occurred demonstrating that cell death was due to the presence of plasmonic heat and not the laser. Although these experiments used a 515 nm laser to compare the photothermal properties of the nanoparticle building blocks and the supraparticles, in real nanomedicine applications a near-infrared laser would be desirable to use, as this would allow a deeper tissue penetration depth without overheating the irradiated area.^{118,119} Therefore, the photothermal response of the supraparticles was also repeated at 785 nm to show that the supraparticles could be heated in conditions commonly used in photothermal therapy (Figure 2.18)

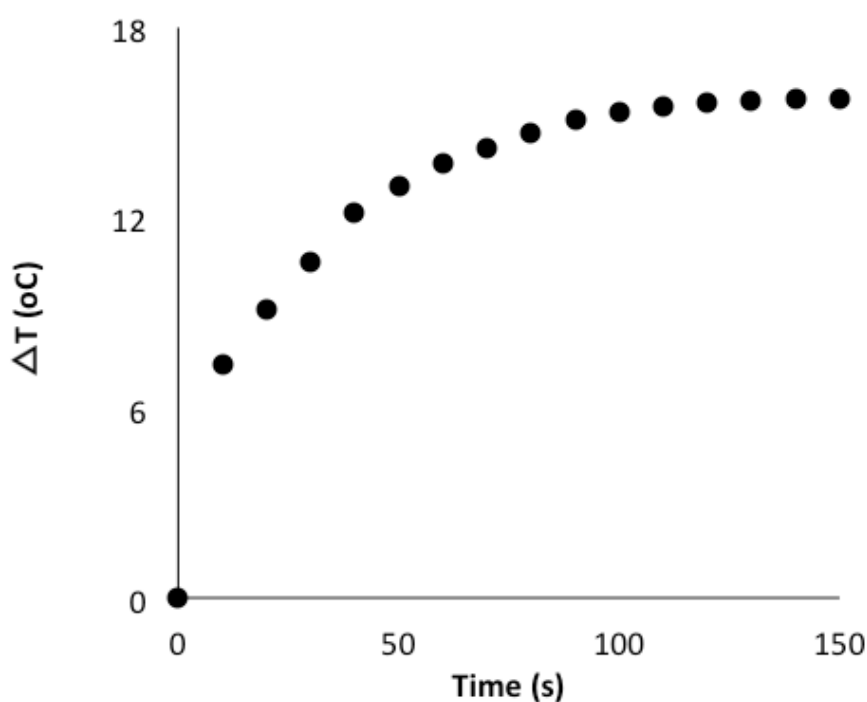


Figure 2.18 Increase in temperature generated by supraparticles irradiated with a 785 nm CW laser (235 mW at the point of incidence) as a function of irradiation time.

The energy required to heat up the nanoparticles can be calculated from the heat transfer equation:

$$Q = mc\Delta T$$

Eq. 1.7 Heat transfer equation

Q= Thermal energy (kJ)

m= mass (kg)

c= specific heat capacity (J)

ΔT =change in temperature

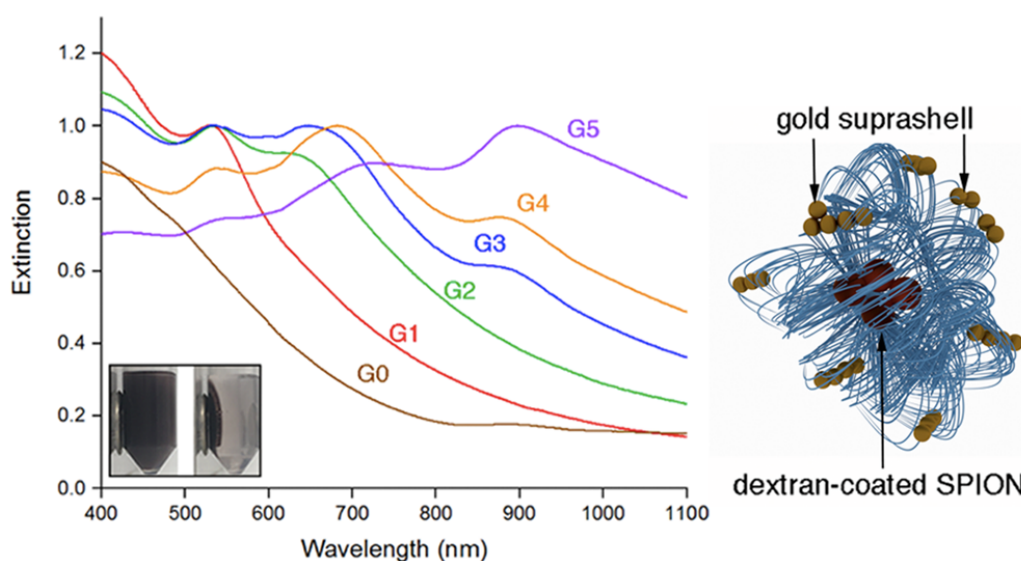
By assuming that the energy transfer of the particles to the water is 100%, the energy absorbed from the 515 nm laser can be calculated as 4.18×10^{-7} kJ and 2.5×10^{-7} kJ for the supraparticles and the nanoparticles respectively while the supraparticles absorbed 1.00×10^{-6} kJ using the 785 nm laser. The supraparticles were 48% more effective in absorbing energy compared to the 40 nm gold nanoparticles. This also supports the hypothesis for the formation of hotspots between particles contained within the supraparticles as larger particles would not absorb light as efficiently.

2.5 Conclusions and Further Work

In conclusion, it has been shown that citrate-capped nanoparticles can be assembled into supraparticles when filtered through a CA membrane. The supraparticles diffract like a single crystal, indicating that the building blocks are crystallographically aligned. Furthermore, the generation of 'hot spots' in the supraparticles increases the SERS response greatly and they have been shown to generate more plasmonic heat and kill cancer cells more effectively. These traits make the supraparticles promising candidates for use in bioapplications such as SERS-based diagnostics, photothermal therapy and plasmonic based theranostics.

For future work, it would be advantageous to repeat the photothermal cell experiments with a CW 785 laser using the same laser power as the 515 nm laser for a direct comparison of how this experiment might compare in a clinical setting. Another experiment would be to functionalize the supraparticles with a capture molecule to increase their selectivity and targeted responses and then to repeat cell experiments with a mixture of healthy and diseased cells.

3. Gold suprashells: enhanced photothermal nanoheaters with multiple LSPR for broadband SERS



This work has been published in part to The Journal of Physical Chemistry C

Contributing authors and their roles:

Sebastian A. Thomson²: Cell culture and provided help with internalising suprashells into the cells

Alastair A. Wark¹: SERS mapping experiments

Roberto de la Rica¹: Principal Investigator

¹. Department of Pure and Applied Chemistry, WestCHEM, University of Strathclyde, Technology and Innovation Centre, 99 George Street, Glasgow, G1 1RD, Scotland, UK.

². Department of Chemistry and Biochemistry, Hunter College-City University of New York, New York, New York 10065, US

3.1 Abstract

In this chapter, a new type of self-assembled plasmonic nanostructure, called gold suprashells is reported which are gold nanoparticles assembled around superparamagnetic iron oxide nanoparticle (SPION) core. Gold suprashells have multiple surface plasmon resonances over a broad vis-NIR wavelength range, which makes them useful in applications where broadband absorption is required. For example, suprashells are efficient substrates that enhance surface-enhanced Raman scattering signals across multiple excitation wavelengths. This unique multi-resonant character is afforded by the suprashell structure, which comprises anisotropic assemblies of nanoparticles with tuneable length. Furthermore, gold suprashells generate more heat when excited with a laser compared to the nanoparticle building blocks, therefore making them promising materials for photothermal applications. The suprashells can potentially be assembled onto any negatively charged core, which opens up multiple possibilities for the development of multifunctional core/suprashell nanoparticle designs. Here, we assemble gold suprashells around dextran-coated SPIONs in order to obtain plasmonic and magnetic nanoparticles. Cells that have internalized the multifunctional nanoparticles can be accumulated with a magnet and killed with a laser through the generation of plasmonic heat. This approach shows promise for the development of therapies aimed at killing circulating tumour cells by utilizing the proposed magnetic and plasmonic nanoparticles.

3.2 Introduction

Gold nanoparticles can generate heat when excited with light that is resonant to their localized surface plasmon resonance (LSPR).¹²⁰⁻¹²⁴ Since nanoparticles accumulate easily in leaky tumors,¹²⁵ the plasmonic heat generated by gold nanostructures can be utilized to selectively kill cancer cells. However, great precision is required for in vivo SERS and photothermal therapy because these approaches require irradiating the tissue with a laser, which has the potential to kill healthy cells as well as diseased tissue. Fortunately, the LSPR of gold nanoparticles can be tuned so they absorb near infrared (NIR) light.^{57,126} In this spectral region biological components absorb less and lasers have a greater penetration depth.¹²⁷ Moreover, if nanoparticles generate highly intense electric fields, lasers of lower power and shorter irradiation times can be used to excite them. This makes NIR absorbers containing intense electric fields ideal for nanomedicine because they reduce side-effects originating from shining a laser on the target tissue.

There are two strategies that are commonly used to obtain plasmonic nanoparticles resonant in the NIR that generate highly intense electric fields. The first approach consists in assembling spherical nanoparticles into compact clusters.¹²⁸ This shifts their LSPR towards longer wavelengths and generates plasmonic "hot spots" in which the electric field is several orders of magnitude higher than in the nanoparticle building blocks (Figure 3.1a (i) and (ii)).¹²⁹ The second approach requires growing anisotropic nanostructures, which generates NIR LSPR's and intensifies the electric field at the nanoparticle vertices.^{127,130} The main difference between these two nanostructures is that nanoparticle aggregates have broad and damped LSPR peaks whereas anisotropic nanoparticles have sharper resonances. In SERS, overlapping the extinction spectra of the nanoparticles and the target molecule results in more intense Raman signals.^{35,131} This is easier to achieve when the LSPR is broad. However, sharp peaks allow the nanoparticles to absorb more light when excited with a laser resonant with their LSPR. In this context, a new nanoparticle design with efficient broadband absorption could become a versatile platform for SERS because it would support

intense Raman signals of a wide range of molecules absorbing light at different wavelengths and when excited with different lasers. If the design included abundant hot spots, it could also improve photothermal applications, since the heat generated by plasmonic nanoparticles is directly proportional to the square of the electric field inside the metal.¹³²

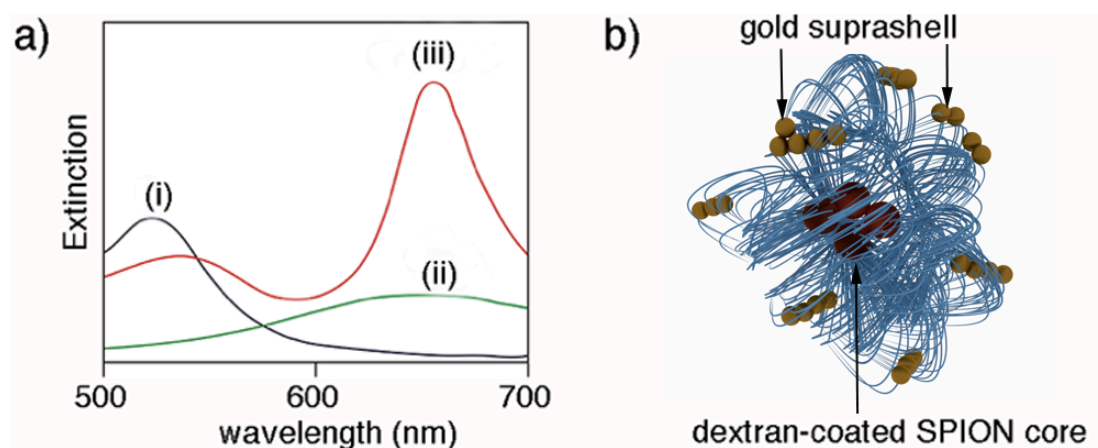


Figure 3.1 Schematic representation of (a) extinction spectrum of individual 20 nm gold nanoparticles (i); nanoparticle aggregates of uncontrolled morphology (ii), anisotropic assemblies of spherical nanoparticles (iii); (b) gold suprashells assembled on dextran-coated SPION

A new method for self-assembled plasmonic nanostructure called gold suprashells is proposed. The suprashells possess multiple surface plasmon resonances over a broad visible-NIR wavelength range. This multi-resonant character makes them useful for applications where broadband absorption is required. The suprashells consist of a collection of anisotropic assemblies of nanoparticles supported on a negatively charged core (Figure 3.1b). The anisotropic assemblies of gold nanoparticles have coupled surface plasmon resonances more similar to that of the longitudinal plasmon modes of gold nanorods than that associated with the random aggregation of spherical particles (Figure 3.1a (iii)).¹³³⁻¹³⁷ The absorbance wavelength of these coupled plasmon modes is intimately related to the length of the assemblies.¹³³⁻¹³⁷ Suprashells are made of anisotropic assemblies containing different numbers of nanoparticle building blocks, which result in multiple surface resonances over a wide range of wavelengths. This makes gold suprashells a versatile platform for SERS spectroscopy regardless of the

absorbance wavelength of the molecule under study.⁸¹ Furthermore, gold suprashells generate more heat when excited with a laser compared to the individual nanoparticle building blocks, therefore making them promising materials for photothermal applications. The suprashells can potentially be assembled onto any negatively charged core, which opens up multiple possibilities for the development of multifunctional core/suprashell nanoparticle designs. Here, the gold suprashells are assembled around dextran-coated superparamagnetic iron oxide nanoparticles (SPIONs) in order to obtain plasmonic and magnetic nanoparticles.¹³⁸⁻¹⁴² Cells that have internalized the multifunctional nanoparticles can be accumulated with a magnet and killed with a laser through the generation of plasmonic heat. This approach shows promise for the development of therapies aimed at killing circulating tumor cells (CTCs) utilizing the proposed magnetic and plasmonic nanoparticles.

3.3 Experimental

3.3.1 Materials

All starting materials were purchased from commercial sources such as Sigma Aldrich and VWR. Dextran-coated supraparamagnetic iron oxide nanoparticles (SPION) were purchased from micromod Partikeltechnologie GmbH.

3.3.2 Suprashell Assembly:

50 μL of 500 nm dextran-coated SPION modified with PEG ending in carboxylate group

s ($10 \text{ mg}\cdot\text{mL}^{-1}$ ($5.1\cdot 10^{10}$ particles mL^{-1}) micromod Partikeltechnologie GmbH) were added to 950 μL of 1% PDDA (diluted in Milli-Q water from a 35% stock solution, Sigma). After 20 min the samples were washed 4 times with water and 500 μL of gold nanoparticles (20 nm diameter, prepared via the Turkevich method⁷⁰ and concentrated by centrifugation to a concentration of 10 nM) were added to the SPIONs and left for 5 min followed by 4 additional washing steps. G2 to G5 were obtained by the addition of 500 μL of 1% PDDA and 500 μL of gold nanoparticles, each followed by 4 washing steps for each additional layer. The resulting solutions were diluted 5-fold and their vis-NIR spectra taken with a Cary 5000 spectrophotometer.

3.3.3 SERS

For the SERS experiments, 100 μL of 0.1 mM 2-naphthalenethiol in ethanol (Sigma Aldrich) was incubated overnight with 900 μL of the suprashell dispersion. All samples contained the same concentration of suprashells assembled on SPION, which was calculated via nanoparticle tracking analysis using a NanoSight LM10 (1.40×10^{10} particles mL^{-1}). The samples were then transferred to a glass vial where SERS spectra were obtained using two different Snowy Range Raman Spectrometers. The first instrument had an excitation wavelength of 638 nm and a spectral resolution of 8 cm^{-1} with an incident power set at 15 mW, and an

integration time of 10 s was used. The second instrument had an excitation wavelength of 785 nm and spectral resolution of 4 cm^{-1} with the laser power set to 15 mW and an integration time of 10 s. Background correction on all spectra was automatically calculated using the operating software (Peak).¹⁴³ Each spectrum was normalized with respect to an ethanol spectrum taken in identical conditions. This was done by dividing all spectra by the ethanol Raman peak intensity at 635 cm^{-1} .

3.3.4 SERS Mapping

Glass slides were cleaned by ultrasonic treatment in acetone for 5 min followed by rinsing with ethanol and deionized water and drying with nitrogen. The slides were then immersed in Hellmanex™ for at least 1 h, rinsed with abundant water and dried with nitrogen. Subsequently the slides were immersed in a 1% (v/v) solution of poly (diallyldimethylammonium chloride) (PDDA) for 30 min. The slides were then rinsed with deionized water and dried with nitrogen. 100 μL of the suprashell dispersion was placed onto the substrates for 10 min. The nanoparticles were adsorbed onto the PDDA-covered slide due to the electrostatic interaction between the citrate-capped nanoparticles and positively charged glass surface. The slides were then covered with 1 μM 2-naphtalenethiol solution for 10 minutes, rinsed with water and dried with nitrogen. Correlated dark-field and SERS imaging was performed on two different microscopes with reference marks on the slide surface used to identify different regions. Raman maps were obtained using a confocal WITec Alpha300R instrument at 633 nm excitation. All maps were acquired using a 100 \times objective (Olympus MPlan, NA = 0.9). Areas up to $20 \times 20\ \mu\text{m}$ in size were imaged in $\sim 0.6\ \mu\text{m}$ steps. An incident laser power of $\sim 0.9\ \text{mW}$, spot size $\sim 0.6\ \mu\text{m}$ and signal integration time of 1 s was used. The SERS maps were created by plotting the difference between the maximum and minimum intensities in the $980\text{-}1100\ \text{cm}^{-1}$ window, targeting the peak at $1064\ \text{cm}^{-1}$ and a preceding background region of the spectrum.

3.3.5 Scanning electron microscopy

2 μL of sample was left to dry on a carbon-coated grid (Agar Scientific). SEM imaging was then performed with a FEI Quanta 250 FEG-ESEM at an acceleration voltage of 25 kV.

3.3.6 Cell culture and Nanoparticle Internalization

Prostatic small cell carcinoma was grown in Dulbecco's modified Eagle's medium supplemented with 10% Fetal Bovine Serum (FBS). Cells were maintained at 37°C in a 5% CO_2 humidified environment. Cells were trypsinized and placed on glass slides or petri dishes for 2 days prior to imaging or photothermal experiments. For imaging experiments, cells were incubated with nanoparticles overnight or 36 h with nanoparticles (10 μL in 2 mL of medium). Incubations were performed in medium supplemented with 0.05% FBS. On the day of the experiment, the medium was removed and replaced with new medium. Cytotoxicity and cell death were studied with trypan blue or ethidium bromide following common protocols described elsewhere. They were determined to be lower than 5% after overnight incubation with a particle concentration of $7 \cdot 10^7$ particles $\cdot\text{mL}^{-1}$. Transmission dark-field microscopy images were obtained with a Nikon Eclipse LV100 with a 20x objective (Nikon S Plan Fluor ELWD, NA = 0.45).

3.3.7 Cell accumulation and photothermal experiments

To measure the increase in temperature triggered by plasmonic heat in suprashell dispersions, 20 μL of each sample was irradiated for 1 min with a CW laser (514 nm or 785 nm excitation wavelength, 27 mW at the point of incidence (514 nm) or 235 mW at the point of incidence (785 nm). The laser was focused into the sample with a 30 cm focal length PCX lens (514 nm) or with a 50 cm focal length PCX lens (785 nm). The temperature in the drop was measured with a thermocouple (Digital Meter, model 6802 II), which is a validated method for studying light-to-heat conversion in solutions of gold nanoparticles.⁸⁶ Cells were killed with plasmonic heat with the following procedure. The day of the experiments, cells already incubated overnight with nanoparticles were trypsinized and centrifuged 3 times for 5 min at 96 g. The cells were re-suspended in fresh complete medium (4 mL) in a 10 mL tube and a magnet was externally

placed in contact with the tube. The tube together with the magnet were placed on an orbital shaker for 5 min. Then, the medium was removed and recovered cells were re-suspended in 1 mL fresh medium and counted. For photothermal experiments, cancer cell pellets were formed by centrifugation and the medium was removed. A CW laser (785 nm, 235 mW at the point of incidence) was used to irradiate the cell pellet for different times (2, 5, 10, 15, 20, 25 and 30 min). Two controls were performed: cells without nanoparticles and 15 min irradiation time and cells with nanoparticles but no irradiation, which yielded $4.6 \pm 1\%$ and $4.8 \pm 1\%$ cell death, respectively. It is important to note that the laser must not directly touch the thermocouple as this will result in irregularly high readings.

3.4 Results and Discussion

Synthesis of the gold suprashells

Figure 3.2 shows a scheme for the method used for assembling gold suprashells onto the SPION. The magnetic cores consist of a cluster of iron oxide nanoparticles approximately 500 nm diameter covered with dextran and are obtained from a commercial source. The dextran is modified with polyethylene glycol molecules (PEG) ending in carboxylate groups that confer negative charge to the nanoparticles (zeta potential (ζ) = -21.7 mV). Positively charged poly(diallyldimethylammonium) (PDDA) molecules are electrostatically wrapped around the cores, which changes their surface charge (ζ = 22.3 mV). After washing away the excess PDDA with water, citrate-capped gold nanoparticles are added (20 nm diameter). The positively charged PDDA molecules surrounding the SPION cores trap the negatively charged gold nanoparticles and generate short anisotropic assemblies, in agreement with previous reports on the assembly of nanoparticles with polycations such as chitosan via a mechanism based on the nonuniform distribution of capping ligands.¹⁴⁴ Repeating the cycle of PDDA and gold nanoparticle additions, generates assemblies containing an increasing number of nanoparticle building blocks. Suprashells obtained with this procedure are named "GX", where X is the number of successive additions of PDDA and gold nanoparticle dual layers.

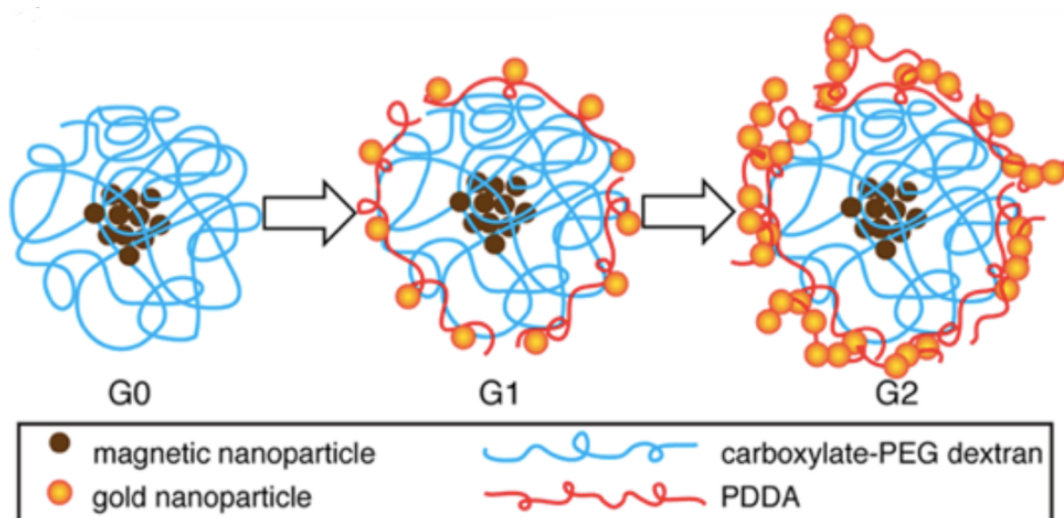


Figure 3.2 Schematic diagram showing the method used to obtain gold suprashells. Anisotropic assemblies of nanoparticles in the suprashells are self-assembled by means of electrostatic interactions between positively charged PDDA molecules and negatively charged gold nanoparticles. Suprashells containing assemblies of different length are named with the code "GX", where X is the number of successive additions of PDDA and gold nanoparticles leading to more extended assemblies.

Spectroscopic analysis of suprashells

Figure 3.3 shows the vis-NIR spectra of the magnetic gold suprashells obtained with the procedure detailed in Figure 3.2. All suprashells have a resonant peak around 530-540 nm, which corresponds to the LSPR of the gold nanoparticle building blocks (Figure 3.4). As the number of additional nanoparticle/polymer layers are increased from G1 to G5, new well-defined LSPR peaks emerge at increasingly red-shifted wavelengths extending into the NIR. The changing shapes of the extinction spectra with increasing layer number provides evidence of strong plasmonic coupling¹²⁹ with anisotropic assemblies of nanoparticles being favoured on the SPION surface rather than simple random aggregation. Recent theoretical and experimental^{133,135-137} studies on quasi-linear or chain-like assemblies of Au nanospheres all demonstrate similar trends to that observed in Figure 3.4. As anisotropic assembly occurs, a relatively small (~10-15 nm) red-shift and damping of the LSPR peak at ~530 nm is accompanied with the emergence of a higher intensity extinction peak at longer wavelengths in the >650 nm range. In a manner analogous to gold nanorods, the relative heights and widths of the LSPR peaks formed on anisotropic assembly depend on the relative length (number of particles) and width (degree of linearity, branch formation). In

contrast, isotropic 3D assemblies of nanoparticles would not be expected to exhibit a continual red-shift of a distinct LSPR peak into the NIR with increasing assembly size.¹⁴⁵ Additionally, it is possible that the spectral features observed in Figure 3.3 are also associated with higher order multipolar resonance such as quadrupoles. The observation of quadrupoles in far-field extinction spectra has been reported in non-spherical particles (e.g. cubes, rods¹⁴⁶) and considerably larger spherical particles featuring a low size dispersity.¹⁴⁷

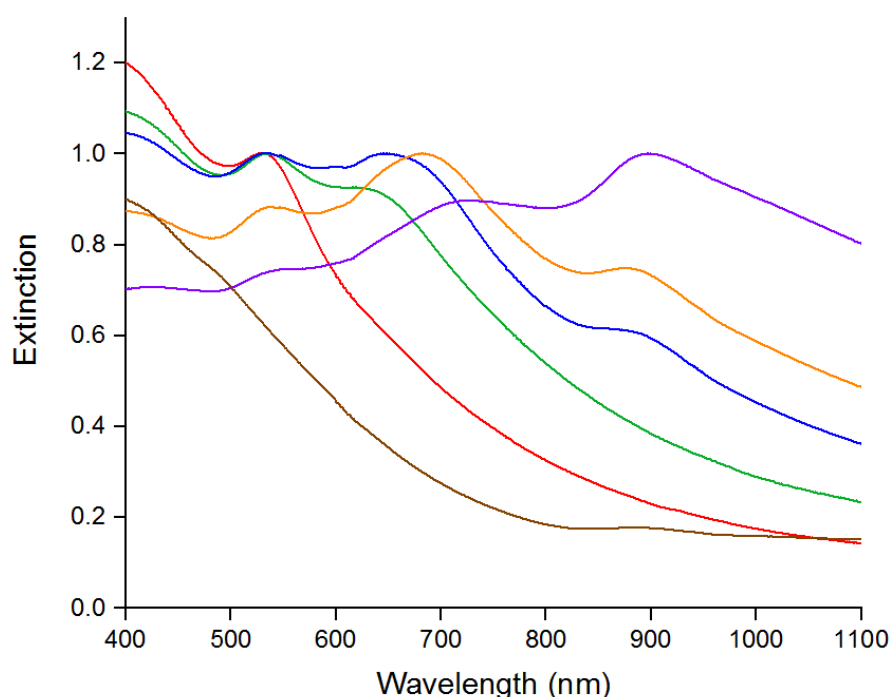


Figure 3.3 Vis-NIR spectra of G0 (brown), G1 (red), G2 (green), G3 (blue), G4 (orange) and G5 (purple).

There are some differences between previously reported studies on anisotropic nanoparticle assembly^{133,135-137} and the measurements reported here. First, it should be pointed out that the close proximity of the nanoparticles to the larger SPION will have a significant broadening and damping effect on the LSPR spectrum (compared to assemblies in suspension or on a glass support), which can be seen by comparing the colloidal and G1 spectra in Figure 3.4. Also, as the layer number increases, second and third LSPR peaks emerge, both of which red-shift and change intensities relative to nanoparticle assembly cycles. In particular, the latter most red-shifted peak forms at >900 nm for the G5 sample, with a continued relative decrease in the ~530 nm peak. This behaviour is evidence of

increasing anisotropy as the layer number increases. The observation of multiple resonance peaks above a broad background reflects that the nanoparticle assembly is unlikely to be highly uniform across the entire SPION substrate. This results in a unique multi-extinction over a wide range of wavelengths.

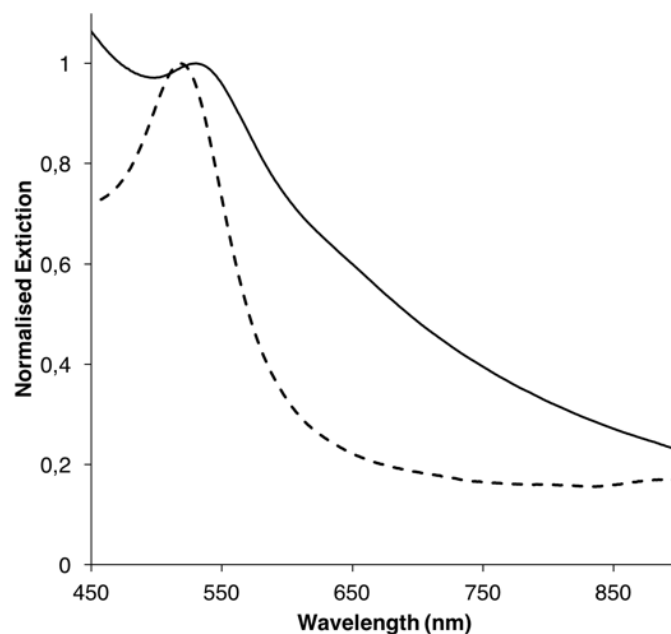


Figure 3.4 Extinction spectrum of the 20 nm gold nanoparticles building blocks used to assemble gold suprashells (dotted lines, ($\lambda_{\max} = 519$ nm)), and G1 suprashells (continuous line).

TEM analysis of supraprashells

Next, the morphology of the supraprashells were studied under electron microscopy. The dextran around the SPION cores collapses using the high-vacuum conditions required for electron microscopy, which makes it challenging to visualize the exact morphology of the supraprashells. In Figure 3.5a the dextran-coated cores of G3 were imaged in backscatter mode in order to maximize the contrast of the polymeric matrix. In this image, the polymer-coated SPION cores appear as undefined globular objects of low electron density. The SPION cores are ~500 nm as provided by the manufacturers and have irregular shapes. In Figure 3.5b-f, 20 nm gold nanoparticles can be clearly identified around the cores in scanning transmission electron microscopy (STEM) mode due to their characteristic size and electron density. In these images the number of gold nanoparticles per SPION core increases from G1 to G5, in agreement with the assembly method depicted in the schematic diagram, Figure 3.2. Although in some cases the nanoparticles seem to be randomly aggregated due to the collapse of the polymeric matrix, anisotropic assemblies can also be clearly detected, which are further extended as more nano-building blocks are assembled onto the supraprashell. These observations agree well with the plasmonic behaviour of anisotropic assemblies of nanoparticles observed in Figure 3.3.

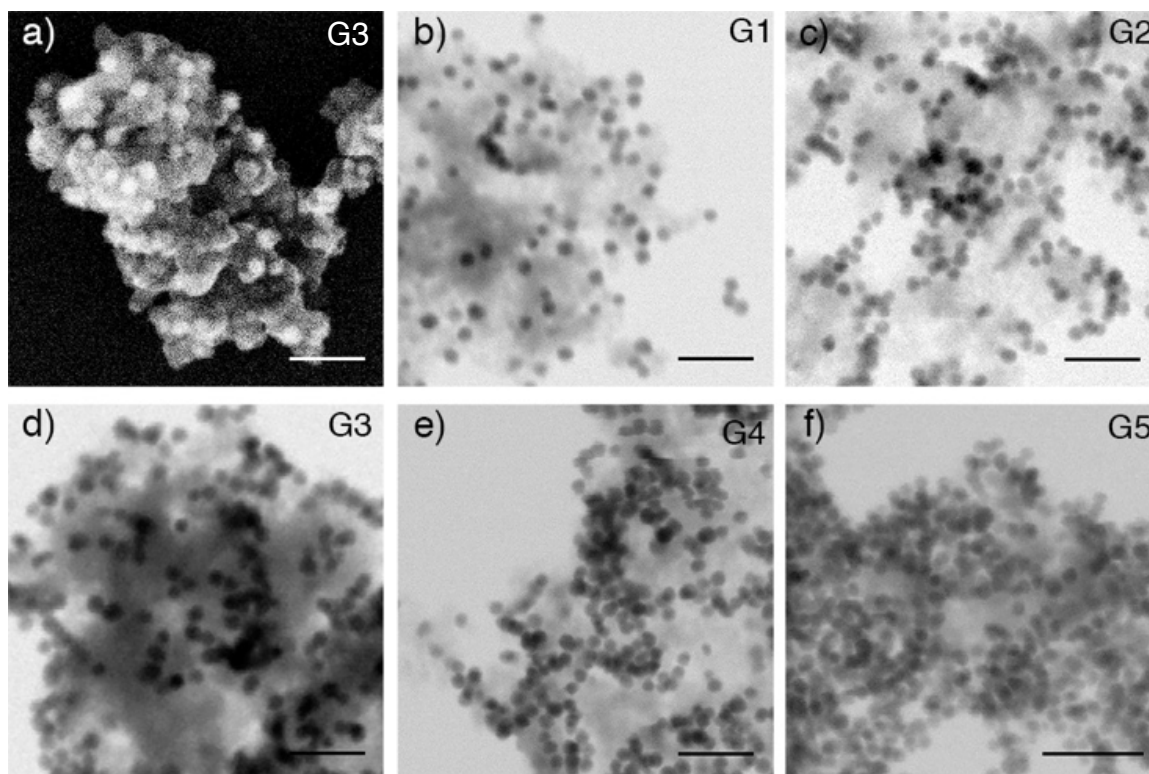


Figure 3.5. Electron microscopy images showing suprashells assembled on SPION; (a) In backscatter mode the contrast of the polymeric matrix is enhanced, which enables visualizing the overall shape of the dextran-coated SPION cores; (b), (c), (d), (e), and (f) correspond to G1, G2, G3, G4 and G5 in STEM mode, respectively. In these images the electron-dense gold nanoparticles can be easily identified by their characteristic size (20 nm). Scale bar = 100 nm.

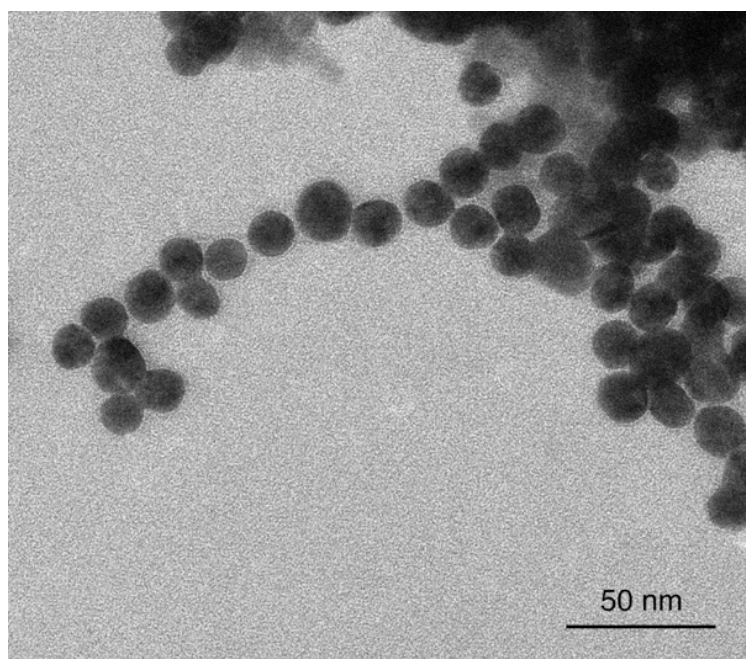


Figure 3.6 Representative TEM image of anisotropic assemblies of nanoparticles in gold suprashells (G3). The inter-particle distance was calculated as the average distance between 150 nanoparticle pairs

SERS experiments with suprashells

The observation of coupled plasmon modes in gold suprashells in Figure 3.4 demonstrates that the nanoparticle building blocks are assembled in close contact. The average inter-particle distance is 1.3 ± 0.3 nm (Figure 3.6). The presence of plasmonic hot spots resonant at multiple wavelengths would be advantageous as a flexible platform capable of enhancing the Raman signal of molecules across a wide range of incident laser wavelengths, even when molecules' absorbance wavelength does not match the LSPR of the nanoparticles. To demonstrate this concept G1, G3 and G5 gold suprashells were modified with 2-naphthalenethiol. This was chosen as the Raman reporter as it is a non-resonant dye therefore the increase in SERS signal will not be affected from the selected laser wavelength. Bulk SERS spectra were recorded upon excitation at 638 nm and 785 nm independently. All colloidal dispersions contained the same suprashell concentration ($1.4 \cdot 10^{10}$ particles \cdot mL $^{-1}$, calculated by nanoparticle tracking analysis). The resulting spectra were normalized to account for any instrumental variations in the signal intensity (see experimental section). In Figure 3.7, G1, G3 and G5 yield well-defined SERS spectra of the non-resonant dye irrespective of the excitation wavelength.¹⁴⁸ G3 and G5 samples always yield more intense bulk SERS

signals than G1 regardless of the excitation wavelength. This is attributed to the lower concentration of nanoparticles and hot spots around G1 cores compared to G3 and G5. The normalized SERS intensities obtained with G3 and G5 are very similar at the two wavelengths assayed even though the concentration of gold per suprashell is higher for G5 than for G3. This observation agrees with previous studies reporting that the enhancement factor in nanoparticle assemblies is not directly correlated to the number of constituent nanoparticle building blocks.¹⁴⁹ It also follows the general trend observed in theoretical studies reporting that the electric field in linear nanoparticle assemblies of different lengths is mainly focused in the centre of the assemblies, and therefore that longer assemblies do not necessarily yield significantly higher SERS enhancements.¹⁵⁰ Furthermore, the suprashells modified with 2-naphthalenethiol can be detected at the single-suprashell level in a SERS maps (Figure 3.8). This demonstrates that suprashells yield detectable Raman signals even when the absorbance wavelength of the molecule under study does not match their LSPR.

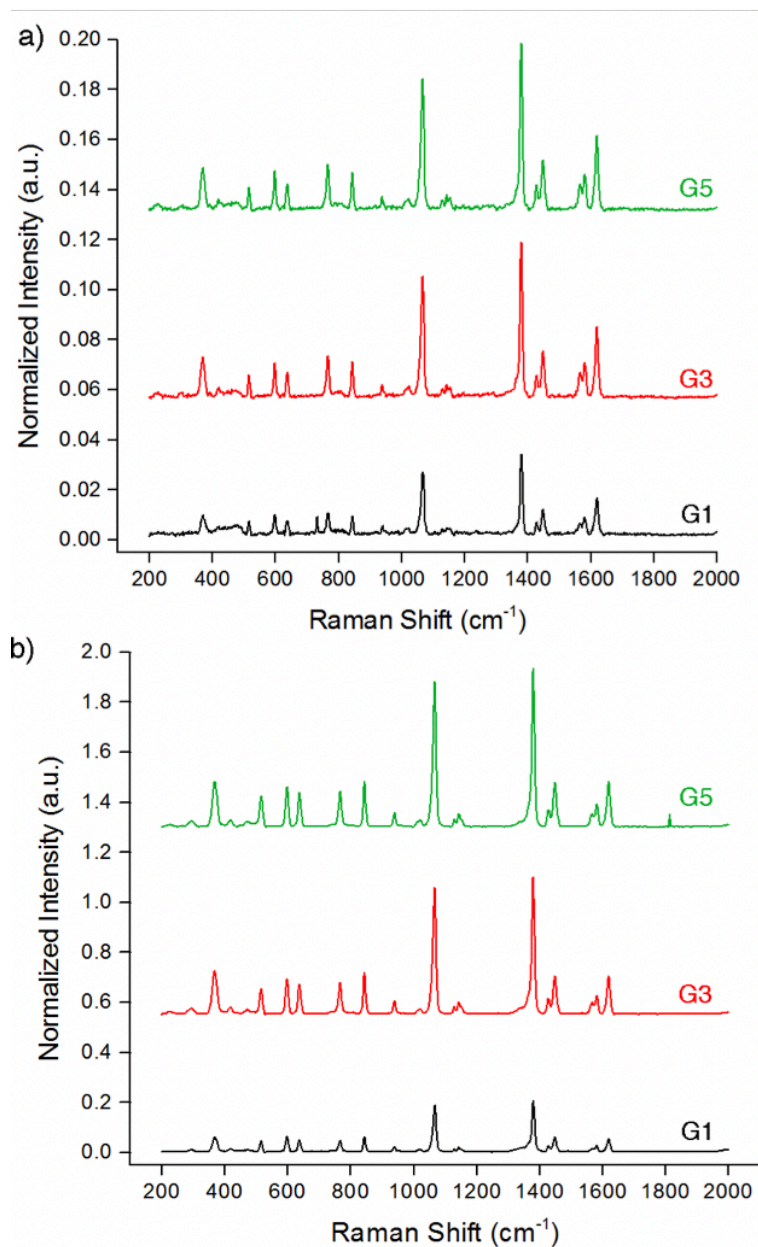


Figure 3.7 Bulk SERS spectra of G1 (black), G3 (red) and G5 (green) gold suprashells coated with 2-naphthalenethiol at excitation wavelengths of (a) 638 nm and (b) 785 nm. The concentration of suprashells in all samples was $1.4 \cdot 10^{10}$ particles $\cdot\text{mL}^{-1}$. Spectra were normalized with respect to an ethanol spectrum taken in identical conditions.

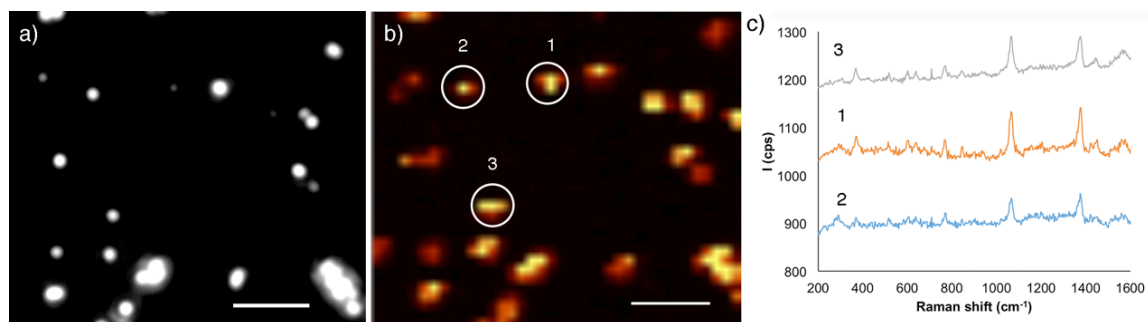


Figure 3.8 SERS mapping of suprashells modified with 2-naphthalenethiol; a), b) Correlated dark-field microscopy (DFM) image and SERS map of G5 suprashells adsorbed onto a glass slide; c) Representative SERS spectra of single suprashells (highlighted with a circle in (b)). SERS images were generated from analysis of the peak intensity at $\sim 1064\text{ cm}^{-1}$ with respect to the background signal with the brightest points corresponding to intensities >300 counts/s (cps). Scale bars= $5\text{ }\mu\text{m}$.

In summary, these results demonstrate that the SERS response of gold suprashells is dominated by the presence of hot spots.¹⁵¹ The suprashells generate well-defined SERS spectra of non-resonant molecules when excited at different wavelengths, even when measured at the single-suprashell level. These features make gold suprashells excellent candidates for multiplex analyses using several Raman reporters absorbing light at different wavelengths and attached to the same suprashell.⁸¹

Photothermal experiments

Next the generation of plasmonic heat by gold suprashells were compared. G1, G3 and G5 suprashells were excited with two continuous wave (CW) lasers emitting light at either 514 or 785 nm. At the green excitation light, absorption is mainly related to the LSPR of the nanoparticle building blocks, whereas the coupled plasmon resonances absorb NIR light. The incident power was 27 mW for both lasers and focused into the samples, this laser power was used so that the results are comparable. The concentration of gold, calculated by inductively coupled plasma mass spectrometry (ICP-MS), was $10\text{ }\mu\text{M}$ in all samples. The samples were irradiated for a short period of time to measure variations in the photothermal properties of the suprashells in the initial stages when the temperature of the solution changes linearly with time (Figure 3.9). The samples were also irradiated for a short time to minimize the variables due to evaporation.

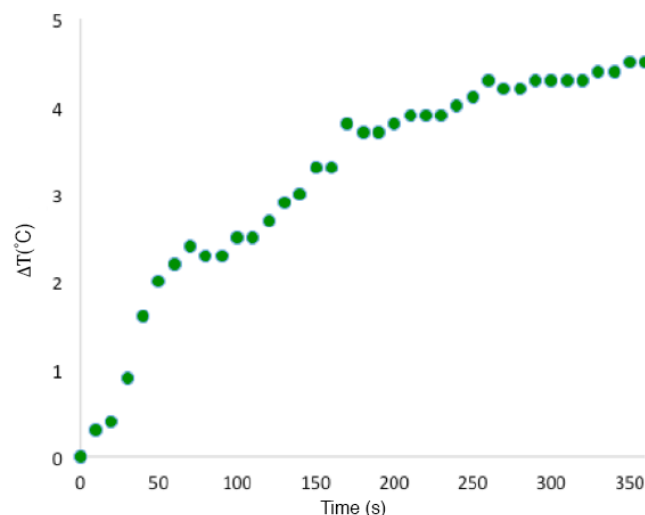


Figure 3.9 Increase in temperature with time when exciting the 20 μL of G5 gold suprashells with a 514 nm CW laser (27 mW) for 1 min.

Figure 3.10 shows that, after irradiating the samples with the 514 nm laser for 1 min, the temperature increases more in the G3 and G5 suprashell dispersions than in G1. This means that G3 and G5 are more efficient nanoheaters compared to G1. The same trend was observed when exciting the nanoparticles with the 785 nm laser. It has been proposed that heat generation by plasmonic nanoparticles is directly proportional to the square of the electric field inside the metal.¹³² Electric fields are intensified at hot spots.¹²⁹ Therefore it is possible that the presence of a larger number of hot spots in G3 and G5 is the key factor for generating higher temperatures with these nanoheaters. Furthermore, the increase in temperature observed when exciting the suprashells with the NIR laser was ca. 3 times higher than when using the green laser using the same laser power of 27 mW. These experiments also suggest that the hot spots are the main contributors to heat generation. However, it should be noted that other factors such as heat diffusion and heat distribution along the nanoparticle assemblies may also influence the temperature of the suprashell dispersion.^{132,152,153} In Figure 3.10b the 785 nm laser power was increased to 235 mW and 20 μL of each sample was also irradiated for 1 min. Under these conditions, higher increases in temperature were registered for all suprashells, which indicates that heat generation is also power-dependent. Figure 3.11 shows the specific change in temperature for G5. The temperature reaches a maximum and seems to decrease slightly, this could be due to evaporation or possible degradation of the G5 sample.

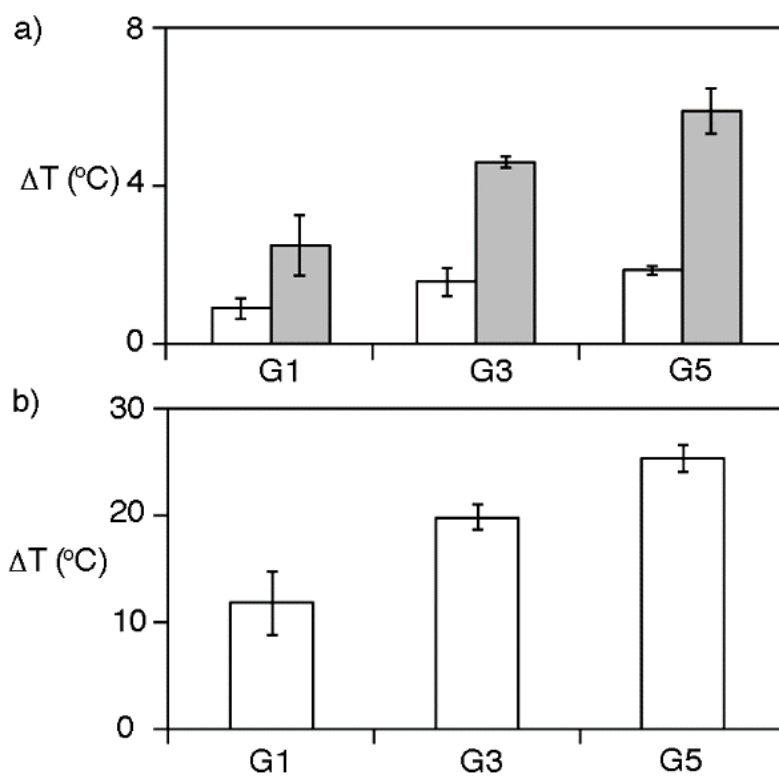


Figure 3.10 Increase in temperature measured in suprashell dispersions after irradiating them with a) a CW green laser (27 mW at the point of incidence) (white bars) or a CW NIR laser (27 mW at the point of incidence) (grey bars); b) a CW NIR laser (235 mW at the point of incidence). The concentration of gold in all experiments was 10 μM and 20 μL of each sample was used. Error bars are the standard deviation ($n = 3$).

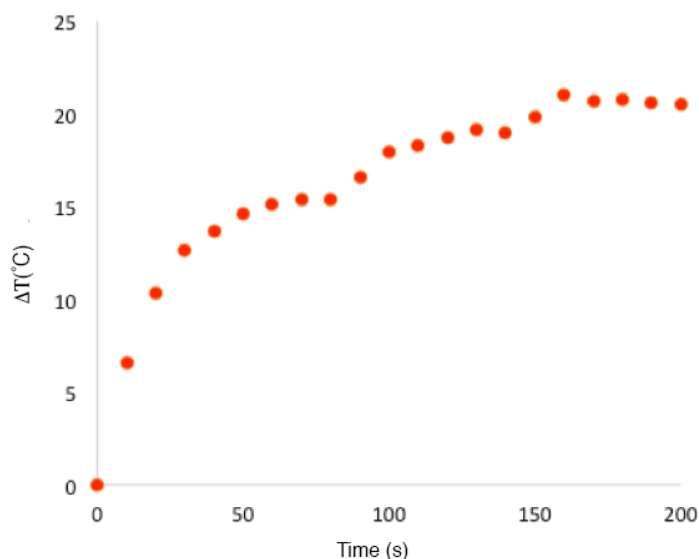


Figure 3.11 Increase in temperature with time when exciting G5 gold suprashells with a 785 nm CW laser (235 mW).

Assuming the energy absorbed from the particles is transferred into the water 100%, the energy absorbed from the laser to the suprashells can be calculated using specific heat capacity equation. The energy absorbed from the laser increases with each additional layer. G1 at 515 nm absorbed 8.37×10^{-8} kJ while G3 and G5 absorbed 2.51×10^{-7} and 3.35×10^{-7} kJ respectively. At 785 nm with a laser power of 27 mW, G1 absorbed 2.51×10^{-7} kJ, G3, 4.17×10^{-7} and G5 absorbed 5.86×10^{-7} . Not surprising as the power of the laser is increased the energy absorbed also increases accordingly.

Cell studies with G3 suprashells

After studying the plasmonic properties of the gold suprashells the potential application afforded by the magnetic core was explored. The proposed gold suprashells assembled on SPION can be easily manipulated with a magnet (Figure 3.12).

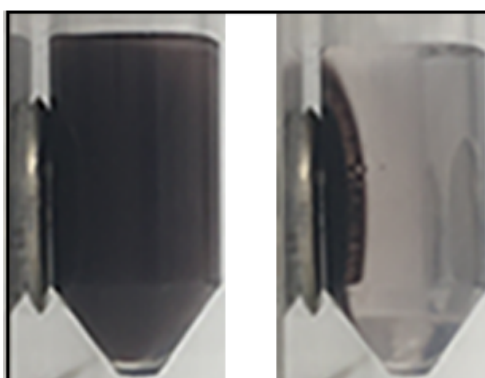


Figure 3.12 Photographs of G3 in the presence of a magnet (left: $t = 0$ s, right: $t = 90$ s).

The suprashells were internalized by prostatic small cancerous cells and cytotoxicity studies showed that only 3.3 ± 1.3 % of cell death occurred with overnight incubation (Figure 3.13a-3.13b). Cells that have internalized the plasmonic and magnetic nanoparticles can be manipulated with a magnet. For this reason, it was proposed that gold suprashells assembled on SPIONs could potentially be used as nanomedicines for eliminating circulating tumour cells (CTCs). It is well established that the release of tumour cells into peripheral blood is a cause of cancer recurrence.^{154,155} It is also a crucial factor in cancer metastasis.¹⁵⁶ In this context it would be desirable to design a therapeutic approach that could not only kill cancer cells at the primary tumour site but that

also destroy or remove cancer cells being shed into the blood stream. The gold suprashells assembled on SPION could therefore be used to this end when the CTCs bearing nanoparticles are accumulated with a magnet and killed with photothermal therapy.

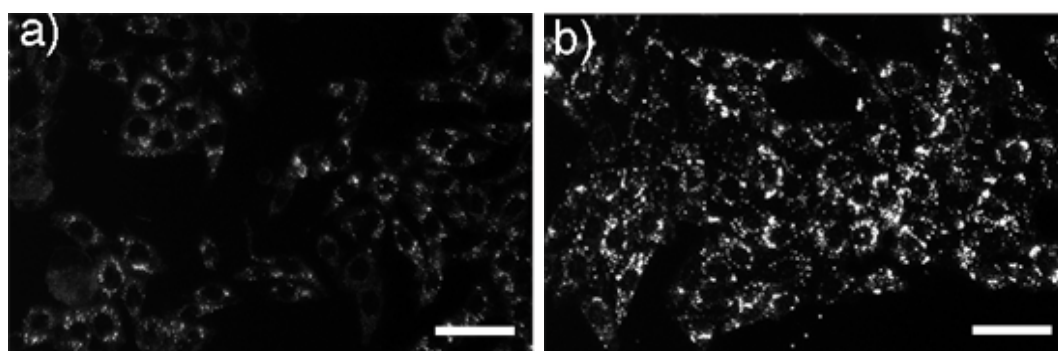


Figure 3.13 Dark-field microscopy images of prostate cancer cells; (a) without suprashells; (b) incubated with suprashells; nanoparticles are mainly found in the cell cytoplasm rather than in the nucleus;

To test whether cells bearing suprashells can be accumulated with a magnet and killed with hyperthermia, prostate cancer cells were incubated overnight with the plasmonic and magnetic nanoparticles. The cells were then trypsinized and counted. Subsequently $76 \pm 8\%$ of the cells were accumulated with an external magnet and a cell pellet was formed. The pellet was then irradiated with a focused CW NIR laser (785 nm, 235 mW at the point of incidence), which would enable greater penetration depth in real healthcare applications than the green laser. In Figure 3.14, the cells die after irradiating them with the laser for 5 min or longer, and the percentage of dead cells increase with irradiation time. This demonstrates the possibility of killing cancer cells with plasmonic heat after accumulating them with a magnet. Please note that the aim of these experiments was not killing all the cells in the pellet but rather showing that the cells can be killed with hyperthermia after magnetic accumulation. Only cells that come in contact with the laser beam are affected by the photothermal treatment. This means that the percentage of dead cells in Figure 3.14 not only depends on the laser power and

irradiation time but also on the diffusion of cells and relative volumes of the pellet and the laser irradiation, among other factors. It should also be noted that the proposed suprashells do not selectively target cancer cells per se, and therefore that they should be modified with targeting moieties in order to be useful in cancer research. For example, suprashells could become selective nanomedicines for cancer research when modified with FDA-approved anti-EpCAM antibodies, which recognize CTCs.^{44,157}

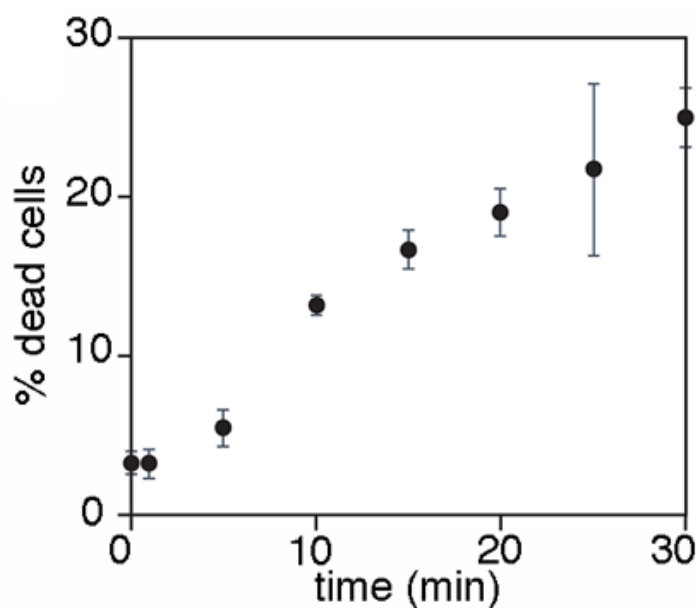


Figure 3.14 Percentage of dead cells after irradiating a sample with a CW laser emitting light at 785 nm (75 mW at the point of incidence). The cells were incubated with magnetic and plasmonic suprashells and concentrated with a magnet prior to irradiation.

3.5 Conclusion and Further Work

In conclusion, a new type of self-assembled nanostructure called gold suprashells has been reported. Suprashells are multiple extinctions at different wavelengths in the visible and NIR spectral range. This makes them versatile materials for applications that require exciting plasmonic nanoparticles over a wide range of wavelengths. Furthermore, they enable the Raman detection of molecules with single suprashell sensitivity. Another advantage of gold suprashells is that there is no need to modify the metal surface with protecting layers in order to prevent their aggregation in buffered solutions. This, along with their ability to boost SERS signals of molecules regardless of their absorbance wavelength, makes suprashells good candidates for identifying molecules by their Raman fingerprint.¹⁵⁸ The presence of hot spots also enhances the generation of heat by the gold suprashells. The generation of plasmonic heat can be used to kill cancer cells accumulated with a magnet after they have internalized the nanoparticles. This paves the way for the utilization of the proposed plasmonic and magnetic nanoparticles as therapeutic agents that enable ablating tumours and destroying circulating tumour cells with the same strategy. This is just one example of the many potential applications of the proposed magnetic and plasmonic nanoparticles. They could also be used in multimodal bioimaging strategies combining MRI and SERS,¹⁵⁹ in synergistic photothermal and magnetothermal therapies,¹⁶⁰ or in cell sorting platforms combining magnetic manipulation and SERS detection.¹⁶¹

For further work, it would be advantageous to functionalize the suprashells with a targeting moiety to further test the selectivity of the system and to repeat the experiment with a mixture cells which include the target. The photothermal experimental set up could also be improved to include a closed vial system and the data to be logged via a thermocouple data logger for increased precision. Further work can also be carried out on the multiplex functionalities of the suprashells. Raman reporters of different wavelengths could be functionalized onto the suprashell at each level and a multiplex analysis could then be carried out.

4 Self-assembled structures of the Fmoc protected amino acids and their potential use as templates for gold nanoparticle assembly.

4.1 Abstract

The aim of this chapter is to create a library of simple molecular templates for nanoparticle assembly. Templated self-assembly is a very useful tool for self-assembling gold nanoparticles. It has already been shown that this can be achieved through biomolecules such as DNA and proteins however, it would be advantageous to create a range of templates from simple biomolecules such as fluorenyl-9-methoxycarbonyl (Fmoc)- protected amino acids. Fmoc is a commonly used protecting group for amino acids, however, it has also been shown to promote self-assembly through π -stacking of its aromatic groups. It is therefore proposed that the Fmoc amino acids will self-assemble into various structures such as ribbons, spheres and fibres due to their inherent side chain characteristics. These structures are further used as soft templates for pegylated (PEG) gold nanoparticle assembly. It is hoped that the vast range of soft templates created from the amino acids will act as a platform for a range of nanoparticle superstructures such as 1D, 2D and 3D assemblies.

4.2 Introduction

Amino acid self-assembly

The self-assembly of peptides and amino acids has been studied extensively due to their inherent chemical diversity and ability to form soft nanomaterials with an array of morphologies, which have further use in a range of applications. Their biocompatibility and low synthetic cost also make them highly attractive as building blocks in bio nanotechnology applications. One way to increase the functionality and tunability of the soft matter structures is to conjugate them with an additional functional moiety. The most utilised functional group is the fluorenyl-9-methoxycarbonyl (Fmoc) group,¹⁶² this is commonly used as a protecting group in peptide synthesis (Figure 4.1). The Fmoc moiety acts as an additional driving force for self-assembly. It is intrinsically hydrophobic and capable of promoting hydrogen bonding and the aromatic fluorenyl ring promotes π - π stacking. These properties further enhance the self-assembling capabilities of the peptide enable unique arrangements in supramolecular morphologies. Furthermore, Fmoc protected amino acids offer a facile and low-cost route into supramolecular architecture as the natural chemical diversity of the amino acid side chain will influence the self-assembly process and contribute to the formation of soft templates with a plethora of sizes and dimensions (Figure 4.2).

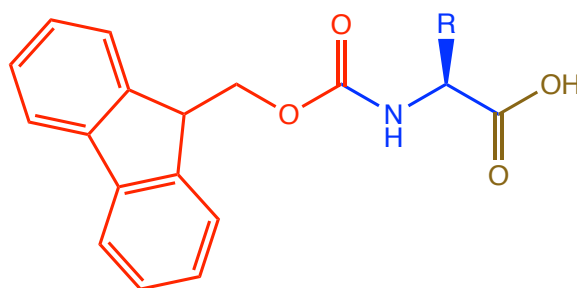


Figure 4.1 The generic structure of a Fmoc protected amino acid; red: Fmoc moiety, blue: amino acid R group; brown: C terminus.

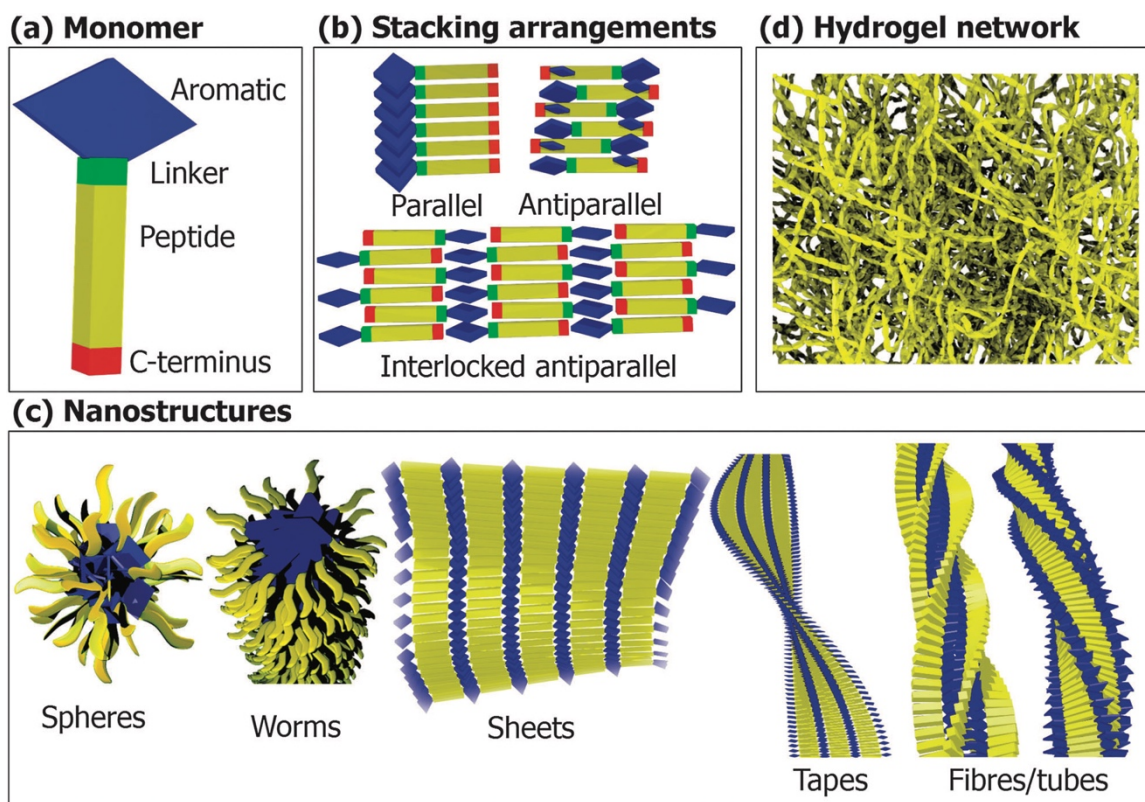


Figure 4.2 Schematic diagram representing the various supramolecular structures that can be achieved by an aromatic amphiphile. Reproduced from Ref 160

Amino acids

There are 20 gene-coded amino acids, all of which are chiral except for glycine. Naturally they are found most commonly in the L form. The amino acids have identical backbones except for proline, which is an imino acid, and are distinguishable by the R-group side chain that gives them their unique character (Figure 4.1). The side chain dictates the final shape of the structure. The amino acids can be split into different classes due to the interactions that arise from the functional group of each side chain. These include the hydrophobic, aromatic, hydrophilic, charged amino acids which are further split into the positively charged and the negatively charged and the 'special' case amino acids (Figure 4.3).

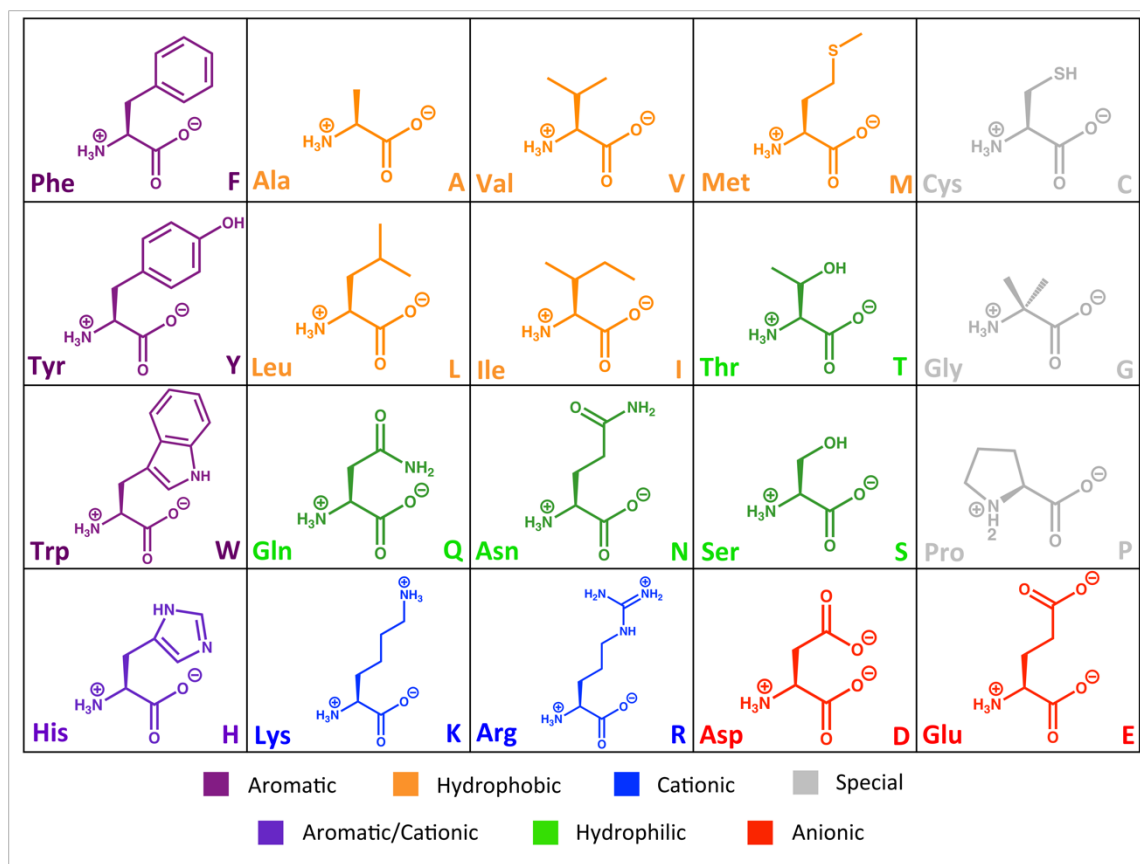


Figure 4.3 The 20 gene-coded amino acids categorised into their collective classification according to their side chain commonality. Their one letter coding is in brackets.

The hydrophobic amino acids include alanine (A), valine (V), leucine (L), isoleucine (I) and methionine (M). Their side chains are primarily aliphatic, and its hydrophobicity leads to the phenomenon known as the hydrophobic effect whereby the solvent rearranges itself around the nonpolar solute which is entropy driven. The hydrophobic effect is most commonly seen in water.

The aromatic amino acids are phenylalanine (F), tryptophan (W) and tyrosine (Y). These are also hydrophobic and each of the side chains contains a delocalized π system capable of stacking. Y contains an electron withdrawing hydroxyl group on the para position of the aromatic ring and W contains an indole functional group which is capable of oxidation.

The hydrophilic amino acids are serine (S), threonine (T), asparagine (N) and glutamine (Q). These are polar and uncharged. S and T are similar in that they both contain a terminal hydroxyl group at the end of their R-group with T containing

an extra methyl. N and Q contain carboxamide groups that can form hydrogen bonds on both the carbonyl and the NH₂ moieties.

The charged amino acids can split into negative and positive residues. The negative residues are glutamic acid (E) and aspartic acid (D), which contain anionic side chains featuring a terminal carboxylic acid causing the pKa's of glutamic acid, and aspartic acid to be 4.2 and 3.9 respectively.¹⁶³ This means that at a neutral pH, the side chains are deprotonated, and electrostatic interactions can occur. The positive residues include lysine (K) and arginine (R) which both have a terminal amine in their R-group. The pKa's of lysine and arginine are 10.5 and 12.3 therefore at pH 7, their cationic side chains are protonated. It is important to highlight that the pH of the solvent plays a significant role in the self-assembling interactions as can be observed with histidine.

Histidine (H) is both charged and aromatic, containing a terminal imidazole group in its side chain. The imidazole group is capable of π bonding and the charge on the side chain is highly dependent on the pH of the solvent. With a pKa of 6.6, under biological conditions the imidazole ring is protonated. However, the second nitrogen can become protonated if the pH of the solution dips below 6 affecting the stacking potential of the amino acid.

The special case amino acids are named as such because they do not fit into any other category and have unique properties. Proline (P) is the only amino acid that has its α -amine incorporated into its side chain. When incorporated into a peptide bond, this creates rigidity as it is unable to donate or accept hydrogen bonds in an α -helix or β -sheet. Cysteine (C) has a terminal thiol group which can undergo oxidation to form disulphide bridges. Glycine (G) is the most simplistic amino acid of the 20 and is the only one that is not chiral because the R-group of glycine consists of a single hydrogen bond.

Nanoparticle self-assembly

Assembling materials from nanoparticles is a central issue in nanofabrication and materials chemistry because the resulting superstructures could have different physical properties due to the arrangement of nano-building blocks in their structure.¹⁶⁴ Among the different approaches for self-assembling nanoparticles into organised superstructures,^{14,50,56,165} templated methods stand out because they produce superstructures that have well defined dimensions and shapes such as nanotubes, spheres or nanofibers. For example, DNA origami scaffolds can be used to guide the assembly of nanoparticle superstructures with different sizes and spatial organisation using programmed DNA-DNA interactions.^{23,26,108,166–168} However, DNA origami templates are mainly used to assemble 1D¹⁶⁹ or 2D nanoparticle superstructures.^{28,49,170} To form 3D superstructures with exquisite internal order, nanoparticles are usually modified with carefully designed oligonucleotides that guide the assembly of supracrystals.^{59,170} Yet, 1D or 2D supracrystals cannot be obtained with the same approach. Herein, it would be desirable to find a method for obtaining a vast array of different nanoparticle superstructures using widely available building blocks such as amino acids. Such a method would reveal a new family of nanoparticle-based nanoobjects with an array of controlled dimensions and orders.

In this chapter it will be shown that when the Fmoc-protected amino acids are incubated with polymer-coated (PEGylated) nanoparticles some self-assemble and interact with each other to yield soft templates covered with nanoparticle superstructures. These superstructures show a wide variety of orders, from 1D supraparticles to 2D networks and hexagonally packed 3D clusters. These occur as a result of the inherent chemical variability of the natural amino acids, that give rise to a plethora of templates. This makes the proposed method of assembling nanoparticles onto the Fmoc amino acid templates a particularly versatile approach for obtaining different types nanoparticle superstructures.

4.3 Experimental

4.3.1 Materials

All reagents and amino acids were purchased from commercial sources (Sigma Aldrich, Fisher and Alfa Aesar). Experiments were performed at room temperature (21- 25°C) unless stated otherwise in the experimental procedure.

4.3.2 Fmoc amino acid assembly

10 mM of each amino acid was weighed out and added to 1 mL of 100 mM, pH 8 phosphate buffer. Each amino acid was then sonicated for 10 s and heated for 5 minutes at 35°C. The solutions were then left to cool and analysis was taken after 6 days to allow for complete self-assembly. For the concentration studies, 2 mL of 10 mM of each amino acid was prepared. This was then added to a slightly heated solution of 100 mM pH 8 phosphate buffer and vortexed to achieve final concentration of 0.1 mM, 0.5 mM, 1 mM, 5 mM and 10 mM in 1 mL of solution.

4.3.3 PEGylated gold nanoparticles

Citrate capped gold nanoparticles were first obtained by adding 61.9 mg of sodium citrate dissolved in 1 mL of MilliQ water to a boiling solution of 500 mL of MilliQ water containing 25.6 mg of gold (III) chloride hydrate. This yielded 20 nm citrate capped gold nanoparticles with a λ_{\max} of 518 nm and a zeta potential of -37.7 mV. After the solution cooled, 16 μM of carboxy-PEG-thiol (CT-PEG₁₂) was added to the nanoparticles and left for 3 h. The nanoparticles were then centrifuged for 30 min at 6037 g to remove any excess PEG and the λ_{\max} shifted to 521 nm and the zeta potential changed to -21.37 mV.

4.3.4 PEGylated gold nanoparticles with the Fmoc-monomers

10 mM of each amino acid was weighed out into a glass vial and 6 μL of PEGylated gold nanoparticles was then added to each vial. 994 μL of 100 mM pH 8 phosphate buffer was then added to the vial and each amino acid was prepared as previously stated. The prepared PEGylated gold nanoparticles were first centrifuged and

concentrated so that the addition of nanoparticles gave a final concentration of 1.32 nM gold nanoparticles. This was to ensure the nanoparticles did not drastically change the pH of the phosphate buffer.

4.3.5 Fourier Transform Infra-red Spectroscopy (FTIR)

FTIR spectra were acquired using a Perkin Elmer spectrum 2 spectrometer in transmission mode. The spectrometer had a resolution of 4 cm^{-1} and spectra was obtained by averaging 16 measurements for each sample.

Each sample was acquired 3 times to account for any variations within the spectrometer and triplicates were performed for each amino acid. Standard FTIR cuvettes (Harrick Scientific) were used and each sample was sandwiched between 2 CaF_2 discs (Crystran Ltd) and a 50 μM PTFE spacer. For free-flowing samples 100 μL of the sample was pipetted directly onto the disc while gel samples were placed onto the disc using a micro spatula. 100 mM pH 8 phosphate buffer was made up in D_2O buffer and used as the solvent, so the water peaks do not overlap the amide region of the spectra. Spectra was baseline corrected with MATLAB.

4.3.6 Circular Dichroism (CD)

CD measurements were performed using a Jasco J-810 spectropolarimeter with a step resolution of 0.5 nm, response of 0.5 s, 1 nm bandwidth and a scanning speed of 100 nm/min. Cylinder cuvettes with a pathlength of 0.01, 0.02 and 0.05 cm or a demountable plate cuvette of 0.002cm was used to obtain spectra depending on the HT voltage response of the sample. If the HT voltage reached above 600 then the detector showed saturation and a cuvette with a smaller pathlength was used. Each sample was then numerically corrected to allow for direct comparisons between concentrations. 100 μL of each sample was added to the cylinder cuvette or 50 μL of sample was added to the demountable cuvette. Measurement was taken from 190 nm to 320 nm.

4.3.7 UV-vis spectroscopy

UV-vis spectra were recorded using a Jasco V-660 spectrophotometer. Samples were prepared in a PMMA UV grade cuvette with a pathlength of 1 cm. Spectra was obtained from 400 – 900 nm using a bandwidth of 1 nm with a medium response and a scan speed of 200 nm/min

4.3.8 Atomic Force Microscopy (AFM)

AFM images were obtained using a Bruker Multimode 8 AFM. The operation was set to carry out a fast scan on the tapping mode. Samples were prepared the 24 h before collection. Mica was cleaned with ethanol and left to dry. 10 μ L of each sample was then pipetted onto the mica slide and left in a covered petri dish to dry overnight.

4.3.9 Transmission Electron Microscopy (TEM)

TEM images were captured using a FEI Tecnai T20 transmission electron microscope operating at 200kV. Carbon-coated copper grids (200 mesh) were glow discharged in air for 30 s. 5 μ L of sample was deposited on the grid for 30 s then blotted with filter paper to remove excess. For gel samples, the grid was touched onto the gels for 30 s then also blotted down using filter paper. To view the amino acids on the TEM, negative stain (10 μ L, 1 % aq. Methylamine vanadate obtained from Nanovan, Nanoprobes) was applied to the grids the excess was removed by filter paper. Each sample was left to dry in a closed environment prior to imaging.

4.3.10 Scanning Electron Microscopy (SEM)

SEM imaging was performed using a FEI Quanta 250 FEG-ESEM in scanning electron transmission mode. 1-2 μL of the sample was added to a coated copper grid (200 mesh) and the sample was allowed to dry in a closed environment prior to imaging.

4.3.11 Coarse-grained simulations

These simulations were carried out as a collaborative work with Prof. Tell Tuttle. Simulations were done using Gromacs 5^{171,172}. A time step of 10 fs was used to integrate equation of motion. The simulations were run in a cubic box with periodic boundary condition in XYZ direction. The neighbourhood list was updated by Verlet scheme every 20 steps. The pressure was maintained at 1 atm using a Parrinello-Rahman barostat ($\tau_p=12.0 \text{ ps}^{-1}$) and the temperature at 300 K by a v-rescale thermostat ($\tau_T=1.0 \text{ ps}^{-1}$). For simulation of self-assembly, starting configurations were obtained by randomly distributing 300 molecules in a cubic box of size 13nm x 13 nm x 13 nm, and solvating by water (concentration $\sim 0.225 \text{ M}$). Systems were simulated for 1 μs . The coarse-grained representations of amino acids present in the literature was used.¹⁷³

4.3.12 Raman experiments

Raman experiments were carried out using a Renishaw InVia upright microscope equipped with a 532 nm CW laser. Spectra were obtained using a 50x objective lens (Olympus MPlan, NA=0.9) with a laser power of 40 mW, an acquisition time of 3 s and a 1200 lines/mm grating. 20 μL of each amino acid was added to the CaF_2 disc and spectra was obtained by averaging 5 spectra acquired from each sample. Careful consideration was taken to not let the sample dry in order to not obscure or influence the Raman/SERS response.

4.4 Systematic study of Fmoc-amino acids

Self-assembly is realised through non-covalent interactions and the Fmoc moiety is known to promote this due to its hydrophobicity and its ability to π stack. There is high interest in Fmoc-protected amino acids whose self-assembled-structures lead to the formation of gels. However, the full spectrum of structures formed from these Fmoc-monomers is has not yet been characterised.^{6,174} It is proposed that each Fmoc protected amino acid will form its own unique structure as a result of the chemical diversity of their respective side chains and the N-terminal Fmoc moiety will help facilitate self-assembly. Each structure is categorized into its respective amino acid family

- Aromatic
- Hydrophobic
- Hydrophilic
- Charged
- 'Other'

The amino acids from this point forward will be referred to by their single letter coding for simplicity. Coarse grained simulations (in collaboration with Prof. Tell Tuttle) of the Fmoc amino acids were carried out with a neutral C-terminus. It should be noted that by using coarse grained analysis there is loss of atomistic detail, therefore some structures obtained are not always a direct representation of reality. Amino acid concentration also plays a vital role in triggering the self-assembly of supramolecular architectures,¹⁷⁵ therefore initial concentration studies were carried out using chiral dichroism (CD) and Fourier-transform infrared spectroscopy (FTIR). D₂O is used in lieu of water in FTIR analysis due to the H₂O peaks overlapping with the amide region of interest at 1550 cm⁻¹ to 1750 cm⁻¹. Further analysis using atomic force microscopy (AFM) and transmission electron microscopy (TEM) was used to obtain images of the fully formed structures. Furthermore, this revealed the various of structures that are formed from the Fmoc amino acids which ranged from small spherical micelles to nanoplates and twisted nanofibrils. Structures were further used as potential

templates for gold nanoparticle assembly, 1.32 nM of 20 nm PEGylated gold nanoparticles were added to 10 mM Fmoc amino acids prior to self-assembly. After assembly, surface enhanced Raman spectroscopy (SERS) was utilized to evaluate the interactions within the hybrid structures. TEM analysis was also carried out on some of these structures formed. For clarity when discussing Raman experiments, the spectra of samples containing nanoparticles will be referred to as a SERS spectrum regardless of their effect on the signal and samples containing only amino acids will be referred to as a Raman spectrum.

4.5 Aromatic Amino Acids

Composition

The aromatic amino acids, F, Y and W, contain phenyl groups within their side chain that help direct monomer self-assembly. The synergistic effects of the intermolecular interactions of the Fmoc moiety and the phenyl groups facilitate the formation of nanofibrils. The presence of 1D fibrils has been reported to be a prerequisite for hydrogelation, the increase in non-covalent crosslinking between the fibres ultimately leads to a decrease in solvent flow thus a gel is formed. Fmoc-F and Fmoc Y are well known low molecular weight (LMW) gelators. Previous reports have shown that the aromatic Fmoc amino acids are able to form hydrogels through a 'pH switch' method¹⁷⁴ and Fmoc F is capable of forming a hydrogel at neutral pH 7.4 with a similar approach as to the one reported here.¹⁷⁶

The aromatic amino acids are intrinsically hydrophobic and with the addition of the Fmoc group, the hydrophobicity of the molecule subsequently increases thus the solubility of the molecule decreases. As per the experimental section, 0.1 mM, 0.5 mM, 1 mM, 5 mM and 10 mM of each amino acid was added to pH 8 phosphate buffer. To aid solubility, each sample underwent a rapid sonication (10 s) followed by 5 min of gentle heating of which the solutions went from milky to transparent (solutions heated from 22 °C to 35 °C), these were then left to cool back down to room temperature.

All the aromatic Fmoc-monomers displayed visible differences after 48 h (Figure 4.4). Out of the three amino acids, Fmoc F (10 mM) was found to gel the quickest, a visible gel started to form after 12 mins and after 16 mins gelation was complete. The cloudy gel was also self-supporting. Overnight, Fmoc W formed a weak translucent gel and with time this turned into white fibrous spheres. Fmoc Y formed a turbid suspended gel after 48 h and even after 1 week, Fmoc Y did not form a complete self-supporting gel. Previous studies have shown that Fmoc F does not gelate in deionised water therefore it is important to note that solvent choice and the presence of ions are an important factor for self-assembly to be realised. It has been suggested that the presence of multivalent anions help

facilitate hydrogen bonding between the residues.¹⁷⁷ It should also be noted that without heating the aromatic amino acids remained insoluble.

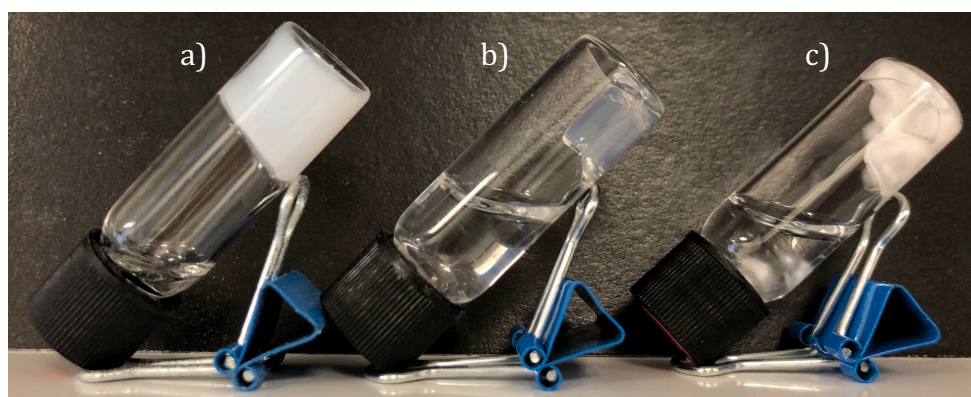


Figure 4.4 Photographs of a) Fmoc-F; b) Fmoc-Y; c) Fmoc-W; 10 mM in 100 mM pH 8 phosphate buffer after 7 days.

Supramolecular structure

Figure 4.5 shows transmission FTIR and CD analysis of a range of concentration for the aromatic Fmoc-monomers. The broad peak around 1570 cm^{-1} observed in the low amino acid concentration solution is a consequence of incomplete exchange of D_2O to H_2O .^{178,179} However as the concentration increases, sharper more defined peaks arise. The region at $1600\text{-}1700\text{ cm}^{-1}$ is customarily linked to the amide I band ($\text{C}=\text{O}$ stretching), however published data revealed that the presence of Fmoc influences the wavenumber of the amide I and the peak present at $\sim 1685\text{ cm}^{-1}$ is due to the carbamate of the Fmoc.¹⁸⁰ Moreover, H-bonding is responsible for peaks shifting to lower wavenumbers.¹⁸¹ Intense peaks observed at 1664 cm^{-1} in Fmoc F and at 1653 cm^{-1} in Fmoc Y are a result of strongly hydrogen bonded carbamate within the Fmoc. There is a doublet peak observed in the Fmoc W spectrum at 1670 cm^{-1} and 1681 cm^{-1} . This could be due to different intermolecular environments that the Fmoc carbamate is in. The small shoulder at 1701 cm^{-1} can be assigned to the carboxylic acid on the C terminus. The slight shoulder around 1615 cm^{-1} of the Fmoc Y spectra is due to the $\nu\text{C-C}$, $\delta\text{C-H}$ of the tyrosine side chain containing an electron withdrawing OH on the para position of the phenyl group.¹⁸² The non-Gaussian peak around 1600 cm^{-1} of Fmoc F is due to an overlap of the phenyl side chain and amide I band. The strong peaks observed at 1578 cm^{-1} in Fmoc Y and at 1583 cm^{-1} in Fmoc W are attributed to this as well.

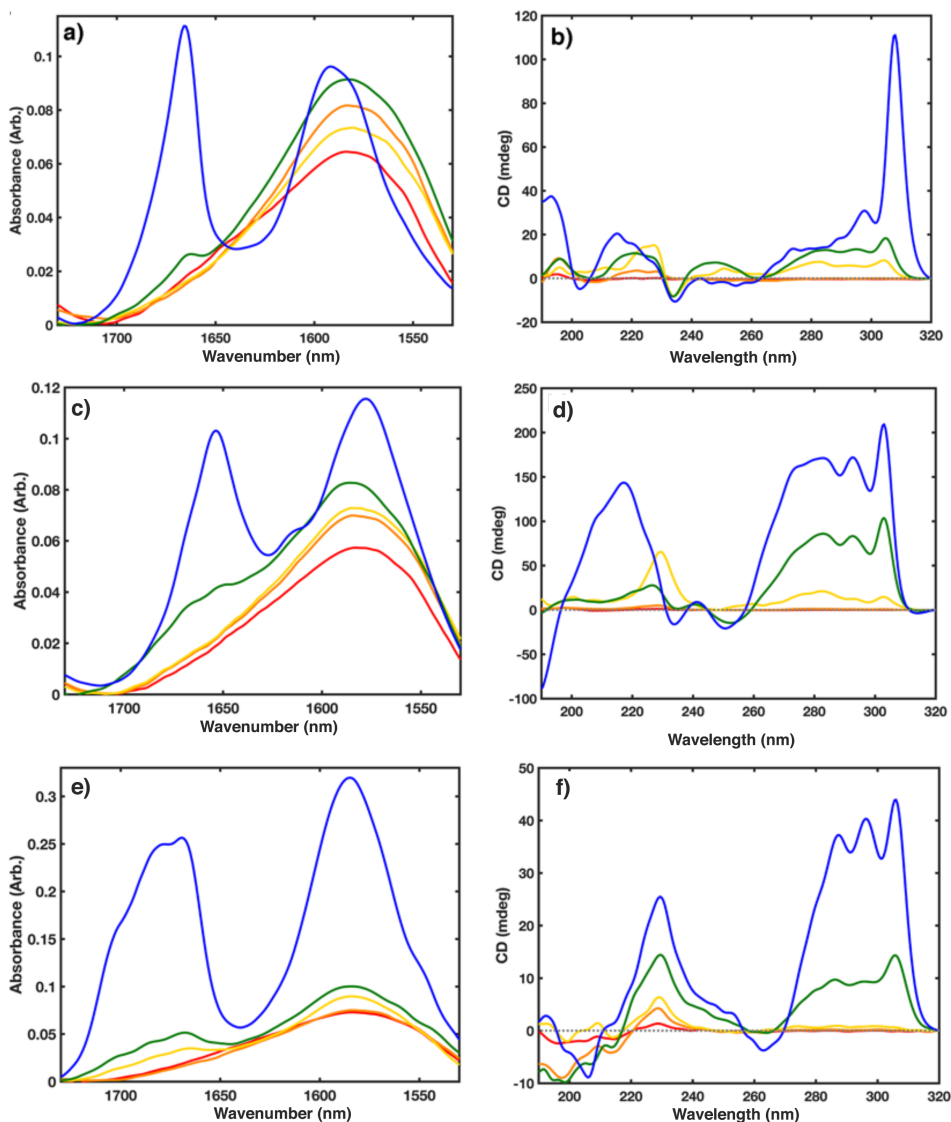


Figure 4.5 Transimission FTIR and CD spectra of Fmoc aromatic amino acids with increasing concentrations from 0.1 mM (red line), 0.5 mM (orange), 1mM (yellow line), 5 mM (green line), and 10 mM (blue line): Spectra taken after 6 days of self assembly in pH 8 phosphate buffer (D₂O (for FTIR) or H₂O (for CD): a) FTIR spectra of Fmoc F b) CD spectra of Fmoc F c) FTIR spectra of Fmoc Y d) CD spectra of Fmoc Y e) FTIR spectra of Fmoc W f) CD spectra of Fmoc W

There are spectral similarities to note in the CD spectra of all three amino acids. The fluorenyl peak at 305 nm due to the π to π^* transition of the Fmoc arises in all amino acid assemblies.¹⁸³ However, the region of 190-230 nm is where the carbonyl chromophore absorbs, which is present in both the Fmoc moiety and the amino acid.¹⁸⁴ This can be shifted depending on the hydrogen bonding on the lone pair of the oxygen. Within the Fmoc F spectrum, the 215 nm peak arises from the carbonyl chromophores of the Fmoc as an increase in the 305 nm peak also

increases the carbonyl peak. Interestingly, the 230 nm peak observed in the Fmoc W spectra is most likely due to the carbonyl chromophore of the amino acid as the peak is still visible at lower concentrations whereas the fluorenyl peak is absent. Aromatic side chains absorb in the near UV-Vis range of 230-300 nm.¹⁸⁵ The strong peaks observed in this region can be attributed to the aromatic interactions within their respective sidechains. The peaks observed are consistent with published spectra of the aromatic amino side chain.¹⁸⁴ This data corroborates with previous reports that offset face to face π interactions can occur between the neighbouring phenyl groups and Fmoc groups as well as hydrogen bonding between the neighbouring carbamates.¹⁸⁶

Coarse grained simulations and nanoscale morphology

Simulations show that the aromatic amino acids align into twisted fibres (Figure 4.6). The core of the structure consists of four Fmoc groups facing each other and are tilted slightly along the z axis and as each layer of Fmoc is slightly tilted this causes the fibres to spiral (Figure 4.7).

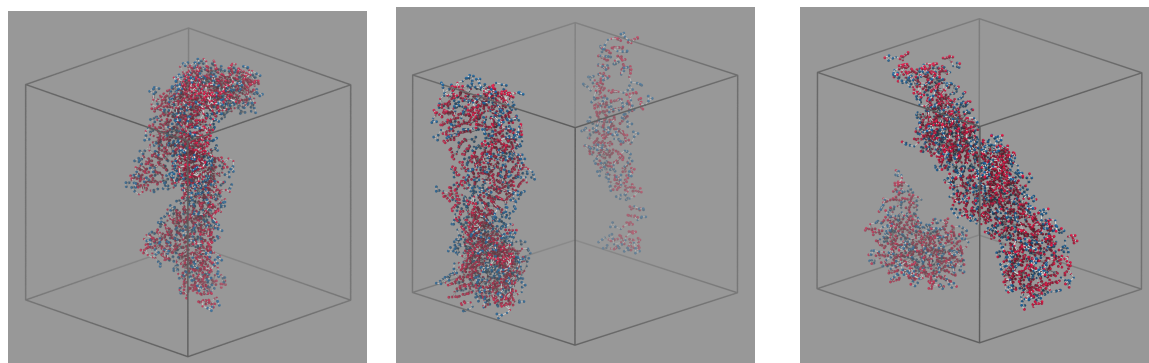


Figure 4.6 Coarse grained simulations of the fibrous structures formed from; Fmoc F (left); Fmoc Y (middle) and W (right).

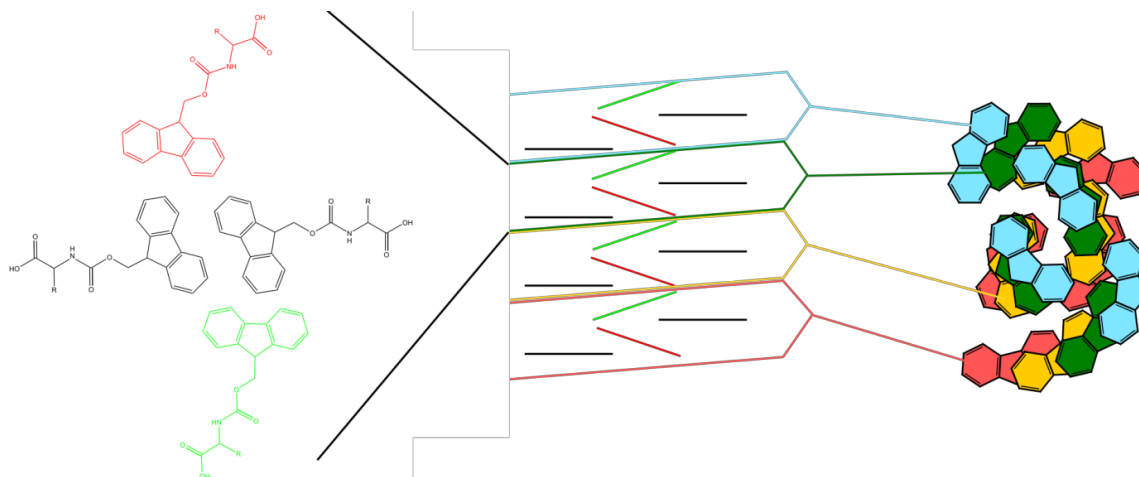


Figure 4.7 Scheme of the core of fiber structure. Left: picture from “top”, middle: picture from side, right: picture from”top” with multiple layers of basic structure forming fiber.

Investigation into the experimental nanoscale morphology was undertaken using TEM and AFM analysis (Figure 4.8). Negative stained TEM imaging showed that all aromatic Fmoc monomers form fibres (Figure 4.8a). This corroborates with published data which also demonstrated that Fmoc- protected aromatic amino acids are capable of forming fibres.^{174,176,187} AFM profiling showed that the individual height of the twisted fibres in Fmoc F were approximately 15 ± 8.62 nm. Fmoc Y forms tape like fibres that are approximately 20 nm in height and Fmoc W can be seen to self-assemble into small fibres in the TEM data. AFM showed that the thinner fibres further assemble into tight bundles of fibres of approximately 500 nm in diameter. This observation is a possible explanation for the weaker gels formed from Fmoc Y and the fibrous spheres observed in Fmoc W due to less crosslinking between the networks of fibres.

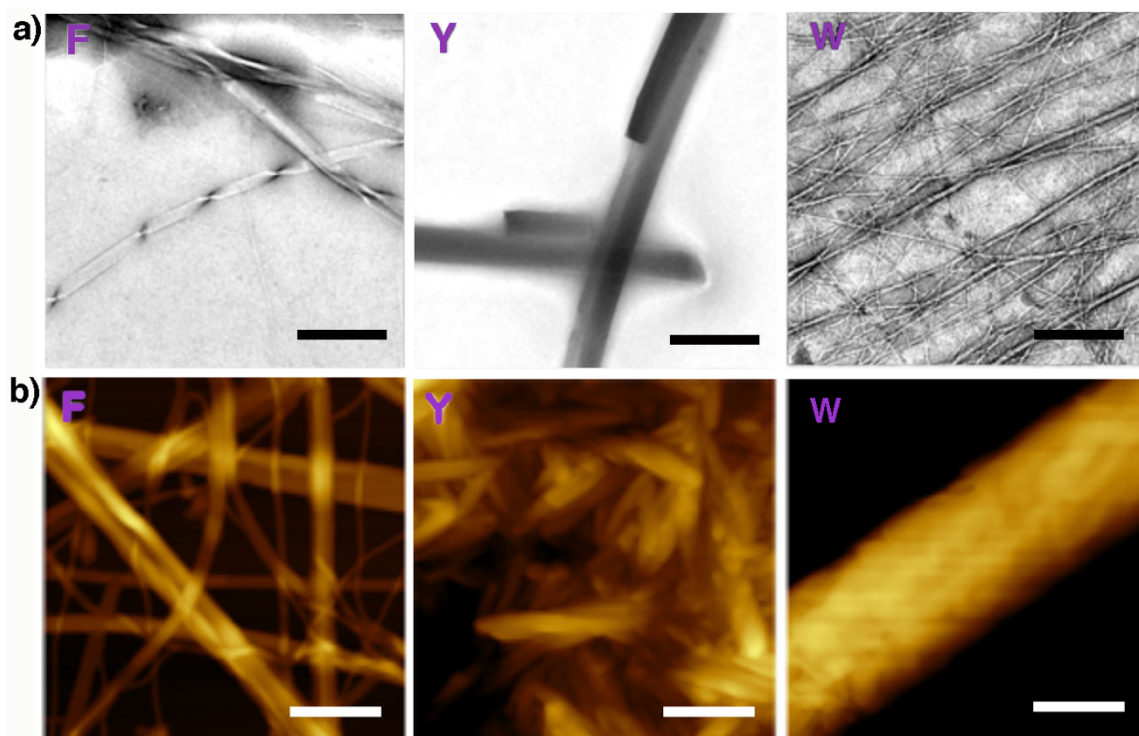


Figure 4.8 Microscopy images of; a) Negative stained TEM images from left to right of Fmoc F, Fmoc Y and Fmoc W b) AFM imaging of gels formed from (from left to right) Fmoc F, Fmoc Y and Fmoc W. All analysis was taken 6 days after self assembly and all concentrations of amino acids were 10 mM. Scale bar = 250 nm

Raman experiments with PEGylated-AuNPs

After analysis of structures formed from the Fmoc monomers, PEGylated-gold nanoparticles (PEG₁₂-AuNP) of 20 nm diameter were added to 10 mM of the Fmoc protected amino acids before self-assembly. It was hypothesized that the nanoparticles would interact with the Fmoc-monomer prior to self-assembly. Raman spectra taken after assembly showed that the samples containing nanoparticles had a weaker signal-to-noise (SNR) ratio compared to Raman spectra of the amino acid monomers (Figure 4.9). This would suggest that the nanoparticles partially inhibit fibre self-assembly. Fmoc dominates the spectra with peaks arising from well-known positions previously assigned to Fmoc at ≈ 1609 , 1480 , ≈ 1295 and ≈ 1020 cm^{-1} .^{188,189} There are distinctive differences in spectra attributed to the aromatic groups in the side chain of each amino acid. Within the Fmoc F spectra (Figure 4.9a), a sharp peak at 1001 cm^{-1} is attributed to a monosubstituted aromatic ring.¹⁹⁰ A parasubstituted ring band can be observed in the Fmoc Y spectra (Figure 4.9b) at 852 cm^{-1} and a strong signal arising from an

orthosubstituted ring can be observed at 750 cm^{-1} in Fmoc W (Figure 4.9c). Furthermore, Fmoc W contains an indole ring band at 1549 cm^{-1} .

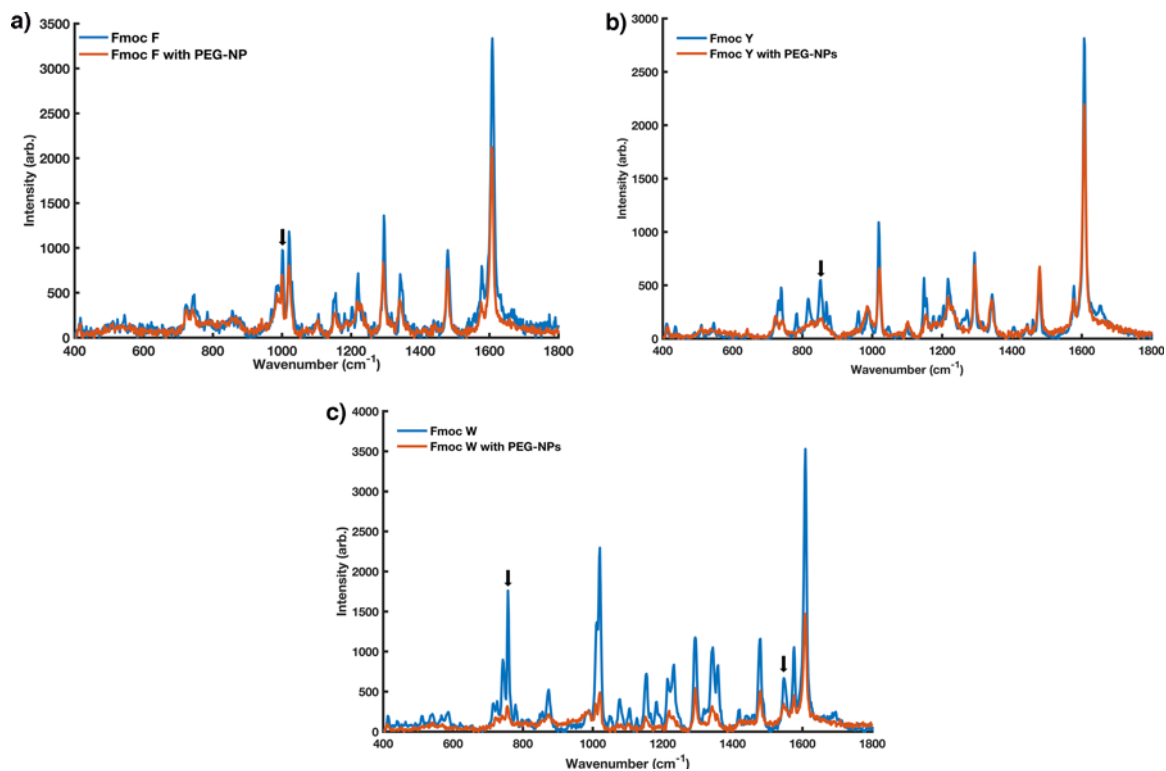


Figure 4.9 Raman spectra of 10 mM Fmoc aromatic amino acids with and without PEGylated gold nanoparticles after 1 week. a) Fmoc F gel, the monosubstituted peak is highlighted at 1001 cm^{-1} . b) Fmoc Y, the parasubstituted peak is highlighted at 852 cm^{-1} c) Fmoc W with the orthosubstituted peak highlighted at 750 cm^{-1} and the indole ring at 1349 cm^{-1} . Spectra taken with a continuous wave (CW) 532 nm laser, 40 mW laser power, acquisition time 3s. 20 μL of each sample was pipetted onto a CaF₂ plate.

TEM analysis of Fmoc F and Fmoc W (Figure 4.10) show that the nanoparticles align along the fibres. This interaction may be the reason why a dampening of signal is observed in the presence of nanoparticles as the nanoparticles contribute to blocking full fibre formation. This is especially evident in Fmoc F where the absence of nanoparticles (Figure 4.8) produces twisted fibres whereas the presence of nanoparticles yield long flat ribbons (Figure 4.10).

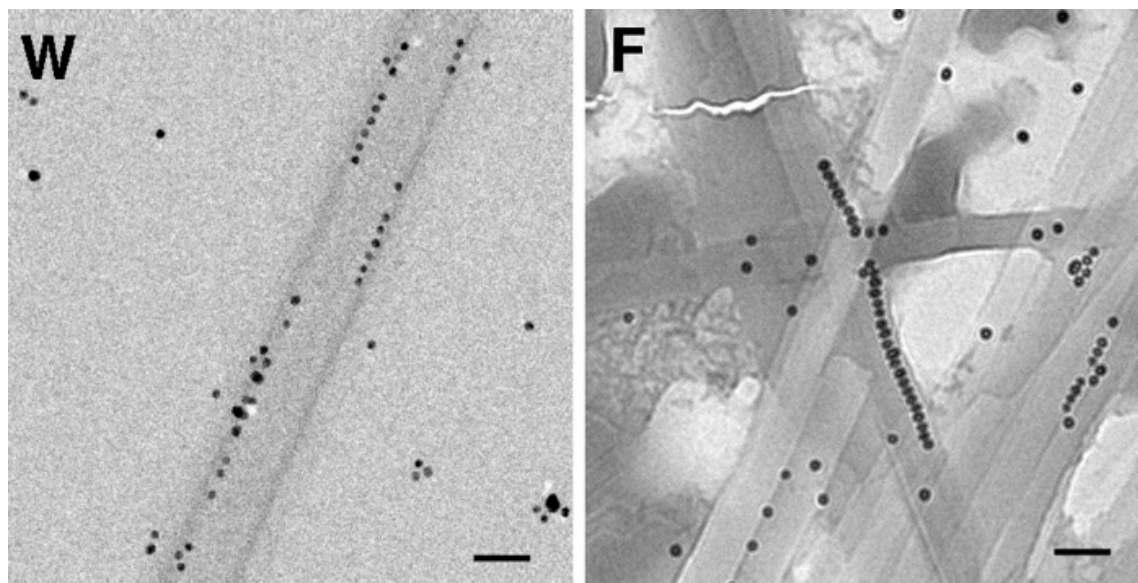


Figure 4.10 TEM imaging of 10 mM Fmoc W and Fmoc F in the presence of 1.32 nM PEGylated gold nanoparticles after 1 week of self-assembly. Scale bar is 50 nm.

Preliminary CD data of the fibres with nanoparticles is shown in Figure 4.11. There is a decrease in all CD signals in the presence of nanoparticles (red line) indicating that the nanoparticles have a deteriorating effect on the formation of chiral fibres. This correlates well with the TEM images above which suggest that the nanoparticles decrease the production of twists in the fibres. This data is preliminary and will however need to be replicated and studied further as there is a loss of resolution of the ~ 300 nm peaks in Fmoc W and a switch from right handedness (positive CD signal) to left handedness (negative CD signal) in Fmoc F compared to the previous data.

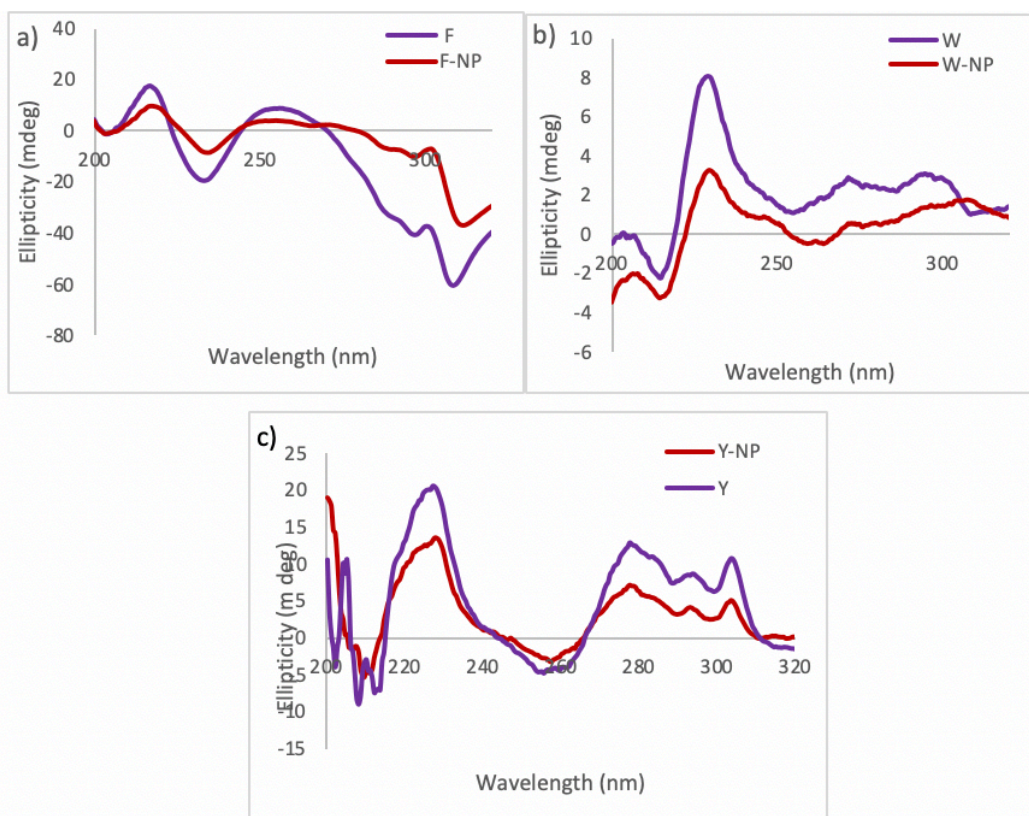


Figure 4.11 Preliminary CD data of aromatic amino acids with nanoparticles present and absent; a) Fmoc F b) Fmoc W and c) Fmoc Y

The next group of amino acids studied are the hydrophobic amino acids, Fmoc A, Fmoc V, Fmoc I, Fmoc L and Fmoc M which have not previously been studied in published literature.

4.6 Hydrophobic amino acids

Composition

The hydrophobic amino acids (A, V, I, L and M) contain aliphatic side chains. There have been no known previous reports of structures formed from the self-assembly of these amino acids. However, the dipeptide Fmoc-AA has been previously shown to form fibrils through pH switching. Other Fmoc dipeptides containing leucine are also capable of forming fibres in the presence of the enzyme thermolysin.^{191,192}

The solutions were prepared as previously described (see experimental section). Five concentrations of each amino acid were made up in pH 8 100 mM phosphate buffer, then sonicated briefly and heated gently for 5 mins. The amino acids dissolved easily into clear suspensions before cooling/heating with the exception of Fmoc M, which only fully dissolved after the sonication/heating/cooling cycle. Most solutions stayed as clear suspensions however, Fmoc M transformed into a transparent gel after 6 days. (Figure 4.12).

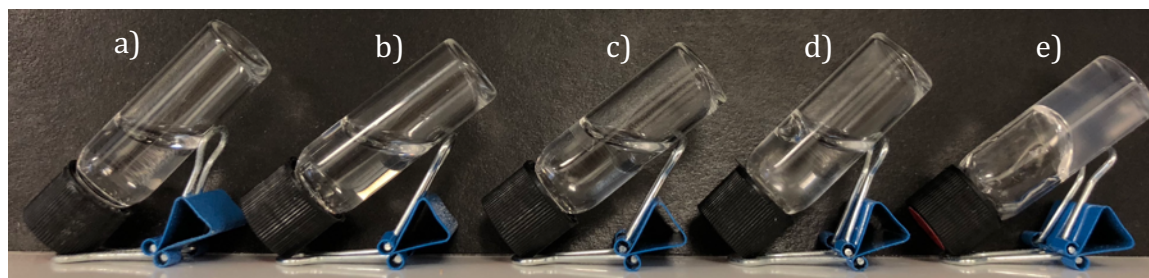


Figure 4.12 Pictures a) Fmoc A; b) Fmoc V; c) Fmoc I; d) Fmoc L and e) Fmoc M after 6 days of self-assembly. 10 mM of each amino acid was added to 1 mL of 100 mM, pH 8 phosphate buffer.

Supramolecular structure and morphology

CD and IR analysis for the range of concentrations for each amino acid is shown in Figure 4.13. No relevant peaks could be observed when amino acid concentrations were below 5 mM. The IR spectra shows that the carbamate peak of the Fmoc is 1680 cm^{-1} , the broadness of the peak suggests that there are intermolecular interactions occurring between the molecules and the slight shift to lower wavenumbers indicates that there is weak hydrogen bonding. The peak at 1590 cm^{-1} is associated with a deprotonated terminal carboxylate group in a micellar formation.¹⁹³ CD analysis for Fmoc A, V and I have poor signal to noise ratio which makes it hard to distinguish between real peaks and noise. However, within the CD spectra of Fmoc M, there are peaks related to the carbonyl of the amino acid and the Fmoc moiety around 220 nm and 250 nm respectively. There is also a small peak appearing at the fluorenyl region around 300 nm. The presence of chiral peaks and the gelation of the 10 mM samples indicates that fibres form in Fmoc M. There are discrepancies for the peaks appearing in Fmoc L as this is very similar to Fmoc D (Figure 4.28b). The reason for this error is an experimental error from the use of a small pathlength cuvette (0.002 cm) which was needed for the measurement to be within a suitable HT voltage (below 600V) that is acceptable for CD analysis.

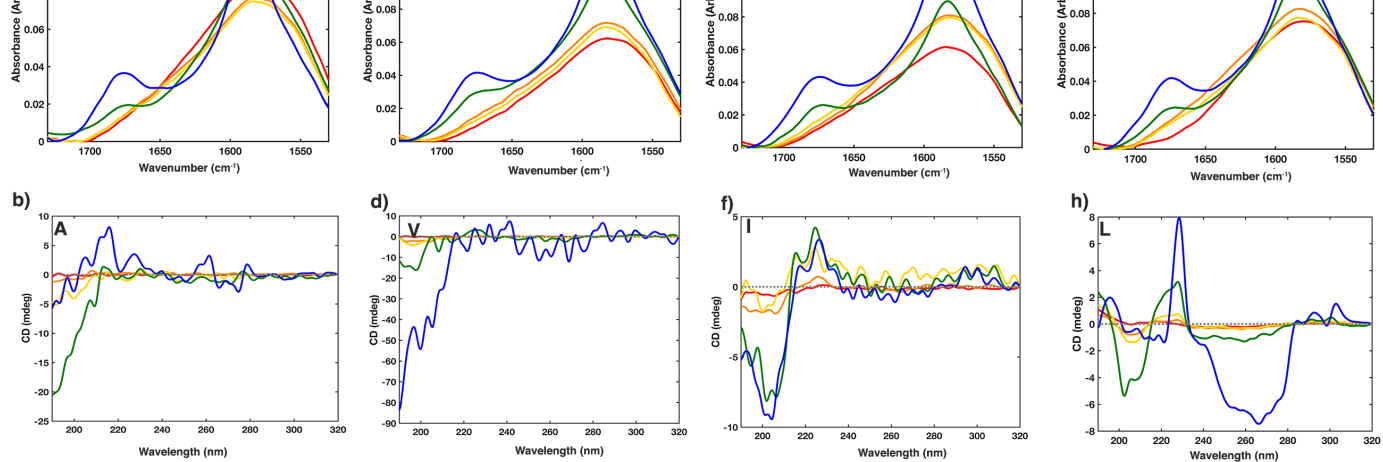


Figure 4.13 Correlating transmission IR and CD spectra of the Fmoc aliphatic amino acids with increasing concentrations of 0.1 mM (red line), 0.5 mM (orange line), 1 mM (yellow line); 5 mM (green line); 10 mM (blue line). a) IR spectra of Fmoc A; b) CD spectra of Fmoc A; c) IR spectra of Fmoc V; d) CD spectra of Fmoc V; e) IR spectra of Fmoc I; f) CD spectra of Fmoc I; g) IR spectra of Fmoc L; h) CD spectra of Fmoc L; i) IR spectra of Fmoc M; j) CD spectra of Fmoc M. Spectra taken after 6 days of self assembly in pH 8 phosphate buffer (D_2O (for FTIR) or H_2O (for CD)). IR spectra is baselined corrected and CD spectra is numerically corrected to have the same pathlength.

Coarse grained simulations and nanoscale morphology

Simulations shown in Figure 4.14, agree with the TEM and AFM data (Figure 4.15). Fmoc A, V and L arranges into clusters with short order. Fmoc A aggregates are more ribbon-like while Fmoc L has a more fibrous-like cluster. Both Fmoc V and Fmoc I contain Fmoc stacking however, these structures stay disordered. However, Fmoc V and I are outliers as the simulations make the structures look as though they are long and flat and experimental data showed that these arranged into small micelles. The reason for the outliers could possibly be due to a loss of resolution using the coarse-grained simulations. Fmoc M consists of a fibre with a small vesicle attached to the end, the Fmoc within the fibrous part of M stacks in a similar way to the aromatic amino acids with a core consisting of four Fmoc. This agrees well with the CD data that indicates fibres have formed.

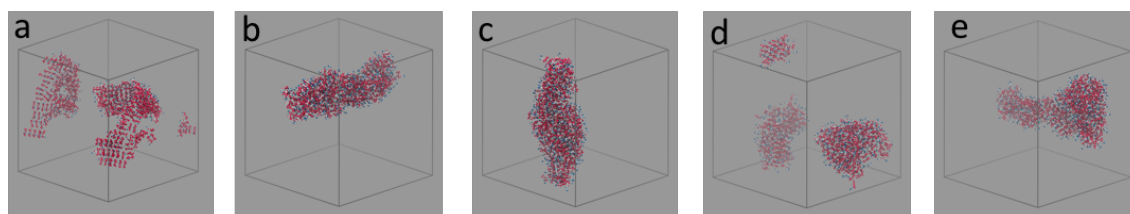


Figure 4.14 Simulations of the hydrophobic amino acids. a) Fmoc A; b) Fmoc V; c) Fmoc I; d) Fmoc L; e) Fmoc M.

TEM and AFM confirm that the majority of structures formed are micellar. AFM profiles are shown in Table 4.1, it should be noted that as the size of the micelle increases relative to the length of the side chain. Fmoc I and Fmoc L are isomers however, Fmoc L assembles into wider but flatter micelles. Fmoc M forms a mixture of micelles and twisted fibres as observed in the simulations, the length of the methionine side chain allows for greater flexibility and the increased hydrophobicity encourages fibrillar formation.

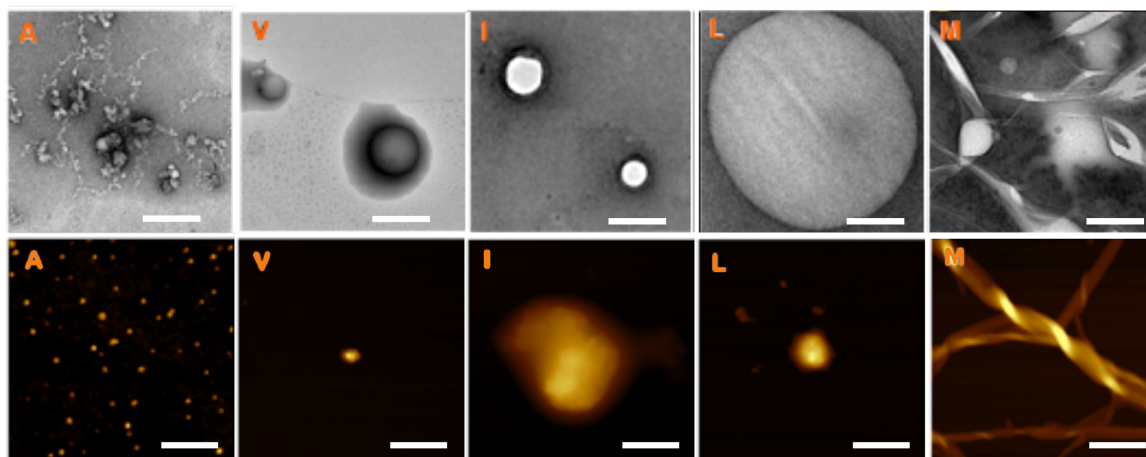


Figure 4.15 Microscopy images of the self-assembled structures formed from the aliphatic Fmoc amino acids, TEM images (top) and AFM images (bottom). From left to right; Fmoc A, Fmoc V, Fmoc I, Fmoc L and Fmoc M. Images acquired after 6 days of self-assembly and all concentrations of amino acids were 10 mM in pH 8 phosphate buffer. Scale bar = 250 nm

Table 4-1 AFM profiles of self-assembled Fmoc protected aliphatic amino acids

AMINO ACID	HEIGHT (nm)	WIDTH (nm)
FMOC A	2.9 ± 0.4	36 ± 6.1
FMOC V	3.9 ± 0.28	46 ± 11
FMOC I	8.2 ± 3.5	78 ± 25
FMOC L	4.4 ± 3.9	105 ± 45
FMOC M	17.4 ± 9.3	129 ± 44

Raman experiments with PEGylated-AuNPs

Raman experiments were conducted as previously described (see experimental section). The SERS spectra (Figure 4.16) of the self-assembled structures with nanoparticles show an enhancement of signals compared to the samples without nanoparticles. This increase in response supports the idea that the nanoparticles are assembled onto the soft templates. Characteristic Fmoc peaks dominate the spectra. The ratio of the aromatic Fmoc 1609 cm^{-1} peak between the sample with and without nanoparticles is shown in Figure 4.17. This reveals that as the side chain increases, the peak ratio of the 1609 cm^{-1} peak decreases thus indicating that the signal enhancement is directly related to the size of the micelles. Moreover, the nanoparticles must be further away from the Fmoc moiety which also suggests that the highly hydrophobic Fmoc moiety is buried within the soft template.

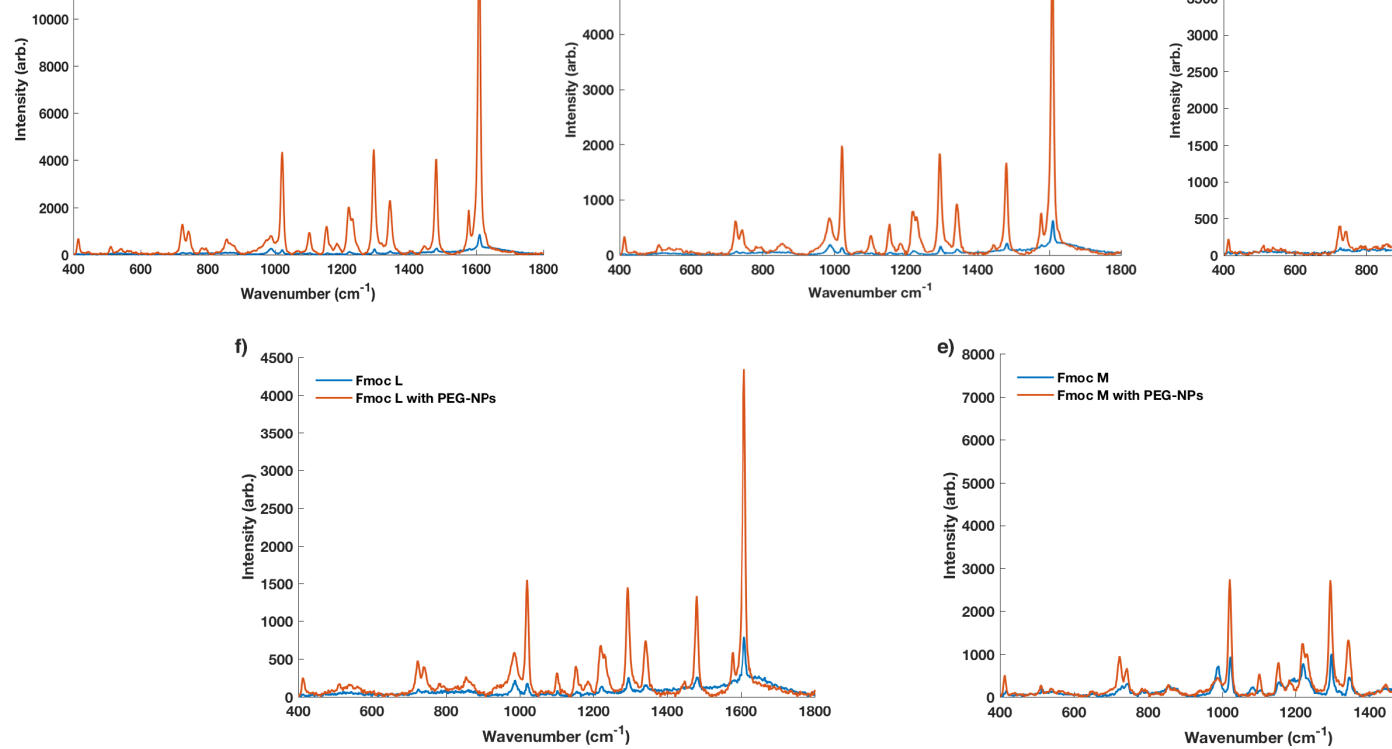


Figure 4.16 Raman spectra of 10 mM Fmoc protected aliphatic amino acids with and without PEGylated gold nanoparticles after 6 days. a) Fmoc A, b) Fmoc V, c) Fmoc I, d) Fmoc L, f) Fmoc M. Spectra taken with a continuous wave (CW) 532 nm laser, 40 mW laser power, acquisition time 3s after 6 days of self-assembly. 20 μ L of each sample was pipetted onto a CaF_2 plate. Careful consideration was taken to not let the sample dry.

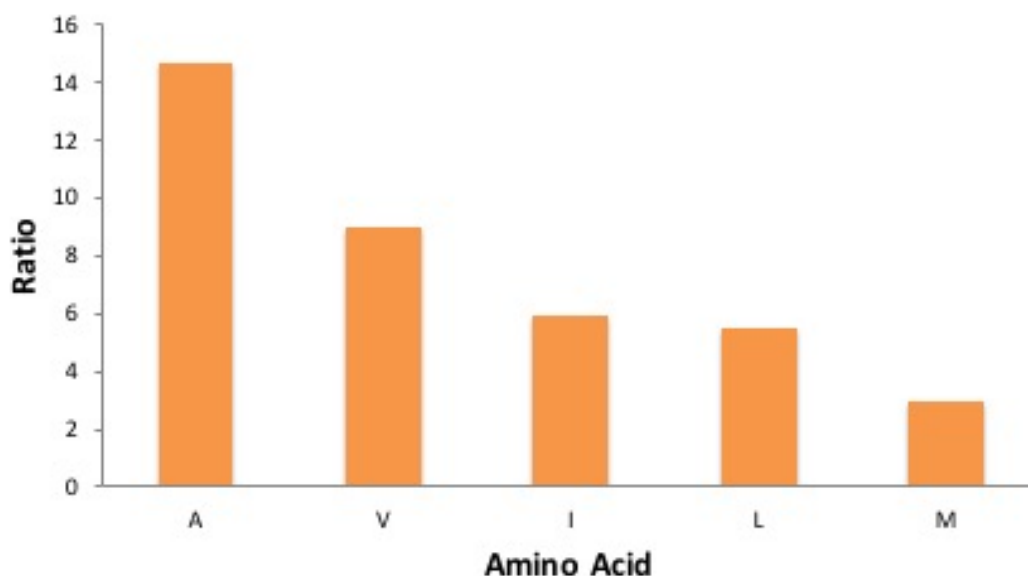


Figure 4.17 Ratio of 1609 cm⁻¹ peak obtained from spectra with and without nanoparticles. As the size of the side chain increases the signal of the characteristic Fmoc peak decreases thus indicating that the nanoparticles are further away from the Fmoc moiety.

Electron microscopy images of the PEGylated nanoparticles with assembled Fmoc A, V and L show that the nanoparticles assemble around the micelles. Fmoc A has the smallest side chains and forms 3D packed clusters, Fmoc V forms 2D hexagonally packed assemblies and Fmoc L, which has an isobutyl side chain generates 1D supraparticles. The TEM images show that there is an increase in nanoparticles around the Fmoc A and as the side chain increases, the number of nanoparticles decrease. This supports the SERS data that tighter packed clusters in Fmoc A will have more ‘hotspot’ formations therefore give the highest enhancement compared to Fmoc L where less nanoparticle interactions will result in less hotspots therefore weaker signals. This type of directed assembly suggests that the micelles from the hydrophobic Fmoc amino acids can be used as soft templates for gold nanoparticle superstructures to create structures with varying degrees of assembly.

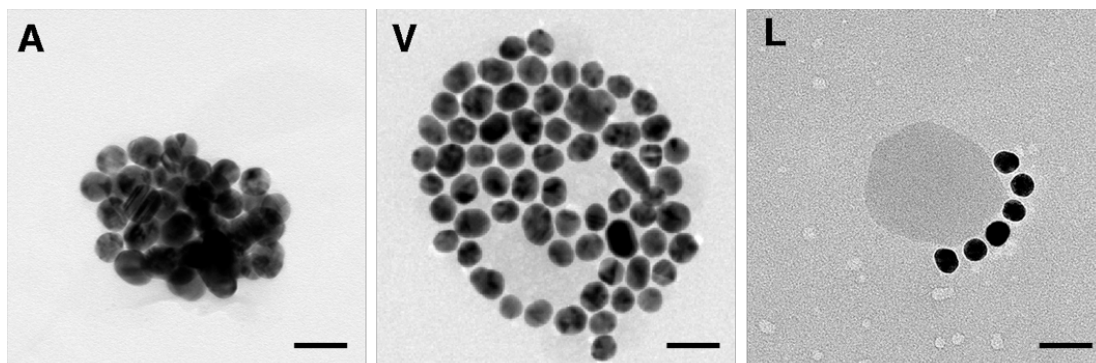


Figure 4.18 TEM imaging of 20 nm PEGylated- gold nanoparticles assembled onto the structures formed from the Fmoc protected aliphatic amino acids A, V and L after 6 days of assembly. The nanoparticles form varying degrees of packing structures from 3D packed clusters to 1D assemblies depending on the length of side chain.

The next set of amino acids which will be discussed are the hydrophilic amino acids, serine (S), threonine (T), asparagine (N) and glutamine (Q).

4.7 Hydrophilic amino acids

Composition

The hydrophilic amino acids are S T N and Q. These amino acids have hydrogen bonding capabilities either through the hydroxyl group of S and T or the carboxamide group of N and Q which can also act as a hydrogen acceptor or donor. Previous studies have shown that Fmoc S assembles into small micelles.¹⁹⁴ Each sample went through the same sonication heating/cooling cycle to keep all variables constant to minimise discrepancies in self-assembly. Fmoc S and T are highly soluble and stayed as homogenous solutions (Figure 4.19a and b). Fmoc N and Q started as milky solutions, after heating turned clear then after cooling, Fmoc N turned into a cloudy solution (Figure 4.19c and d).

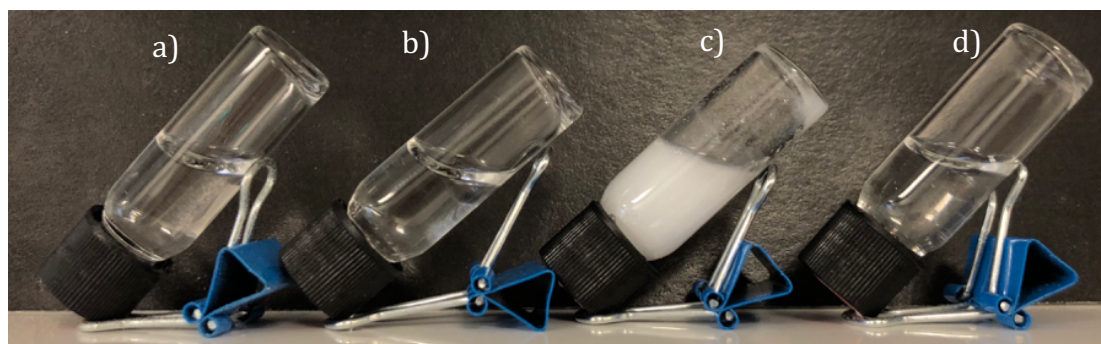


Figure 4.19 Pictures of hydrophilic amino acids after 6 days after assembly in 100 mM pH 8 phosphate buffer; a) Fmoc S; b) Fmoc T; c) Fmoc N; d) Fmoc Q.

Supramolecular structure and morphology

Figure 4.20 shows the IR and CD spectra of the hydrophilic amino acids. As the concentration of the samples increases, the terminal carboxylate whose usual position for micellar formation is at 1590 cm^{-1} shifts to 1595 cm^{-1} in Fmoc S and Fmoc T thus indicating hydrogen bonding. The Fmoc carbamate vibration is also signified by a peak present at 1677 cm^{-1} . The presence and positions of these peaks follow the same trend of micellar self-assembly observed in the aliphatic amino acids. There are no characteristic CD peaks observed for S and T as the signal to noise ratio is very poor suggesting no chirality is present.

For the carboxamide containing hydrophilic amino acids, a small peak appearing at 1659 cm^{-1} within the FTIR spectra of Fmoc N can be assigned to the amide I band this suggests that the fibres may be in an alpha-helix conformation as the

shape of the CD spectra within the Fmoc area (around 305 nm) also exhibits a characteristic alpha helix spectrum (Figure 4.20e).¹⁹⁵ The strong signal observed in Fmoc N and Fmoc Q at 1590 cm^{-1} indicates that the C-terminus carboxylate is deprotonated. Both amino acids have shoulders $\sim 1630 \text{ cm}^{-1}$ related to the $\nu\text{C}=\text{O}$ bands within the carboxamide, these are also downshifted suggesting strong hydrogen bonding.¹⁹⁶ Moreover, the Fmoc carbamate in Q shifts to a lower wavenumber of 1664 cm^{-1} also signifying strong hydrogen bonding. However, there is no signal within the Fmoc region of the CD data thus indicating that the Fmoc moiety is not in a chiral environment

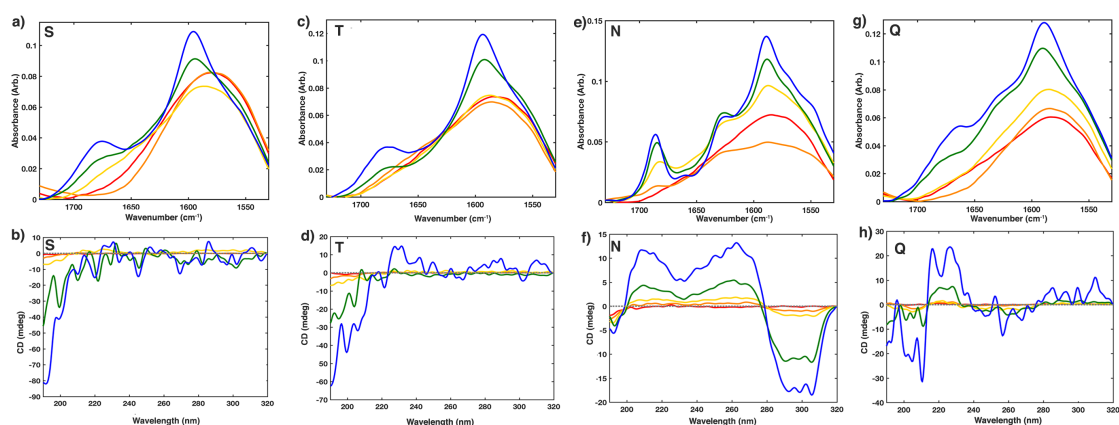


Figure 4.20 Correlating transmission FTIR and CD spectra of the Fmoc hydrophilic amino acids with increasing concentrations of 0.1 mM (red line), 0.5 mM (orange line), 1 mM (yellow line); 5 mM (green line); 10 mM (blue line) of: a) FTIR spectra of Fmoc S; b) CD spectra of Fmoc S; c) FTIR spectra of Fmoc T; d) CD spectra of Fmoc T; e) FTIR spectra of Fmoc N; f) CD spectra of Fmoc N; g) FTIR spectra of Fmoc Q; h) CD spectra of Fmoc Q; FTIR spectra is baselined corrected. The pathlength of the CD spectra is numerically corrected.

Coarse grained simulations and nanoscale morphology

The simulations also show that Fmoc S and Fmoc T form aggregates (Figure 4.21). Fmoc S forms small fibre like structures and there is Fmoc π - π stacking in Fmoc T. Both clusters formed do not have any long-range order. The presence of aggregate formation is confirmed by AFM and TEM imaging shown in Figure 4.22. The simulations for Fmoc N show that the Fmoc interactions are similar to the aromatic amino acids, however it was suggested that there is a possibility the interactions can become stronger, and the structures will start to become crystalline (Figure 4.21). The simulations also show that Fmoc N is capable of

forming broader ribbons, this is further confirmed by the AFM and TEM data (Figure 4.22) and supported by the CD and IR data. Fmoc Q has an Fmoc core which is extended in-plane (Figure 4.21) allowing it to become more ribbon-like which supplements the CD data which suggests no chiral environments. TEM and AFM analysis confirms the presence of flat ribbons in Fmoc Q.

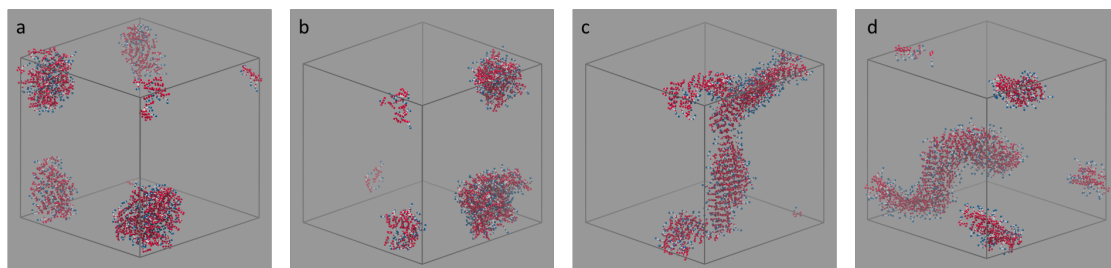


Figure 4.21 Coarse-Grained simulations of; a) Fmoc S; b) Fmoc T; c) Fmoc N; d) Fmoc Q. Fmoc S and Fmoc T forms small aggregates while Fmoc N has a core of four Fmoc moieties with strong interactions. Fmoc Q has a core which is extended in-plane allowing the structure to become more ribbon-like.

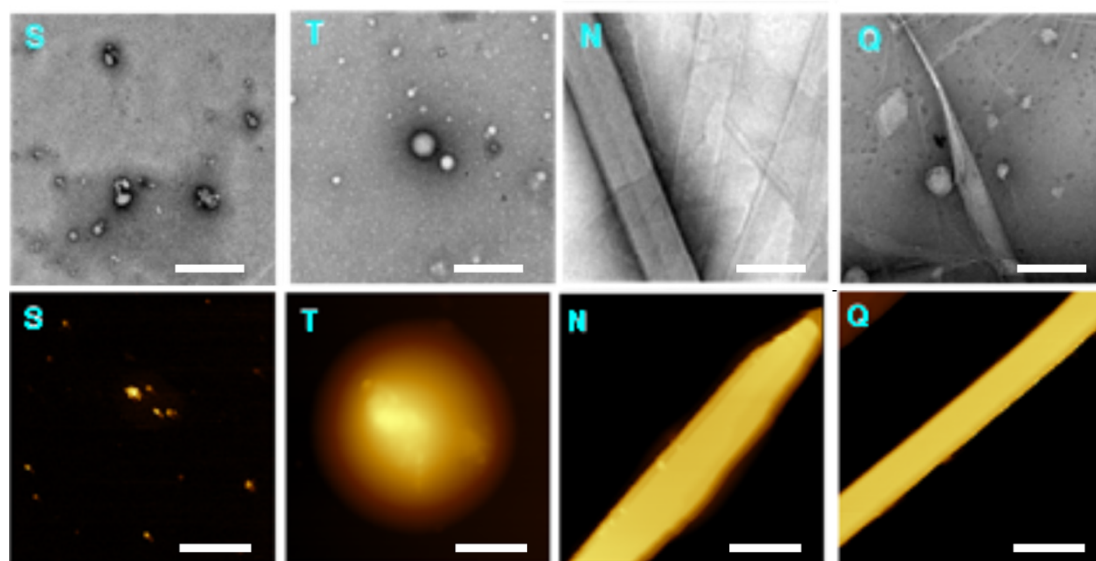


Figure 4.22 Microscopy images of the self-assembled structures formed from the aliphatic Fmoc amino acids, TEM images (top) and AFM images (bottom). From left to right; Fmoc S, Fmoc T, Fmoc N, and Fmoc Q. All concentrations of amino acids were 10 mM. Scale bar = 250 nm

Raman experiments with PEGylated-AuNPs

SERS spectra of Fmoc S and Fmoc T with PEGylated gold nanoparticles (PEG₁₂-AuNP) is shown in Figure 4.23. There is significant SERS enhancement of the characteristic Fmoc peaks in both amino acids thus indicating that the nanoparticles are closely interacting with the Fmoc monomer micelles. TEM analysis of PEG₁₂-AuNP/Fmoc S and SEM analysis of PEG₁₂-AuNP/Fmoc T (Figure 4.24) confirms that the nanoparticles assemble around the micelles in tight clusters. A slight increase in the ratio of the 1609 cm⁻¹ signal observed in Fmoc T compared to Fmoc S suggests that more nanoparticles are interacting with Fmoc T consequently creating more hotspots. SEM data of Fmoc T shows that the nanoparticles are hexagonally packed around micelle and are more densely packed around the centre of the micelle.

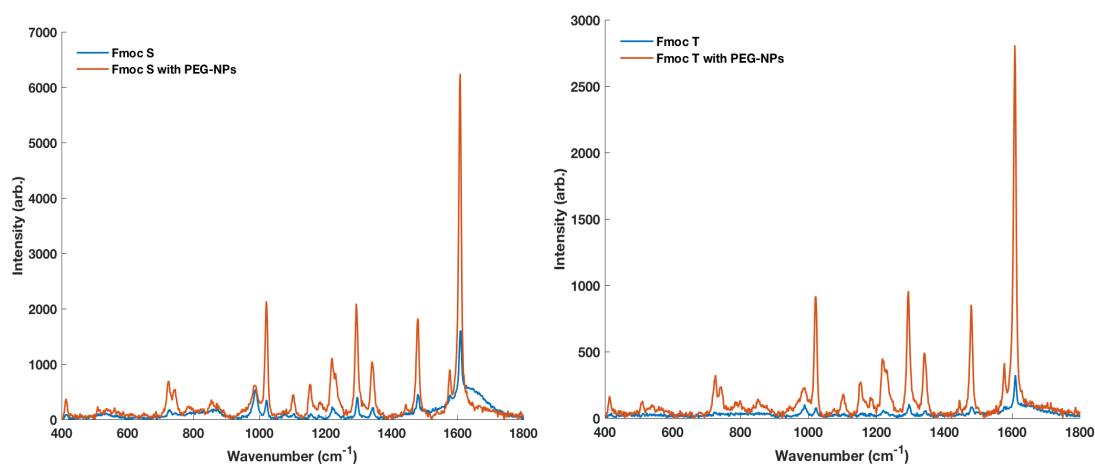


Figure 4.23 Raman spectra of 10 mM Fmoc protected amino acids with and without PEGylated gold nanoparticles after 6 days; Fmoc S (left) and Fmoc T (right) Spectra taken with a continuous wave (CW) 532 nm laser, 40 mW laser power, acquisition time 3s. 20 μ L of each sample was pipetted onto a CaF₂ plate. Careful consideration was taken to not let the sample dry.

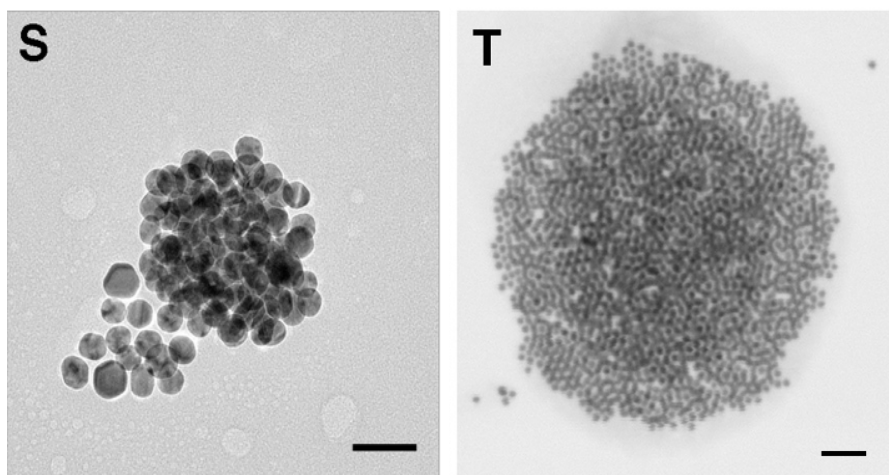


Figure 4.24 Electron microscopy images. TEM of 20 nm PEGylated- gold nanoparticles interacting with Fmoc S (left, Scale bar = 50 nm) and SEM imaging of 20 nm PEGylated- gold nanoparticles interacting with Fmoc T (right, Scale bar = 100 nm). Imaging was taken after 6 days of assembly

Raman experiments with Fmoc N showed that the presence of nanoparticles does not enhance or drastically change the signal which signifies that the nanoparticles exhibit little interaction with the ribbons formed. However, there are signal enhancements for Fmoc Q, it is interesting to note that there has been no Raman enhancement from previous fibrous structures formed. The reason for the signal enhancement may be due to Fmoc Q having an extended in-plane orientation of Fmoc rather than an Fmoc core therefore the nanoparticles are able to interact more closely with the Fmoc moiety.

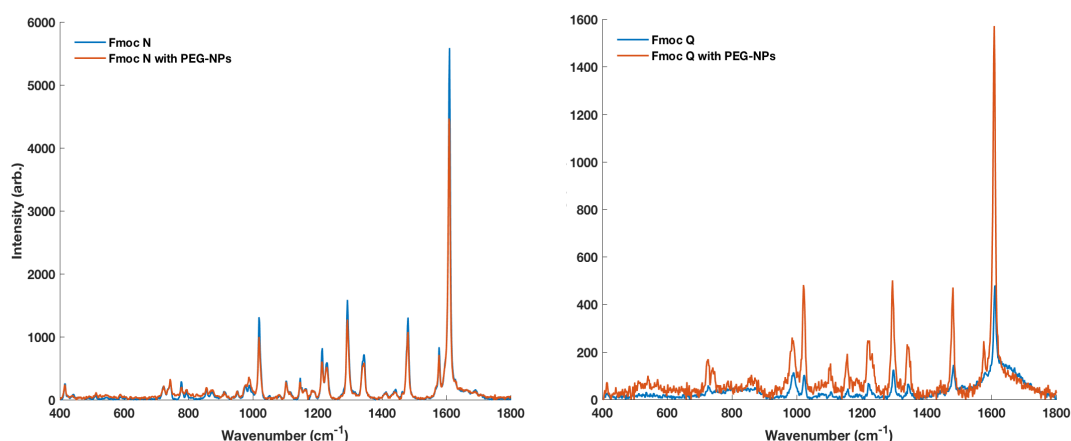


Figure 4.25 Raman spectra of 10 mM Fmoc protected amino acids with and without PEGylated gold nanoparticles after 6 days; Fmoc N (left) and Fmoc Q (right) Spectra taken with a continuous wave (CW) 532 nm laser, 40 mW laser power, acquisition time 3s.

The next set of amino acids which will be discussed are the charged amino acids. These include the negatively charged amino acids aspartic acid (D) and glutamic acid (E) and the positively charged amino acids arginine (R), lysine (K) and histidine (H).

4.8 Charged Amino Acids

Composition

The negatively charged amino acids, D and E have carboxylic acid side chains. Moreover, the side chain of E is one carbon longer than D which also gives it a higher pKa. Both Fmoc D and E were highly soluble (Figure 4.26).

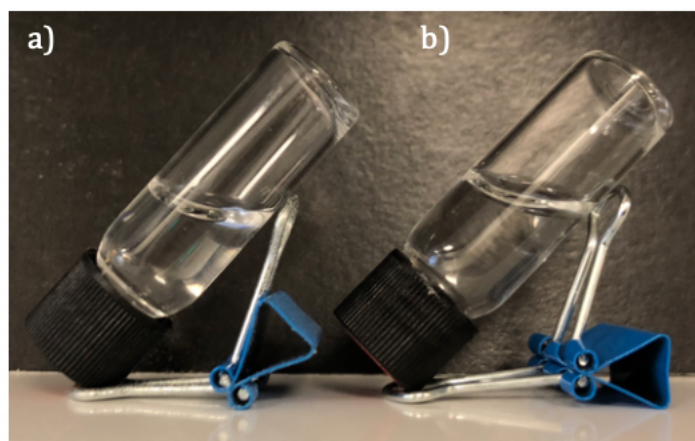


Figure 4.26 Pictures of negative amino acids after 6 days of assembly. a) Fmoc D and b) Fmoc E. 10 mM of each amino acids was added to 100 mM, pH 8 phosphate buffer

The positively charged amino acids are R, K and H which are protonated in pH 8 phosphate buffer. H is also aromatic thus has π bonding capabilities. Fmoc R and K did not dissolve in the buffer and stayed as cloudy suspensions even after the heating/cooling cycle (Figure 4.27).

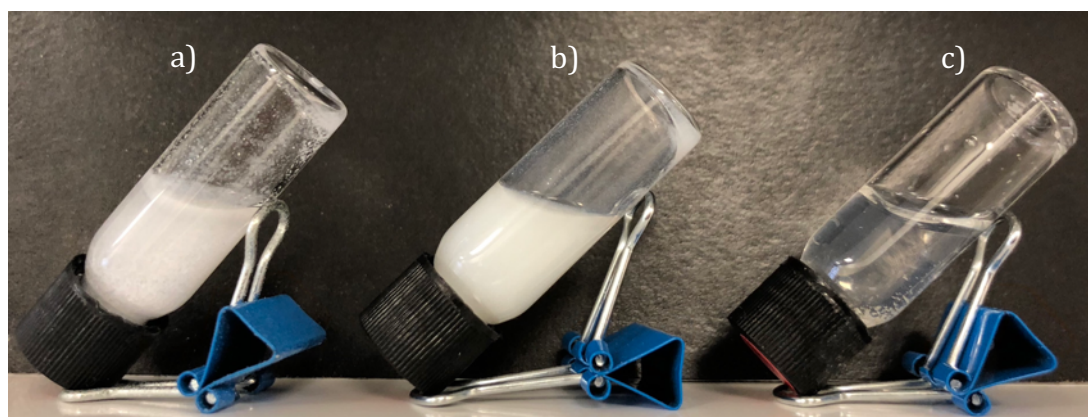


Figure 4.27 Pictures of positive Fmoc amino acids taken after 6 days a) Fmoc R; b) Fmoc K; c) Fmoc H. 10 mM of each amino acids was added to 100 mM, pH 8 phosphate buffer

Supramolecular structure and morphology

Figure 4.28 shows the CD and FTIR spectra of Fmoc D and E. The Fmoc peak is hydrogen bonded at 1678 cm^{-1} . The COO^- of Fmoc D overlaps with presence of the amide I band around 1578 cm^{-1} hence the broad distribution under the peak. The amide I band does not overlap with the COO^- band in Fmoc E and the COO^- is observed at 1565 cm^{-1} .¹⁹⁷ The CD spectra has poor signal to noise ratio which indicates there is no obvious chirality. The peaks observed in the 10 mM sample of Fmoc E are similar to those observed in 10 mM of Fmoc L (Figure 4.13h). This is due to an experimental error from either a defective cuvette or the poor correction of the spectra. The absence of the 1590 cm^{-1} peak in the FTIR spectra suggests the terminal carboxylate is protonated and the position of the Fmoc carbamate and the presence of the amide I band indicates that the structure of the micelles is highly ordered.

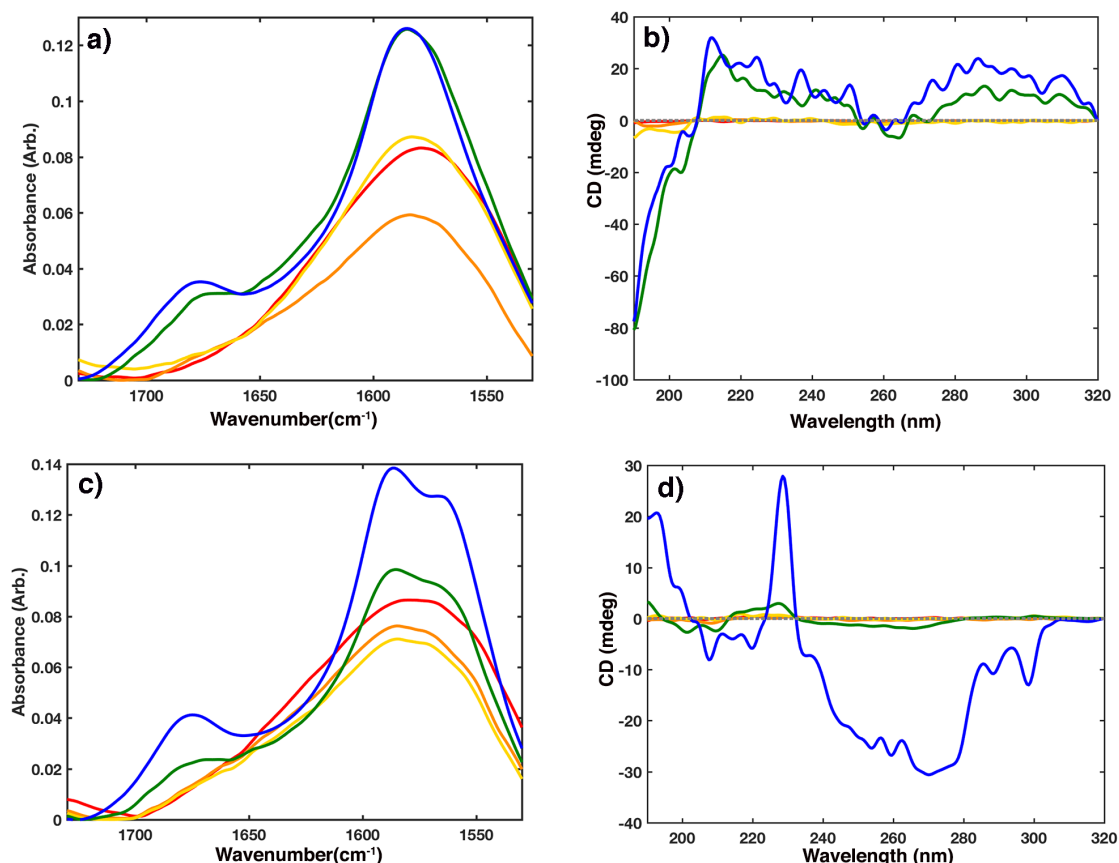


Figure 4.28 Correlating transmission IR and CD spectra of the Fmoc negatively charged amino acids D and E with increasing concentrations of 0.1 mM (red line), 0.5 mM (orange line), 1 mM (yellow line); 5 mM (green line); 10 mM (blue line) of: a) IR spectra of Fmoc D; b) CD spectra of Fmoc D; c) IR spectra of Fmoc E; d) CD spectra of Fmoc E. Spectra taken after 6 days of self assembly in pH 8 phosphate buffer (D_2O (for FTIR) or H_2O (for CD)). IR spectra is baselined corrected and CD spectra pathlength is numerically corrected in order to compare measurements.

Figure 4.30 shows the FTIR and CD spectra of the positively charged amino acids. Within the FTIR spectra of Fmoc H there is a peak at 1708 cm^{-1} and a shoulder at 1676 cm^{-1} , these can be related to the amide I band and the Fmoc carbamate. Previous studies have reported that protonation of the imidazole chain affects the position of the amide I band by increasing it to a higher wavenumber.¹⁹⁸ The carboxylate peak is evident at 1592 cm^{-1} , similar to the trend of previous amino acids which have assembled into micelles.

The Fmoc carbamate and the amide I band can be assigned at 1686 and 1587 cm^{-1} respectively in Fmoc R. There are also side chain peaks that arise from the in-plane bending symmetrical vibration of $CN_3H_5^+$ at 1644 cm^{-1} and the asymmetrical stretching of $CN_3H_5^+$ around 1670 cm^{-1} .¹⁹⁹ Within the CD spectrum of R there are

negative fluorenyl peaks of the Fmoc and positive red-shifted peaks from the carbonyl around 250 nm suggesting that fibres have formed with opposing handedness. Fmoc K shows a weak carbamate band at 1678 cm^{-1} . The overlap of the amide I band with in-plane symmetrical and asymmetrical vibrations of the NH_3^+ of the side chain gives rise to the broad band at 1600 cm^{-1} .

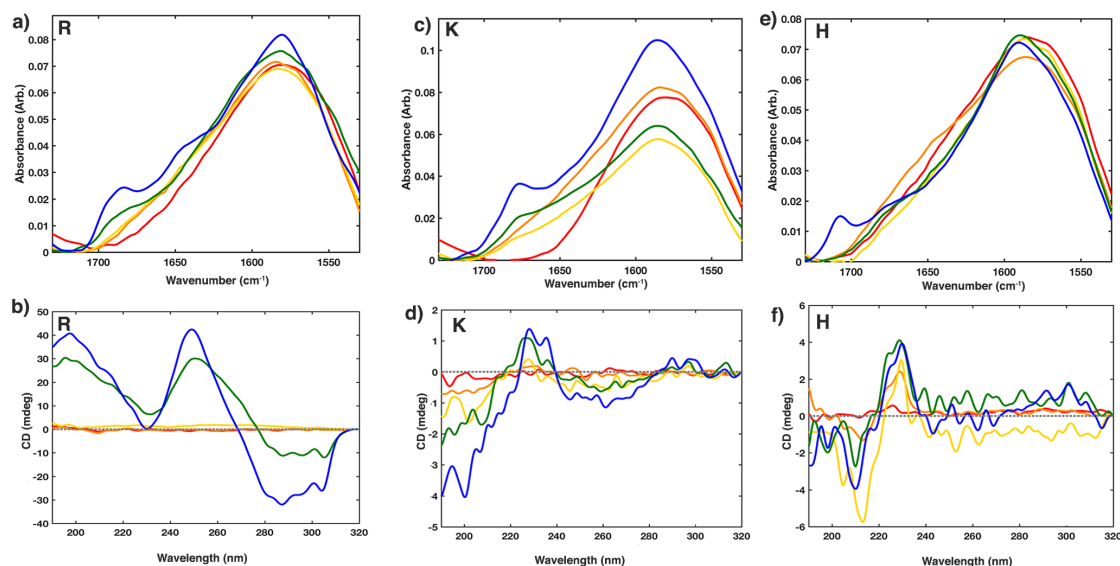


Figure 4.29 Correlating transmission FTIR and CD spectra of the Fmoc positively charged amino acids R, K and H with increasing concentrations of 0.1 mM (red line), 0.5 mM (orange line), 1 mM (yellow line); 5 mM (green line); 10 mM (blue line) of: a) IR spectra of Fmoc R; b) CD spectra of Fmoc R; c) IR spectra of Fmoc K; d) CD spectra of Fmoc K; e) IR spectra of Fmoc H; f) CD spectra of Fmoc H. IR spectra is baselined corrected and CD spectra pathlength is numerically corrected in order to compare measurements.

Coarse grained simulations and nanoscale morphology

Simulations of Fmoc D and Fmoc E corroborate with the experimental data suggesting that highly ordered structures are formed in clusters (Figure 4.30). TEM data shows that elongated micelles have formed in both Fmoc D and Fmoc E while AFM shows small micelles (Figure 4.31).

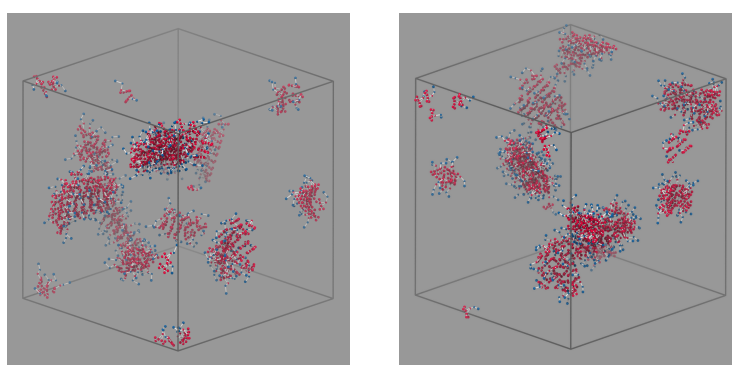


Figure 4.30 Coarse grained simulations of Fmoc D (left) and Fmoc E (right)

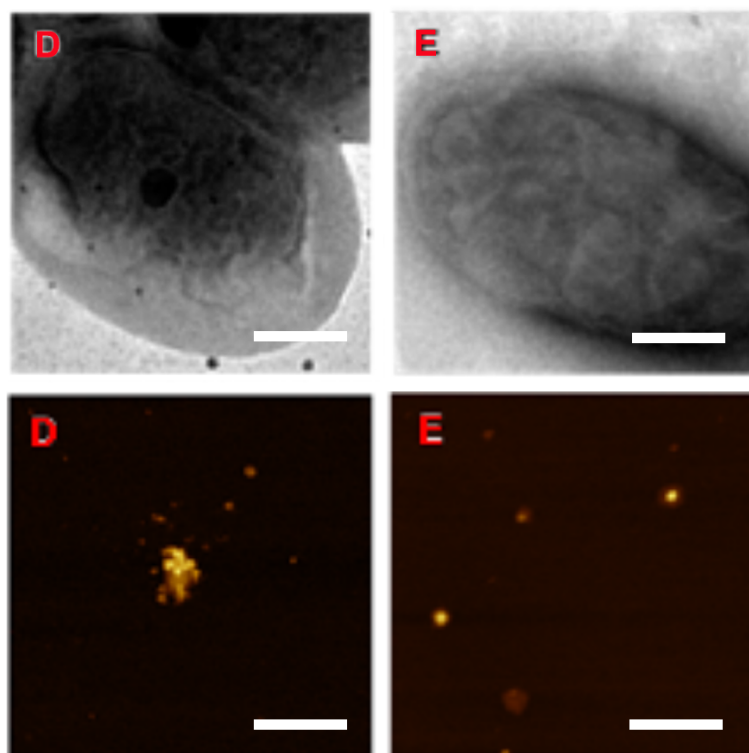


Figure 4.31 Microscopy images of the self-assembled structures formed after 6 days of assembly from the negative Fmoc amino acids, TEM images (top) and AFM images (bottom); Fmoc D (left) and Fmoc E(right). Scale bar = 250 nm

Simulations of the positive amino acids show that Fmoc H is capable of forming fibres with a Fmoc core although this is not evident in the any of the experimental data and there were no obvious signs of chirality in the CD data (Figure 4.31). Simulations show that Fmoc R self assembles with an Fmoc core, while Fmoc K follows an extended in-plane core similar to Fmoc Q (Figure 4.32). It should be noted that the CD data of both ribbon-like structures of Fmoc Q and Fmoc K show no chirality of Fmoc. TEM and AFM corroborates simulations and spectral data that R assembles into plates and K into thin ribbon structures (Figure 4.33).

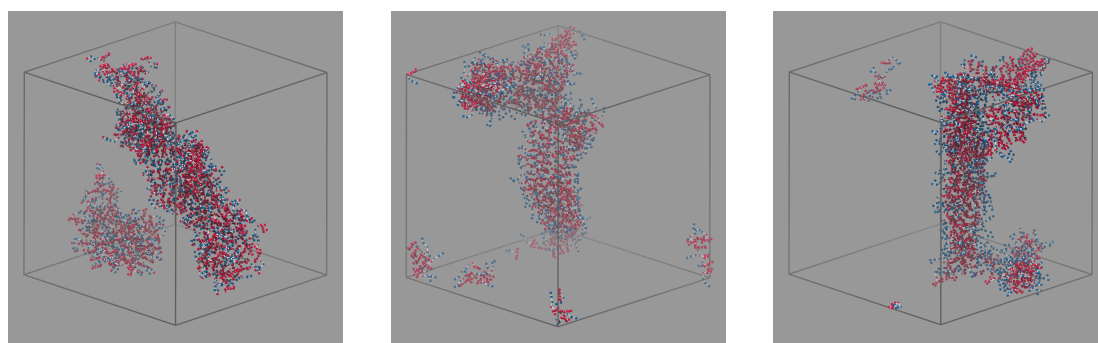


Figure 4.32 Coarse grained simulations of Fmoc R (left); Fmoc K (middle) and Fmoc H (right)

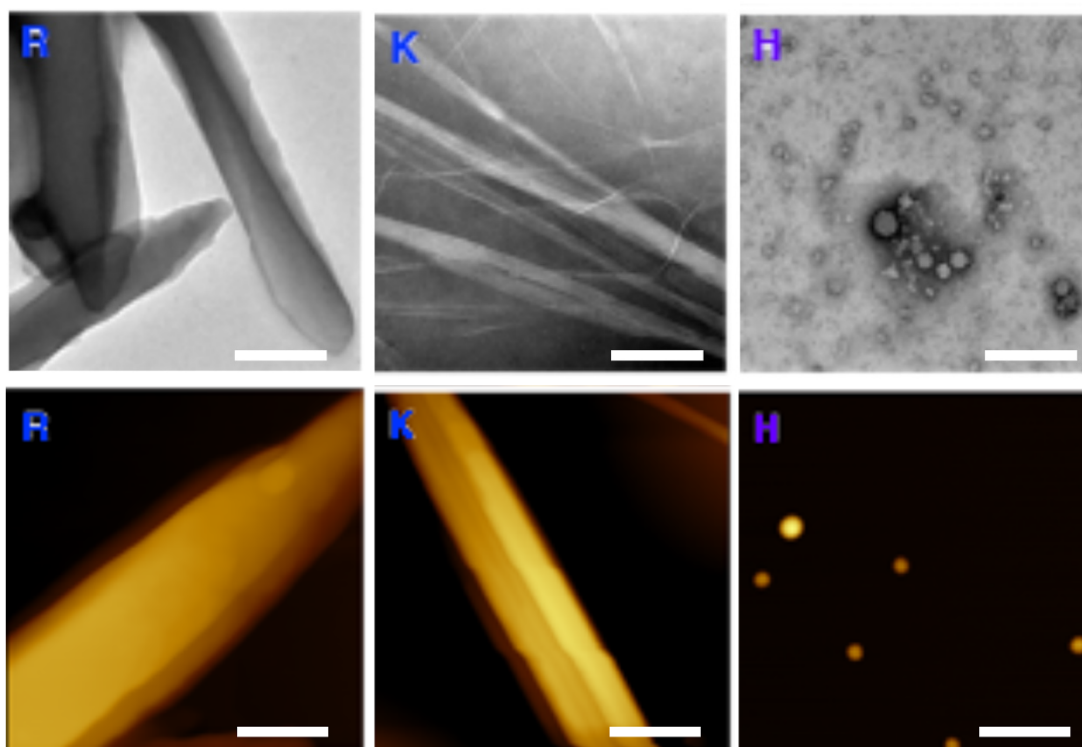


Figure 4.33 Microscopy images of the self-assembled structures formed from the positive Fmoc amino acids after 6 days of assembly, TEM images (top) and AFM images (bottom). From left to right; Fmoc R, Fmoc K and Fmoc H. Scale bar = 250 nm

Raman experiments with PEGylated-AuNPs

As before, PEGylated gold nanoparticles were added to the 10 mM samples before self-assembly. The SERS enhancement of from the samples of nanoparticles with Fmoc E is slightly greater than that of Fmoc D (Figure 4.34), this is also evident from the TEM analysis where there seems to be a greater population of nanoparticles on the periphery of the micelles on Fmoc E (Figure 4.35). The nanoparticles are aggregated randomly on the surface of D while on E, they are ordered (Figure 4.35). One possible reason for this arrangement could be that the extra length of E exposes the COO⁻ of the side chain which allows the carboxylate end of the PEG on the nanoparticles to interact and arrange more neatly on the surface.

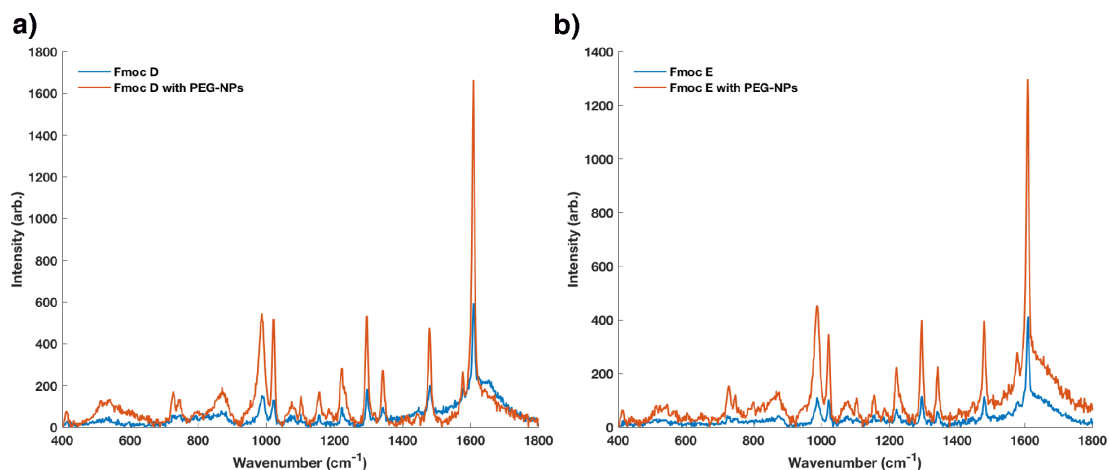


Figure 4.34 Raman spectra and SERS spectra of 10 mM Fmoc protected amino acids with and without PEGylated gold nanoparticles after 6 days; Fmoc D (left) and Fmoc E (right) Spectra taken with a continuous wave (CW) 532 nm laser, 40 mW laser power, acquisition time 3s.

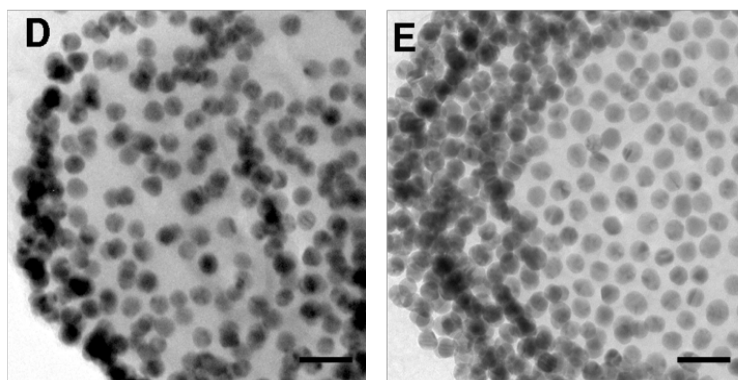


Figure 4.35 TEM images of 20 nm PEGylated- gold nanoparticles interacting with Fmoc D (left) and Fmoc E (right) after 6 days of assembly. Scale bar 50 nm. The nanoparticles are randomly aggregated on the surface of D while they are arranged orderly on the surface of E.

The Raman experiments from R and K gave similar results to the previous fibrous structures (Figure 4.36). The nanoparticles do not add increase the signal, in fact the presence of nanoparticles seem to inhibit the formation of the self-assembled structures. The SERS spectra of Fmoc H shows a very intense peak at 987 cm^{-1} , this peak is usually associated with the Fmoc moiety. However, possibly due to the

orientation of the molecule, this peak dominates over the other characteristic Fmoc peaks.

The next set of amino acids to be discussed are the 'other' amino acids cysteine (C), proline (P) and glycine (G). These cannot be placed into any of the previous categories as they have their own unique characteristics

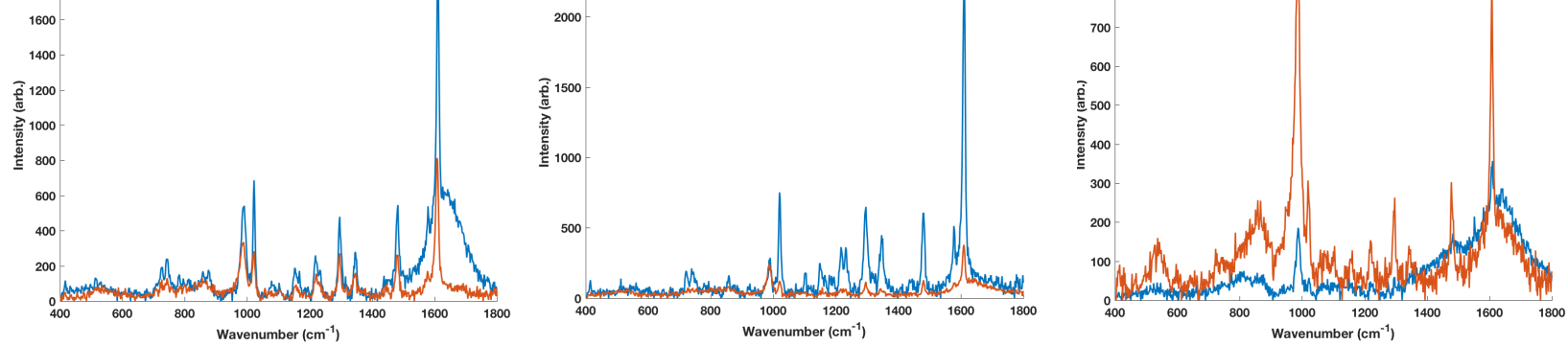


Figure 4.36 Raman experiments with 10 mM Fmoc protected amino acids with and without PEGylated gold nanoparticles after 6 days; Fmoc K (left); Fmoc R (middle) and Fmoc H (right). Spectra taken with a continuous wave (CW) 532 nm laser, 40 mW laser power, acquisition time 3s.

4.9 'Other' amino acid

Glycine

Fmoc G is the simplest amino acid with only a hydrogen side as a side chain. It is the only amino acid which is not chiral. Fmoc G dissolved easily into a homogenous solution (Figure 4.37).



Figure 4.37 Picture of Fmoc G after 6 days. 10 mM of Fmoc G was added to 1 mL of 100 mM, pH 8 phosphate buffer.

The FTIR spectra has a carbamate peak at 1682 cm^{-1} and a COO^- peak at 1593 cm^{-1} , typical of micellar structures previously reported (Figure 4.38). There is also a shoulder around 1649 cm^{-1} and 1561 cm^{-1} relating to the amide I and amide II respectively. This suggest that there is some order within the micelles. The CD spectrum is as expected showing no signs of chirality.

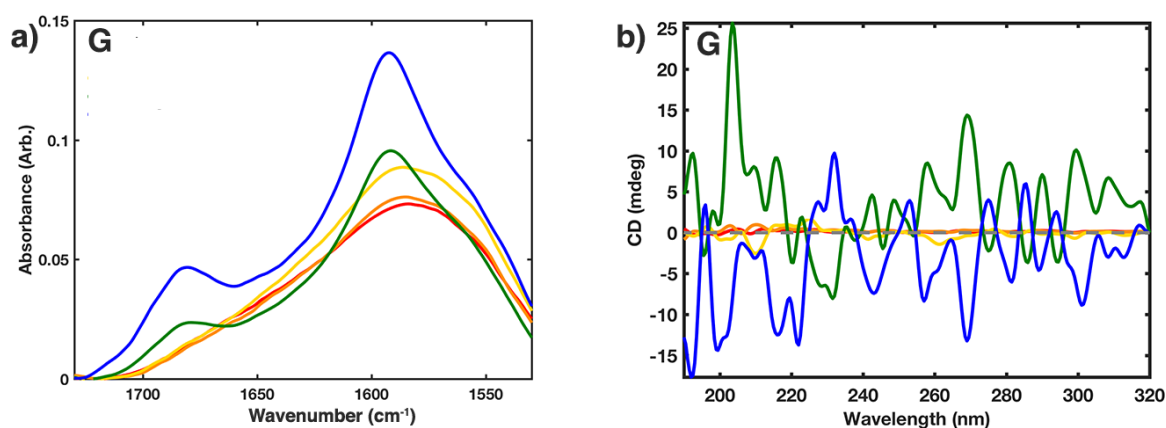


Figure 4.38 Correlating FTIR data (a) and CD data (b) of Fmoc G after 6 days with increasing concentrations of 0.1 mM (red line), 0.5 mM (orange line), 1 mM (yellow line); 5 mM (green line); 10 mM (blue line). IR spectra is baselined corrected and CD spectra pathlength is numerically corrected in order to compare measurements.

Coarse grained simulations show that Fmoc G assembles into membranes with ribbon like domains (Figure 4.39). This does not agree with the rest of the data as TEM and AFM data show small micelles which agree with the FTIR (Figure 4.40).

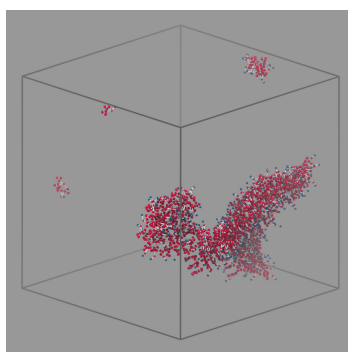


Figure 4.39 Coarse grained simulations of Fmoc G

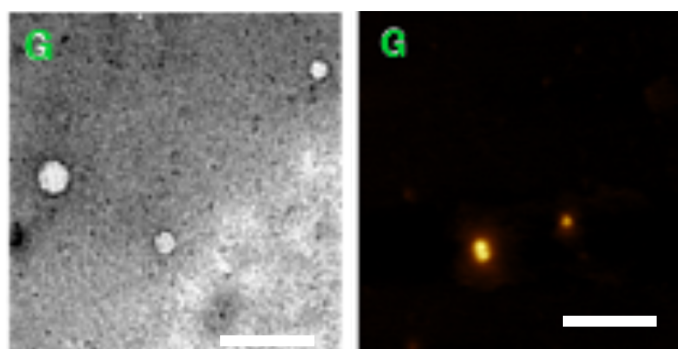


Figure 4.40 Microscopy images of the self-assembled structures formed from Fmoc G; TEM images (left) and AFM images (right) Scale bar= 250 nm

Raman experiments of Fmoc G with PEGylated nanoparticles are shown in Figure 4.41. The PEGylated nanoparticles double the Fmoc signal suggesting that the

nanoparticles do interact with self-assembled Fmoc glycine but are not as tightly packed as the hydrophobic amino acids.

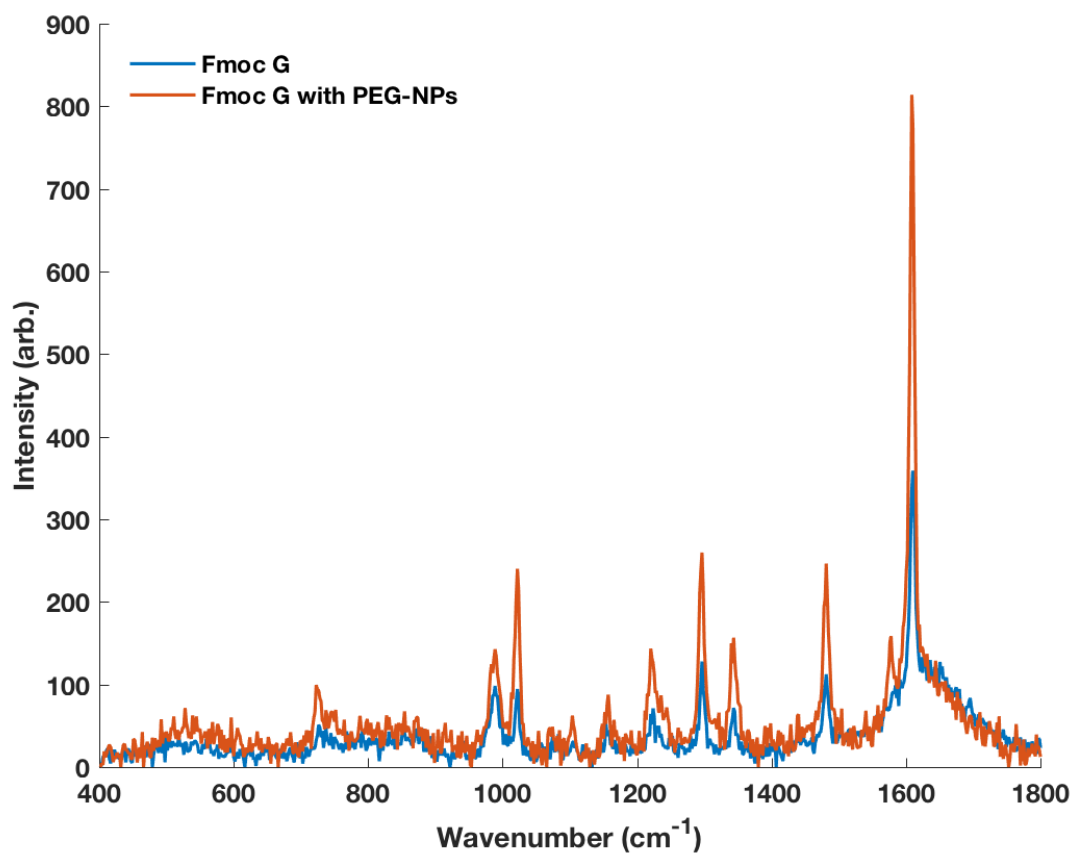


Figure 4.41 Raman experiments with 10 mM Fmoc G. Spectra taken with a continuous wave (CW) 532 nm laser, 40 mW laser power, acquisition time 3s after 6 days of assembly.

Proline

Proline is the only amino acid with its α -amine incorporated into its side chain which can cause rigidity during self-assembly. The Fmoc protected proline stayed as a clear solution (Figure 4.42)

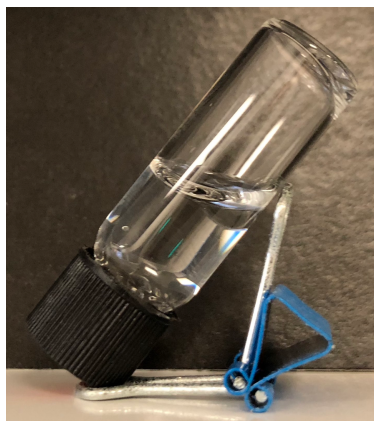


Figure 4.42 Picture of Fmoc P after 6 days. 10 mM of Fmoc P was added to 1 mL of 100 mM, pH 8 phosphate buffer

Simulations of Fmoc P showed that aggregates form and this is further corroborated with the spectral data and electron microscopy imaging (Figure 4.43). The FTIR data shows a peak at 1587cm^{-1} typical of a deprotonated terminal COO^- in micellar formation while there is a strong hydrogen bonded carbamate Fmoc at 1665cm^{-1} (Figure 4.44). The CD data shows left handed chirality of the proline side chain with increasing concentrations, but no chirality was observed from the Fmoc moiety. AFM and TEM confirm the presence of aggregates (Figure 4.45).

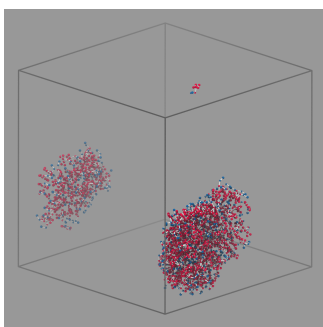


Figure 4.43 Coarse grained simulations of Fmoc P

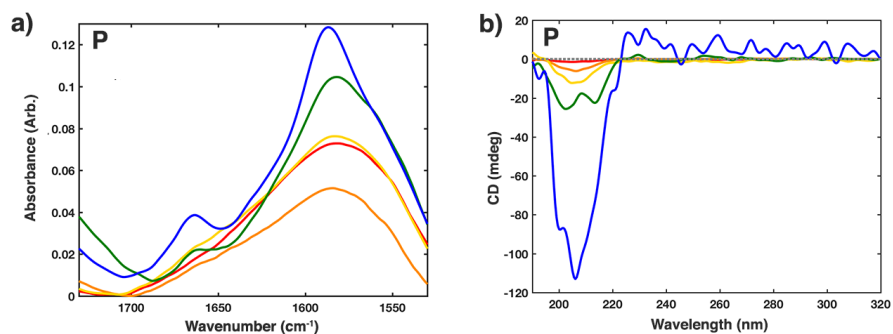


Figure 4.44 Correlating FTIR data (a) and CD data (b) of Fmoc P with increasing concentrations of 0.1 mM (red line), 0.5 mM (orange line), 1 mM (yellow line); 5 mM (green line); 10 mM (blue line). IR spectra is baselined corrected and CD spectra pathlength is numerically corrected in order to compare measurements

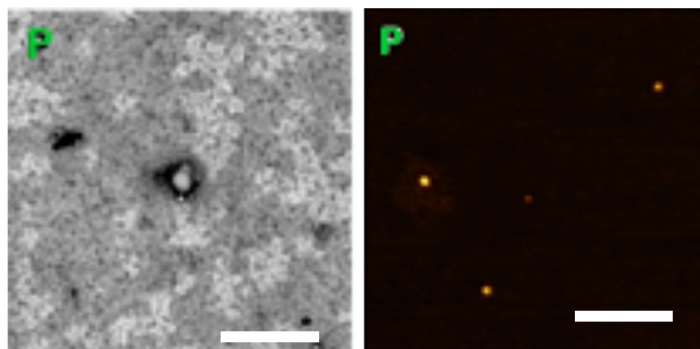


Figure 4.45 Microscopy images of the self-assembled structures formed from Fmoc G; TEM images (left) and AFM images (right) Scale bar 250 nm

Raman and SERS spectra shows that the signal remains unchanged in the presence of 20 nm PEGylated gold nanoparticles (Figure 4.46). This is most likely due to the rigid backbone of the amino acid forming compact aggregates with strongly bonded Fmoc carbamates that does not allow interactions with the nanoparticles.

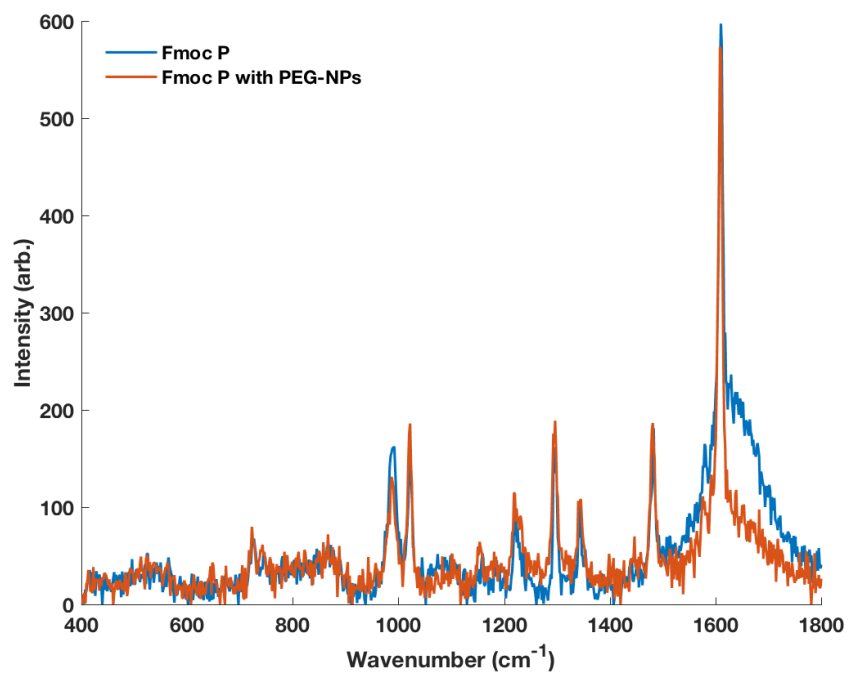


Figure 4.46 Raman and SERS experiments with 10 mM Fmoc G. Spectra taken with a continuous wave (CW) 532 nm laser, 40 mW laser power, acquisition time 3s

Cysteine

Cysteine has a terminal thiol which can undergo oxidation to form disulphide bonds therefore when preparing the sample of Fmoc C, a reducing agent (Tris(2-carboxyethyl) phosphine hydrochloride) was added to ensure that disulphide bonds do not form. After 6 days, the sample turned into a cloudy white mixture (Figure 4.47).

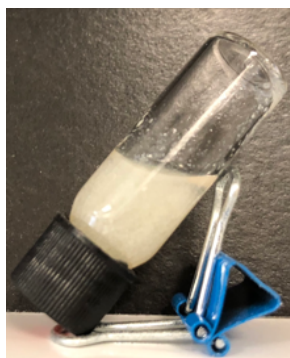


Figure 4.47 Picture of Fmoc C after 6 days. 10 mM of Fmoc C and 20 mM of Tris(2-carboxyethyl) phosphine hydrochloride was added to 1 mL of 100 mM, pH 8 phosphate buffer

FTIR data showed that the Fmoc carbamate peak was very weak and dampened, there was also a sharp terminal carboxyl peak around 1576 cm^{-1} (Figure 4.48). The CD spectra showed no signs of chirality within the Fmoc C sample. Simulations showed that there was π stacking of the Fmoc moiety, although the FTIR data showed a highly downshifted carboxyl group suggesting some intermolecular interactions (Figure 4.49) AFM and TEM data showed that Fmoc C assembled into aggregates with a border or spheres (Figure 4.50).

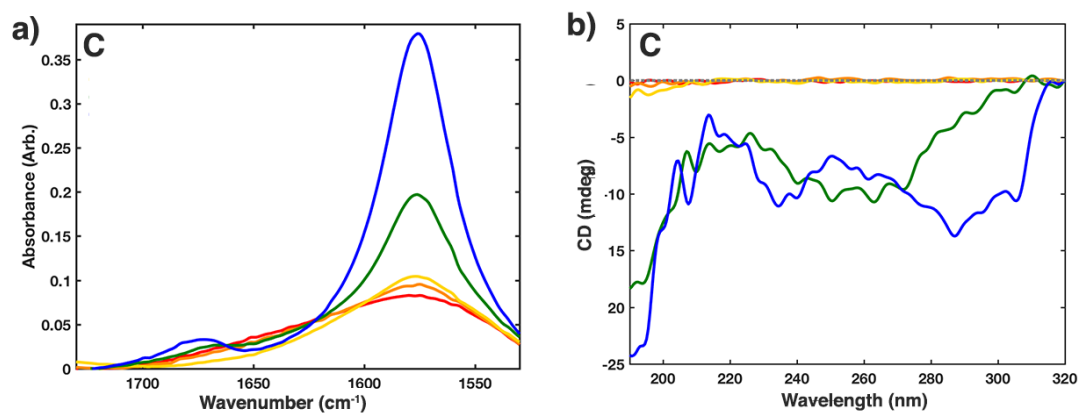


Figure 4.48 Correlating FTIR data (a) and CD data (b) of Fmoc C with increasing concentrations of 0.1 mM (red line), 0.5 mM (orange line), 1 mM (yellow line); 5 mM (green line); 10 mM (blue line).

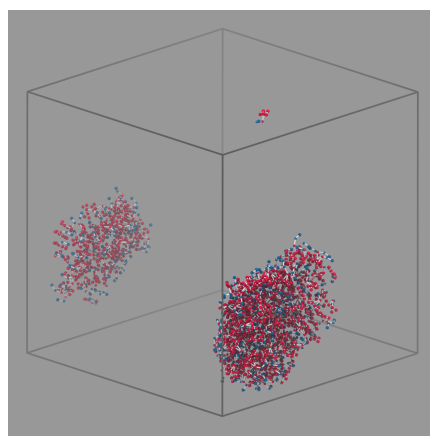


Figure 4.49 Coarse-grained simulations of Fmoc C

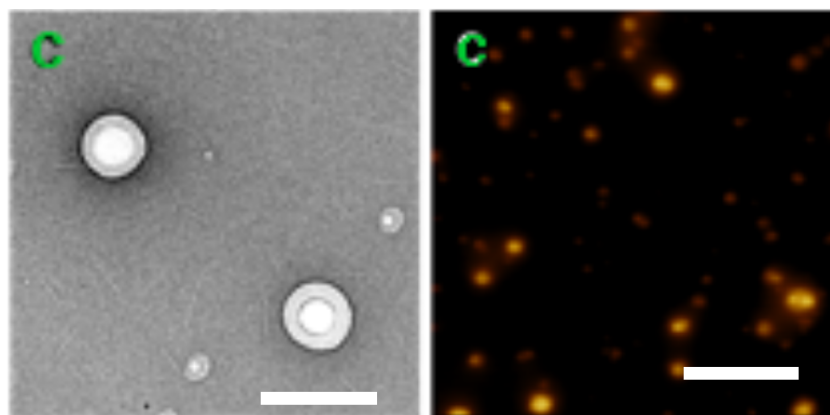


Figure 4.50 Microscopy images of the self-assembled structures formed from Fmoc C; TEM images (left) and AFM images (right) Scale bar 250 nm

When PEGylated gold nanoparticles were added to 10 mM of the Fmoc C, the solution turned from red to purple after 6 days (Figure 4.51). Figure 4.52 shows a normalised spectrum of the change in UV-vis extinction. The λ_{max} red-shifts from 524 nm to 532 nm. This change in extinction is most likely due to the displacement of PEG on the nanoparticle thus causing the thiol group of the cysteine to interact with the nanoparticle causing aggregation. The presence of cysteine has also been known to self-assemble nanoparticles into chains with similar extinction profiles.⁵²

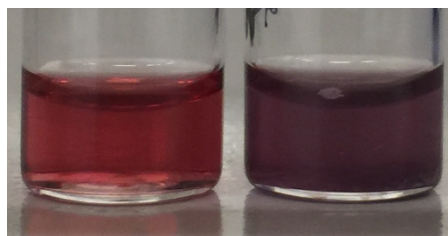


Figure 4.51 Pictures taken of PEGylated gold nanoparticles with Fmoc A(left) and Fmoc C (right) after 6 days of self-assembly. This is to highlight the change of colour observed into Fmoc C compared to the other amino acids.

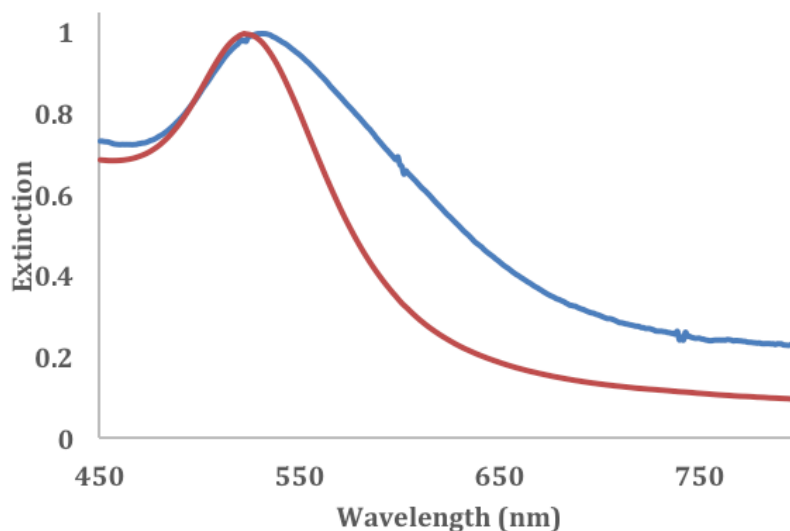


Figure 4.52 UV-Vis spectra of PEGylated gold nanoparticles with Fmoc C after 0 days (red) and 6 days (blue). Measurements were taken with a PMMA cuvette with a pathlength of 1cm and a scan speed of 200 nm/min. The peak has broadened which shows aggregation.

Interestingly, TEM analysis showed that the presence of nanoparticles causes fibres to form (Figure 4.53). However, the nanoparticles do not interact directly with the fibres. This suggests that the nanoparticles do not directly guide the formation of soft fibres but rather promote it via displacement of PEG₁₂. SERS data also revealed that there was no enhancement of the Fmoc moiety which also confirms that the nanoparticles are not interacting with the fibres (Figure 4.54). The absence of a peak around 500 cm⁻¹ shows that cysteine has not assembled via disulphide bridges. The presence of the reducing agent may also be a factor in the assembly of fibres. Further characterisation using FTIR and CD is most likely needed to explain the assembly of fibres in the presence of nanoparticles

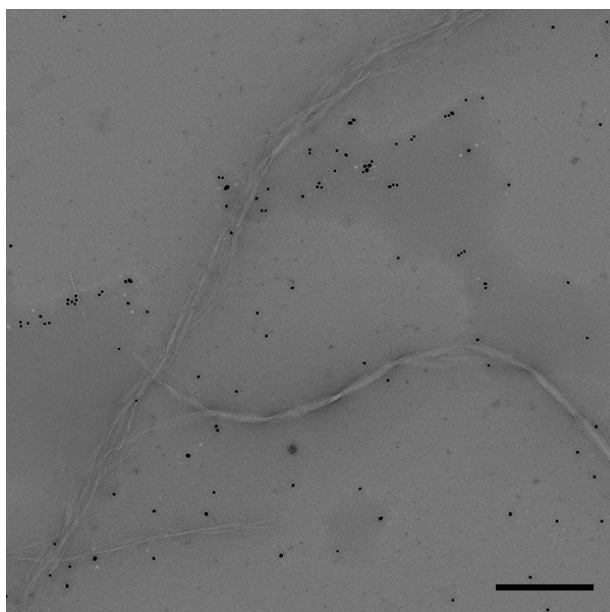


Figure 4.53 TEM analysis of Fmoc C in the presence of PEGylated gold nanoparticles after 6 days. Scale bar = 500 nm

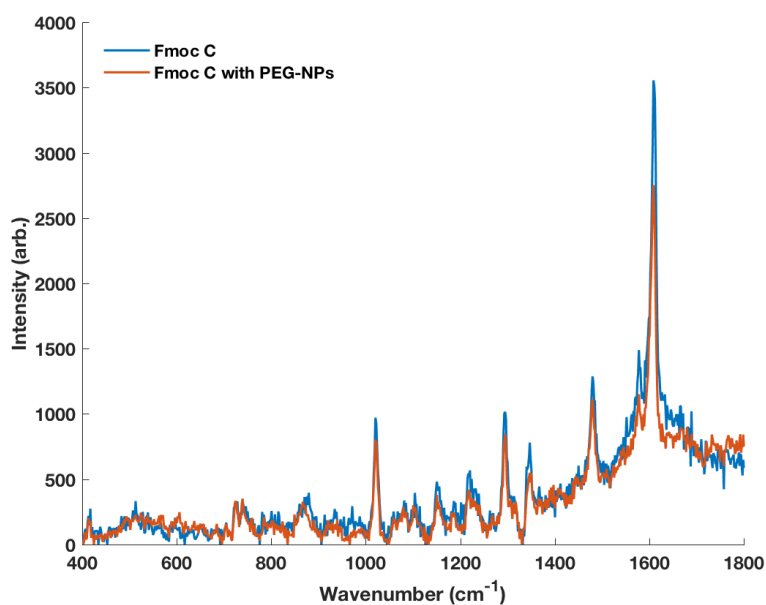


Figure 4.54 Raman and SERS experiments with 10 mM Fmoc C. Spectra taken with a continuous wave (CW) 532 nm laser, 40 mW laser power, acquisition time 3s

4.10 Conclusions and Further work

To conclude, it has been shown that soft templates can be assembled from the Fmoc amino acids with some nanoparticle interaction with the soft templates.

The aromatic amino acids assembled into twisted fibrous structures and the inclusion of nanoparticles seem to inhibit the formation of fibres as shown by the dampening of the Raman signals, the Fmoc core of the fibres are also in a chiral environment as shown by the simulations and CD data.

The hydrophobic amino acids mostly assemble into micelles with the exception of Fmoc M which assembles into fibres with a micelle at the end of each fibre. The nanoparticles interact with these soft structures in varying degrees of order from 3D clusters with Fmoc A to 2D particles with Fmoc V and 1D assemblies in Fmoc L. The trend observed correlates with the length of the side chain. As the side chain length increases, the degree of assembly decreases as does the SERS enhancement.

The hydrophilic amino acids Fmoc S and Fmoc T also form micelles while Fmoc N and Fmoc Q forms fibres. The fibres produced from Fmoc N have a chiral Fmoc core while they are arranged in-plane in Fmoc Q therefore no chirality is observed. The nanoparticles interact with Fmoc S, T and Q while there was a dampening of Fmoc signals in the SERS spectra for Fmoc N with the nanoparticles.

The positively charged amino acids Fmoc D and Fmoc E arranges into micelles. There is a SERS enhancement of the Fmoc moiety with the nanoparticles. The nanoparticles are aggregated on the surface of Fmoc D while they are ordered on the surface of Fmoc E. The negatively charged amino acids Fmoc R arrange into twisted fibres and Fmoc Q into ribbons while Fmoc H arranges into micelles. The nanoparticles did not interact with R or K, but they do interact somewhat with H as there is an increase in the 987 cm^{-1} peak not observed in the other spectrums. The other amino acids C P and G all formed micelles. However, the nanoparticles did not interact with Fmoc P, this was the only micellar structure that the nanoparticles did not interact with. In the presence of nanoparticles Fmoc C

reassembled from micelles to fibres and the nanoparticles also show aggregation, however further work should also be undertaken to understand the mechanism of fibre assembly between the Fmoc C and the PEGylated gold nanoparticles.

All in all, the PEGylated gold nanoparticles interact mostly with the micellar structures with varying degrees of assembly with the exception of Fmoc P. These interactions show that Fmoc can be used as a template for nanoparticle assembly depending on the length and intrinsic properties of the side chain of the amino acid. The presence of nanoparticles appears to inhibit the assembly of fibrous structures by reducing the SERS response however, there is a SERS enhancement observed in Fmoc Q. It would be interesting to see the how these nanoparticles interact with the fibres in TEM or SEM analysis.

For future work, it would also be interesting to observe the photothermal response of nanoparticles assembled onto the micelles and possibly a complete CD analysis of the nanoparticles with the fibrous assemblies of the amino acids.

Preliminary studies were undertaken to observe the changes in interactions between citrate capped 20 nm gold nanoparticles with the assembled Fmoc-monomers. Fmoc E showed the most interesting results (Figure 4.55b). The nanoparticles gradually started to change colour from red to purple then after 6 days of incubation, purple crystals started to form indicating that the nanoparticles are incorporated into the structure. While the nanoparticles in Fmoc D aggregated with no further obvious changes in the sample. However, further analysis will have to be undertaken.

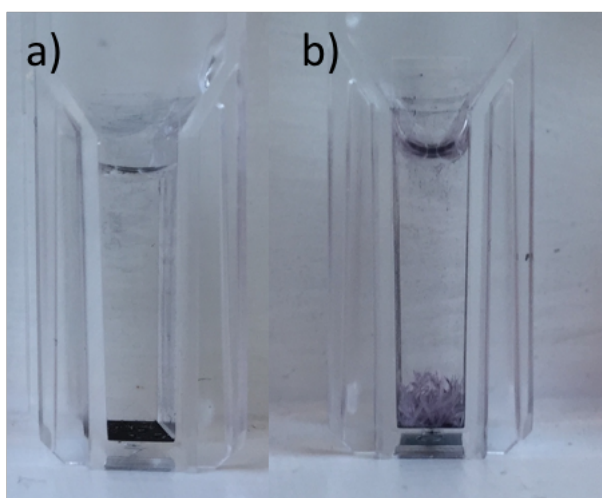


Figure 4.55 Picture taken of a cuvette containing 10 mM of : a) Fmoc D and b) Fmoc E with 1.63 nM 20 nm citrate capped gold nanoparticles in 1 mL, 100 mM pH 8 phosphate buffer after 6 days of incubation

5 Conclusions and Future Work

The aim of this thesis was to produce gold nanoparticle superstructures that have enhanced physiochemical and plasmonic properties for further use in nanomedicine applications. The superstructures prepared would then be used as SERS substrates or in photothermal applications with cells.

Initially in chapter 2, gold supraparticles were formed through a ligand loss method by filtering 40 nm citrate capped gold nanoparticles through a calcium acetate filter with a pore size of 0.2 μm . As the nanoparticles pass through the filter, they would crystallographically realign and rearrange into a supraparticle. This was achieved through a loss of the citrate ligand surrounding the nanoparticle and then a lattice arrangement. The supraparticles had superior SERS properties when comparing them to the 40 nm nanoparticles due to the formation of hotspots within each supraparticle. Furthermore, the supraparticles were further tested for their plasmonic heating properties and it was found that the supraparticles had a 50% greater increase in temperature compared to their individual nanoparticle building blocks. Due to the method of production, the supraparticles were found to be non-toxic to cells. Photothermal experiments with cells proved that the supraparticles were 30% more efficient in killing cancer cells than their nanoparticle constituent.

One challenge of this project was separating out the nanoparticle building blocks from the supraparticles therefore for future work this would be beneficial to find an effective method of size separation without losing a significant amount of the supraparticles. Another significant experiment would be to functionalise the supraparticles with a targeting moiety and test its selectivity *in vivo* with an improved photothermal experiment with a laser in the NIR region.

Further research was conducted into gold nanoparticle assemblies using a template. The first template used was dextran-coated superparamagnetic iron oxide nanoparticles (SPION). The gold nanoparticles were assembled onto this

template by using a positive polymer (PDDA) and additional layers of nanoparticles were created through the same repetition of PDDA/nanoparticle addition causing anisotropic assemblies on the surface. These were aptly named gold suprashells. The gold suprashells had multiple extinction profiles relating to the length of assemblies upon the surface which could be extended into the NIR region. Further tests were conducted into their SERS and photothermal properties. With increasing layers, the suprashells produced well defined SERS spectra of 2-naphthalenethiol however, a plateau is observed between layer 3 and layer 5 in agreement with previous reports which suggest hotspot formation is mainly focussed in the centre of linear assemblies. This property makes the suprashells viable platforms for multiplexing as each additional layer of gold nanoparticle can be functionalised with a targeting agent. The photothermal experiments showed that with each additional layer of gold nanoparticle, there is an increase in change of temperature. Cell studies with the suprashells showed low cytotoxicity and their magnetic properties allowed for easy manipulation which meant that the cells which contained the suprashells could be concentrated then irradiated.

For future work, it would again be beneficial to functionalise the suprashells with targeting moiety to test for their selectivity between cancerous and normal cells, but to also test their viability as theranostic agents. Where DNA could be used in lieu of PDDA and the inner nanoparticle layers could contain a drug whereas the outer layers would contain a targeting moiety. Cancerous cells could therefore be targeted, collected and when irradiated with a laser the DNA strands would dehybridise and expose the drug molecule for treatment of the cells. Future work would also be to improve the photothermal experiments in both the suprashells and supraparticles to include a closed system and continuous monitoring in the system where evaporation would not be a problem.

The last chapter focussed on both molecular self-assembly and nanoparticle self-assembly. Molecular assembly of Fmoc amino acids was first carried out and a full characterisation was undertaken. These assemblies were then used as molecular templates for PEGylated gold nanoparticles. The nanoparticles mostly assembled

around the micellar structures with the exception of Fmoc P and seemed to suppress fibre formation in the Fmoc structures that formed fibres. The nanoparticle assemblies with the hydrophobic amino acids showed that the nanoparticles could be assembled into 1D, 2D and 3D structures depending on the length of side chain which is promising for the use of amino acid assemblies as templates for gold nanoparticles.

For further work it would be beneficial to investigate the nanoparticles interactions with Fmoc C further as there was a conformation change from micelles to fibres was observed and aggregation of the nanoparticles. It would also be interesting to see the direct relationship between citrate capped gold nanoparticles and the soft templates.

It has been shown in this thesis that gold nanoparticle superstructures can be achieved through varying methods of assembly and the superstructures fabricated have enhanced physiochemical properties that can be further used in bio nanomedical applications.

6 References

- 1 G. M. Whitesides and M. Boncheva, *Proc. Natl. Acad. Sci.*, 2002, **99**, 4769–4774.
- 2 G. M. Whitesides and B. Grzybowski, *Sci. (New York, NY)*, 2002, **295**, 2418–2421.
- 3 J. Lankelma, Z. Nie, E. Carrilho and G. M. Whitesides, *Anal. Chem.*, 2012, **84**, 4147–4152.
- 4 Web of Science [v.5.27.2] - Web of Science Core Collection, https://apps.webofknowledge.com/RAMore.do?product=WOS&search_mode=GeneralSearch&SID=C4YaFE6K3LSD3GfVw6i&qid=7&ra_mode=more&ra_name=PublicationYear&colName=WOS&viewType=raMore, (accessed 20 February 2018).
- 5 K. Subramani, A. Khraisat and A. George, *Curr. Nanosci.*, 2008, **4**, 201–207.
- 6 J. Wang, K. Liu, R. Xing and X. Yan, *Chem. Soc. Rev.*, 2016, **45**, 5589–5604.
- 7 C. T. O'Mahony, R. A. Farrell, T. Goshal, J. D. Holmes, M. A. Morris, C. T. O. Mahony, R. A. Farrell, T. Goshal, J. D. Holmes and M. A. Morris, in *Thermodynamics - Systems in Equilibrium and Non-Equilibrium*, ed. J. C. B. T.-T.-S. in E. and N.-E. Moreno-Piraján, InTech, Rijeka, 2011, p. Ch. 13.
- 8 J. W. Steed and J. L. Atwood, *Supramolecular chemistry*, Wiley, 2000.
- 9 J. M. Berg, J. L. Tymoczko and L. Stryer, in *Biochemistry: International Edition*, W H Freeman, 2002.
- 10 J. Emsley, R. J. Parker and R. E. Overill, *J. Chem. Soc. Faraday Trans. 2 Mol. Chem. Phys.*, 1983, **79**, 1347–1353.
- 11 B. Kronberg, *Curr. Opin. Colloid Interface Sci.*, 2016, **22**, 14–22.
- 12 R. W. Siegel, *Nanostructured Materials*, Springer Netherlands, Dordrecht, 1998.
- 13 M. Grzelczak, J. Vermant, E. M. Furst and L. M. Liz-Marzán, *ACS Nano*, 2010, **4**, 3591–3605.
- 14 A. D. Merg, J. C. Boatz, A. Mandal, G. Zhao, S. Mokashi-Punekar, C. Liu, X. Wang, P. Zhang, P. C. A. Van Der Wel and N. L. Rosi, *J. Am. Chem. Soc.*, 2016, **138**, 13655–13663.
- 15 R. Klajn, K. J. M. Bishop and B. A. Grzybowski, *Proc. Natl. Acad. Sci.*, 2007,

- 104**, 10305–10309.
- 16 Z. Nie, A. Petukhova and E. Kumacheva, *Nat. Nanotechnol.*, 2010, **5**, 15–25.
- 17 P. M. Tiwari, K. Vig, V. a. Dennis and S. R. Singh, *Nanomaterials*, 2011, **1**, 31–63.
- 18 J. Liu and Y. Lu, *J. Fluoresc.*, 2004, **14**, 343–354.
- 19 Z. Zhan, X. Ma, C. Cao and S. J. Sim, *Biosens. Bioelectron.*, 2012, **32**, 127–132.
- 20 M. E. Napier and J. M. Desimone, *Polym. Rev.*, 2007, **47**, 321–327.
- 21 W. H. De Jong and P. J. a Borm, *Int. J. Nanomedicine*, 2008, **3**, 133–149.
- 22 R. S. Gill, R. F. Saraf and S. Kundu, *ACS Appl. Mater. Interfaces*, 2013, **5**, 9949–9956.
- 23 C. a Mirkin, R. L. Letsinger, R. C. Mucic and J. J. Storhoff, *Nature*, 1996, 382, 607–609.
- 24 S. Y. Park, A. K. R. Lytton-Jean, B. Lee, S. Weigand, G. C. Schatz and C. A. Mirkin, *Nature*, 2008, **451**, 553–556.
- 25 D. Nykypanchuk, M. M. Maye, D. Van Der Lelie and O. Gang, *Nature*, 2008, **451**, 549–552.
- 26 Y. Tian, Y. Zhang, T. Wang, H. L. Xin, H. Li and O. Gang, *Nat. Mater.*, 2016, **15**, 654–661.
- 27 R. Schreiber, N. Luong, Z. Fan, A. Kuzyk, P. C. Nickels, T. Zhang, D. M. Smith, B. Yurke, W. Kuang, A. O. Govorov and T. Liedl, *Nat. Commun.*, 2013, **4**, 2948.
- 28 B. Teschome, S. Facsko, K. V. Gothelf and A. Keller, *Langmuir*, 2015, **31**, 12823–12829.
- 29 R. Schreiber, I. Santiago, A. Ardavan and A. J. Turberfield, *ACS Nano*, 2016, **10**, 7303–7306.
- 30 P. Wang, T. A. Meyer, V. Pan, P. K. Dutta and Y. Ke, *Chem*, 2017, **2**, 359–382.
- 31 K. V. Gothelf and T. Tørring, *F1000Prime Rep.*, 2013, **5**, 1–4.
- 32 L. Bin Zhong, J. Yin, Y. M. Zheng, Q. Liu, X. X. Cheng and F. H. Luo, *Anal. Chem.*, 2014, **86**, 6262–6267.
- 33 M. A. Correa-Duarte and L. M. Liz-Marzán, *J. Mater. Chem.*, 2006, **16**, 22–25.
- 34 L. C. Palmer and S. I. Stupp, *Acc. Chem. Res.*, 2008, **41**, 1674–1684.
- 35 D. Liu, F. Zhou, C. Li, T. Zhang, H. Zhang, W. Cai and Y. Li, *Angew. Chemie - Int. Ed.*, 2015, **54**, 9596–9600.
- 36 B. Liu, M. Louis, L. Jin, G. Li and J. He, *Chem. - A Eur. J.*, 2018, **11**, 1114–1120.

- 37 T. Chen, M. Pourmand, A. Feizpour, B. Cushman and B. M. Reinhard, *J. Phys. Chem. Lett.*, 2013, **4**, 2147–2152.
- 38 S. R. Ahmed, J. Kim, V. T. Tran, T. Suzuki, S. Neethirajan, J. Lee and E. Y. Park, *Sci. Rep.*, 2017, **7**, 1–11.
- 39 M. A. Olson, A. Coskun, R. Klajn, L. Fang, S. K. Dey, K. P. Browne, B. A. Grzybowski and J. F. Stoddart, *Nano Lett.*, 2009, **9**, 3185–3190.
- 40 R. Kaminker, M. Lahav, L. Motiei, M. Vartanian, R. Popovitz-Biro, M. A. Iron and M. E. Van Der Boom, *Angew. Chemie - Int. Ed.*, 2010, **49**, 1218–1221.
- 41 D. S. Sidhaye, S. Kashyap, M. Sastry, S. Hotha and B. L. V. Prasad, *Langmuir*, 2005, **21**, 7979–7984.
- 42 B. I. Ipe, S. Mahima and K. G. Thomas, *J. Am. Chem. Soc.*, 2003, **125**, 7174–7175.
- 43 B. Y. Kim, I. B. Shim, O. L. A. Monti and J. Pyun, *Chem. Commun.*, 2011, **47**, 890–892.
- 44 C. H. Wu, J. Cook, S. Emelianov and K. Sokolov, *Adv. Funct. Mater.*, 2014, **24**, 6862–6871.
- 45 B. P. Binks, *Curr. Opin. Colloid Interface Sci.*, 2002, **7**, 21–41.
- 46 J. Tian, L. Yuan, M. Zhang, F. Zheng, Q. Xiong and H. Zhao, *Langmuir*, 2012, **28**, 9365–9371.
- 47 J. P. J. P. Coelho, M. J. M. J. Mayoral, L. Camacho, M. T. Martín-Romero, G. Tardajos, I. López-Montero, E. Sanz, D. Ávila-Brandé, J. J. J. Giner-Casares, G. Fernández, A. Guerrero-Martínez, D. Avila Brandé, J. J. J. Giner-Casares, G. Fernández and A. Guerrero-Martínez, *J. Am. Chem. Soc.*, 2016, **139**, jacs.6b09485.
- 48 L. Olofsson, T. Rindzevicius, I. Pfeiffer, M. Käll and F. Höök, *Langmuir*, 2003, **19**, 10414–10419.
- 49 J. J. Armao, I. Nyrkova, G. Fuks, A. Osypenko, M. Maaloum, E. Moulin, R. Arenal, O. Gavat, A. N. Semenov and N. Giuseppone, *J. Am. Chem. Soc.*, 2017, jacs.6b11179.
- 50 Z. Yang, T. Altantzis, D. Zanaga, S. Bals, G. Van Tendeloo and M. P. Pileni, *J. Am. Chem. Soc.*, 2016, **138**, 3493–3500.
- 51 H. Y. Lee, S. H. R. Shin, A. M. Drews, A. M. Chirsan, S. A. Lewis and K. J. M. Bishop, *ACS Nano*, 2014, **8**, 9979–9987.

- 52 A. Mocanu, I. Cernica, G. Tomoaia, L. D. Bobos, O. Horovitz and M. Tomoaia-Cotisel, *Colloids Surfaces A Physicochem. Eng. Asp.*, 2009, **338**, 93–101.
- 53 S. Zhang, X. Kou, Z. Yang, Q. Shi, G. D. Stucky, L. Sun, J. Wang and C. Yan, *Chem. Commun.*, 2007, 1816–1818.
- 54 P. B. Tchounwou, W. K. Ayensu, N. Ninashvili and D. Sutton, *Environ. Toxicol.*, 2003, **18**, 149–75.
- 55 W. C. Li and S. W. Lee, *Curr. Appl. Phys.*, 2012, **12**, 1361–1365.
- 56 K. L. Gurunatha, A. C. Fournier, A. Urvoas, M. Valerio-Lepiniec, V. Marchi, P. Minard and E. Dujardin, *ACS Nano*, 2016, **10**, 3176–3185.
- 57 R. De La Rica, *Nanoscale*, 2017, **9**, 18855–18860.
- 58 R. D'Agata, P. Palladino and G. Spoto, *Beilstein J. Nanotechnol.*, 2017, **8**, 1–11.
- 59 P. Kaur, Y. Maeda, A. C. Mutter, T. Matsunaga, Y. Xu and H. Matsui, *Angew. Chemie - Int. Ed.*, 2010, **49**, 8375–8378.
- 60 J. R. Waldeisen, T. Wang, B. M. Ross and L. P. Lee, *ACS Nano*, 2011, **5**, 5383–9.
- 61 A. Arakaki, S. Hideshima, T. Nakagawa, D. Niwa, T. Tanaka, T. Matsunaga and T. Osaka, *Biotechnol. Bioeng.*, 2004, **88**, 543–546.
- 62 K. Lee and M. a El-sayed, *J. Phys. Chem. B*, 2006, 19220–19225.
- 63 P. Mulvaney, *Langmuir*, 1996, **12**, 788–800.
- 64 M. Cordeiro, F. F. Carlos, P. Pedrosa, A. Lopez and P. V. Baptista, *Diagnostics*, , DOI:10.3390/diagnostics6040043.
- 65 J. Polte, *CrystEngComm*, , DOI:10.1039/C5CE01014D.
- 66 I. Tokarev and S. Minko, *Soft Matter*, 2012, **8**, 5980.
- 67 W. Hergert and T. Wriedt, *Mie Theory Basics Appl.*, 2012, **169**, i–xiv.
- 68 K. Nakamura, T. Kawabata and Y. Mori, *Powder Technol.*, 2003, **131**, 120–128.
- 69 S. Link and M. A. El-Sayed, *J. Phys. Chem. B*, 1999, **103**, 4212–4217.
- 70 J. Kimling, M. Maier, V. Okenve, V. Kotaidis, H. Ballot, a Plech and B. Okenve, *J. Phys. Chem. B*, 2006, **110**, 15700–15707.
- 71 M. Wuithschick, A. Birnbaum, S. Witte, M. Sztucki, U. Vainio, N. Pinna, K. Rademann, F. Emmerling, R. Kraehnert and J. Polte, *ACS Nano*, 2015, **9**, 150706092247000.
- 72 J. Turkevich, G. Garton and P. C. Stevenson, *J. Colloid Sci.*, 1954, **9**, 26–35.

- 73 R. S. Krishnan and R. K. Shankar, *J. Raman Spectrosc.*, 1981, **10**, 1–8.
- 74 P. J. Larkin, *Infrared and Raman Spectroscopy: Principles and Spectral Interpretation*, 2011.
- 75 E. W. Smith and G. Dent, in *Journal of Raman Spectroscopy*, John Wiley & Sons, 2005, vol. 36, pp. 835–835.
- 76 A. Otto, *Stud. Surf. Sci. Catal.*, 1983, **14**, 329–342.
- 77 E. Petryayeva and U. J. Krull, *Anal. Chim. Acta*, 2011, **706**, 8–24.
- 78 J. P. Scaffidi, M. K. Gregas, V. Seewaldt and T. Vo-Dinh, *Anal. Bioanal. Chem.*, 2009, **393**, 1135–1141.
- 79 S. G. Patching, *Biochim. Biophys. Acta*, 2014, **1838**, 43–55.
- 80 J. Kneipp, H. Kneipp, M. McLaughlin, D. Brown and K. Kneipp, *Nano Lett.*, 2006, **6**, 2225–2231.
- 81 A. McLintock, C. A. Cunha-Matos, M. Zagnoni, O. R. Millington and A. W. Wark, *ACS Nano*, 2014, **8**, 8600–8609.
- 82 W. R. Premasiri, D. T. Moir, M. S. Klempner, N. Krieger, G. Jones and L. D. Ziegler, *J. Phys. Chem. B*, 2005, **109**, 312–320.
- 83 G. R. Souza, D. R. Christianson, F. I. Staquicini, M. G. Ozawa, E. Y. Snyder, R. L. Sidman, J. H. Miller, W. Arap and R. Pasqualini, *Proc. Natl. Acad. Sci. U. S. A.*, 2006, **103**, 1215–1220.
- 84 S. Link and M. A. El-Sayed, *Int. Rev. Phys. Chem.*, 2000, **19**, 409–453.
- 85 X. Huang and M. A. El-Sayed, *J. Adv. Res.*, 2010, **1**, 13–28.
- 86 H. Zakaria, W. S. Abdelaziz and T. Youssef, *Lasers Med. Sci.*, 2016, **31**, 625–634.
- 87 B. Khlebtsov, V. Zharov, A. Melnikov, V. Tuchin and N. Khlebtsov, *Nanotechnology*, 2006, **17**, 5167–5179.
- 88 J. Sharma, R. Chhabra, H. Yan and Y. Liu, *Chem. Commun. (Camb)*, 2007, **9**, 477–9.
- 89 S.-E. Kim, B.-R. Lee, H. Lee, S. D. Jo, H. Kim, Y.-Y. Won and J. Lee, *Sci. Rep.*, 2017, **7**, 17327.
- 90 K. Saha, S. S. Agasti, C. Kim, X. Li and V. M. Rotello, *Chem. Rev.*, 2012, **112**, 2739–2779.
- 91 R. A. Sperling, P. R. Gil, F. Zhang, M. Zanella and W. J. Parak, *Chem. Soc. Rev.*, 2008, 1896–1908.

- 92 T. Abdallah, T. A. El-Brolosy, M. B. Mohamed, K. Easawi, S. Negm and H. Talaat, *J. Raman Spectrosc.*, 2012, **43**, 1924–1930.
- 93 H. Zakaria, W. S. Abdelaziz and T. Youssef, *Lasers Med. Sci.*, 2016, **31**, 625–634.
- 94 T. Dreifuss, E. Barnoy, M. Motiei and R. Popovtzer, in *Design and Applications of Nanoparticles in Biomedical Imaging*, Springer International Publishing, Cham, 2016, pp. 403–427.
- 95 C. W. Liao, Y. S. Lin, K. Chanda, Y. F. Song and M. H. Huang, *J. Am. Chem. Soc.*, 2013, **135**, 2684–2693.
- 96 E. V. Sturm (née Rosseeva) and H. Cölfen, *Chem. Soc. Rev.*, 2016, **45**, 5821–5833.
- 97 H. Cölfen and M. Antonietti, *Angew. Chemie - Int. Ed.*, 2005, **44**, 5576–5591.
- 98 L. Liu, D. He, G. S. Wang and S. H. Yu, *Langmuir*, 2011, **27**, 7199–7206.
- 99 A. W. Xu, M. Antonietti, H. Cölfen and Y. P. Fang, *Adv. Funct. Mater.*, 2006, **16**, 903–908.
- 100 K. S. Louis and A. C. Siegel, 2011, **740**, 7–12.
- 101 W. Haiss, N. T. K. Thanh, J. Aveyard and D. G. Fernig, *Anal. Chem.*, 2007, **79**, 4215–4221.
- 102 J. Park, K. An, Y. Hwang, J. E. G. Park, H. J. Noh, J. Y. Kim, J. H. Park, N. M. Hwang and T. Hyeon, *Nat. Mater.*, 2004, **3**, 891–895.
- 103 S. Stankovich, D. A. Dikin, G. H. B. Dommett, K. M. Kohlhaas, E. J. Zimney, E. A. Stach, R. D. Piner, S. B. T. Nguyen and R. S. Ruoff, *Nature*, 2006, **442**, 282–286.
- 104 N. G. Bastús, J. Comenge and V. Puntes, *Langmuir*, 2011, **27**, 11098–11105.
- 105 S. Volden, K. Zhu, B. Nyström and W. R. Glomm, *Colloids Surfaces B Biointerfaces*, 2009, **72**, 266–271.
- 106 N. Sosibo, P. Mdluli, P. Mashazi, R. Tshikhudo, A. Skepu, S. Vilakazi and T. Nyokong, *Mater. Lett.*, 2012, **88**, 132–135.
- 107 G. P. Sahoo, D. K. Bhui, H. Bar, P. Sarkar, S. Samanta, S. Pyne and A. Misra, *J. Mol. Liq.*, 2010, **155**, 91–95.
- 108 H. Yao, C. Yi, C.-H. Tzang, J. Zhu and M. Yang, *Nanotechnology*, 2006, **18**, 015102.
- 109 Y. H. Ngo, D. Li, G. P. Simon and G. Garnier, *Langmuir*, 2012, **28**, 8782–8790.

- 110 Z. Quan, H. Xu, C. Wang, X. Wen, Y. Wang, J. Zhu, R. Li, C. J. Sheehan, Z. Wang, D. M. Smilgies, Z. Luo and J. Fang, *J. Am. Chem. Soc.*, 2014, **136**, 1352–1359.
- 111 R. Li, J. Zhang, R. Tan, F. Gerdes, Z. Luo, H. Xu, J. A. Hollingsworth, C. Klinke, O. Chen and Z. Wang, *Nano Lett.*, 2016, **16**, 2792–2799.
- 112 F. Li, D. P. Josephson and A. Stein, *Angew. Chemie - Int. Ed.*, 2011, **50**, 360–388.
- 113 P. F. Damasceno, M. Engel and S. C. Glotzer, *Science (80-.)*, 2012, **337**, 453–457.
- 114 J. Xu, Y. Wang, X. Qi, C. Liu, J. He, H. Zhang and H. Chen, *Angew. Chemie - Int. Ed.*, 2013, **52**, 6019–6023.
- 115 C. Lu and Z. Tang, *Adv. Mater.*, 2016, **28**, 1096–1108.
- 116 S. E. J. Bell and N. M. S. Sirimuthu, *J. Phys. Chem. A*, 2005, **109**, 7405–7410.
- 117 K. Thorkelsson, P. Bai and T. Xu, *Nano Today*, 2015, **10**, 48–66.
- 118 T. A. Henderson and L. Morries, *Neuropsychiatr. Dis. Treat.*, 2015, **11**, 2191.
- 119 A. M. Smith, M. C. Mancini and S. Nie, *Nat. Nanotechnol.*, 2009, **4**, 710–711.
- 120 J. S. Donner, S. A. Thompson, M. P. Kreuzer, G. Baffou and R. Quidant, *Nano Lett.*, 2012, **12**, 2107–2111.
- 121 C. Loo, A. Lowery, N. Halas, J. West and R. Drezek, *Nano Lett.*, 2005, **5**, 709–711.
- 122 X. Huang, I. H. El-Sayed, W. Qian and M. A. El-Sayed, *J. Am. Chem. Soc.*, 2006, **128**, 2115–2120.
- 123 J. S. Donner, S. A. Thompson, C. Alonso-Ortega, J. Morales, L. G. Rico, S. I. C. O. Santos and R. Quidant, *ACS Nano*, 2013, **7**, 8666–8672.
- 124 J. R. Cole, N. A. Mirin, M. W. Knight, G. P. Goodrich and N. J. Halas, *J. Phys. Chem. C*, 2009, **113**, 12090–12094.
- 125 M. Yu and J. Zheng, *ACS Nano*, 2015, **9**, 6655–6674.
- 126 Y. Yang, S. Matsubara, M. Nogami, J. Shi and W. Huang, *Nanotechnology*, 2006, **17**, 2821–2827.
- 127 M. F. Tsai, S. H. G. Chang, F. Y. Cheng, V. Shanmugam, Y. S. Cheng, C. H. Su and C. S. Yeh, *ACS Nano*, 2013, **7**, 5330–5342.
- 128 L. L. Ma, M. D. Feldman, J. M. Tam, A. S. Paranjape, K. K. Cheruku, T. A. Larson, J. O. Tam, D. R. Ingram, V. Paramita, J. W. Villard, J. T. Jenkins, T. Wang, G. D. Clarke, R. Asmis, K. Sokolov, B. Chandrasekar, T. E. Milner and K. P. Johnston,

- ACS Nano*, 2009, **3**, 2686–2696.
- 129 N. J. Halas, S. Lal, W. S. Chang, S. Link and P. Nordlander, *Chem. Rev.*, 2011, **111**, 3913–3961.
- 130 P. Senthil Kumar, I. Pastoriza-Santos, B. Rodríguez-González, F. Javier García De Abajo and L. M. Liz-Marzán, *Nanotechnology*, 2008, **19**, 015606.
- 131 L. Zhang, H. Chang, A. Hirata, H. Wu, Q. K. Xue and M. Chen, *ACS Nano*, 2013, **7**, 4595–4600.
- 132 G. Baffou and R. Quidant, *Laser Photonics Rev.*, 2013, **7**, 171–187.
- 133 C. Tira, D. Tira, T. Simon and S. Astilean, *J. Mol. Struct.*, 2014, **1072**, 137–143.
- 134 L. Guo, A. R. Ferhan, H. Chen, C. Li, G. Chen, S. Hong and D. H. Kim, *Small*, 2013, **9**, 234–240.
- 135 W.-S. Chang, B. A. Willingham, L. S. Slaughter, B. P. Khanal, L. Vigderman, E. R. Zubarev and S. Link, *Proc. Natl. Acad. Sci.*, 2011, **108**, 19879–19884.
- 136 H. Zhang and D. Wang, *Angew. Chemie - Int. Ed.*, 2008, **47**, 3984–3987.
- 137 Z. Yin, W. Zhang, Q. Fu, H. Yue, W. Wei, P. Tang, W. Li, W. Li, L. Lin, G. Ma and D. Ma, *Small*, 2014, **10**, 3619–3624.
- 138 Z. Fan, M. Shelton, A. K. Singh, D. Senapati, S. A. Khan and P. C. Ray, *ACS Nano*, 2012, **6**, 1065–1073.
- 139 I. Y. Goon, L. M. H. Lai, M. Lim, P. Munroe, J. J. Gooding and R. Amal, *Chem. Mater.*, 2009, **21**, 673–681.
- 140 C. S. Levin, C. Hofmann, T. a Ali, a T. Kelly, E. Morosan, P. Nordlander, K. H. Whitmire and N. J. Halas, *ACS Nano*, 2009, **3**, 1379–1388.
- 141 C. Li, T. Chen, I. Ocsoy, G. Zhu, E. Yasun, M. You, C. Wu, J. Zheng, E. Song, C. Z. Huang and W. Tan, *Adv. Funct. Mater.*, 2014, **24**, 1772–1780.
- 142 S. Yu, J. A. Hachtel, M. F. Chisholm, S. T. Pantelides, A. Laromaine and A. Roig, *Nanoscale*, 2015, **7**, 14039–46.
- 143 P. A. Mosier-Boss and M. D. Putnam, *Anal. Chem. Insights*, 2013, **8**, 83–97.
- 144 L. Wu, C. Shi, L. Tian and J. Zhu, *J. Phys. Chem. C*, 2008, **112**, 319–323.
- 145 A. S. Urban, X. Shen, Y. Wang, N. Large, H. Wang, M. W. Knight, P. Nordlander, H. Chen and N. J. Halas, *Nano Lett.*, 2013, **13**, 4399–4403.
- 146 E. K. Payne, K. L. Shuford, S. Park, G. Schatz and C. A. Mirkin, *J. Phys. Chem. B*, 2006, **110**, 2150–2154.
- 147 N. G. Bastús, J. Piella and V. Puntes, *Langmuir*, 2016, **32**, 290–300.

- 148 R. A. Alvarez-Puebla and R. F. Aroca, *Anal. Chem.*, 2009, **81**, 2280–2285.
- 149 S. L. Kleinman, B. Sharma, M. G. Blaber, A. I. Henry, N. Valley, R. G. Freeman, M. J. Natan, G. C. Schatz and R. P. Van Duyne, *J. Am. Chem. Soc.*, 2013, **135**, 301–308.
- 150 Z. B. Wang, B. S. Luk'yanchuk, W. Guo, S. P. Edwardson, D. J. Whitehead, L. Li, Z. Liu and K. G. Watkins, *J. Chem. Phys.*, 2008, **128**, 094705.
- 151 P. S. Popp, J. F. Herrmann, E.-C. Fritz, B. J. Ravoo and C. Höppener, *Small*, 2016, **12**, 1667–1675.
- 152 G. Baffou, R. Quidant and F. J. García de Abajo, *ACS Nano*, 2010, **4**, 709–716.
- 153 C. L. Baldwin, N. W. Bigelow and D. J. Masiello, *J. Phys. Chem. Lett.*, 2014, **5**, 1347–1354.
- 154 C. Bayarri-Lara, F. G. Ortega, A. Cueto Ladrón de Guevara, J. L. Puche, J. Ruiz Zafra, D. de Miguel-Pérez, A. S.-P. Ramos, C. F. Giraldo-Ospina, J. A. Navajas Gómez, M. Delgado-Rodríguez, J. A. Lorente and M. J. Serrano, *PLoS One*, 2016, **11**, e0148659.
- 155 C. S. Hall, M. Karhade, B. A. Laubacher, H. M. Kuerer, S. Krishnamurthy, S. DeSnyder, A. E. Anderson, V. Valero, N. T. Ueno, L. Yisheng, S. Xiao and A. Lucci, *J. Natl. Cancer Inst.*, 2015, **107**, djv250.
- 156 H. J. Yoon, M. Kozminsky and S. Nagrath, *ACS Nano*, 2014, **8**, 1995–2017.
- 157 S. R. Chavva, A. Pramanik, B. P. V. Nellore, S. S. Sinha, B. Yust, R. Kanchanapally, Z. Fan, R. A. Crouch, A. K. Singh, B. Neyland, K. Robinson, X. Dai, D. Sardar, Y. Lu and P. C. Ray, *Part. Part. Syst. Charact.*, 2014, **31**, 1252–1259.
- 158 A. Huefner, W. L. Kuan, K. H. Müller, J. N. Skepper, R. a. Barker and S. Mahajan, *ACS Nano*, 2016, **10**, 307–316.
- 159 S. Pronk, S. Páll, R. Schulz, P. Larsson, P. Bjelkmar, R. Apostolov, M. R. Shirts, J. C. Smith, P. M. Kasson, D. van der Spoel, B. Hess and E. Lindahl, *Bioinformatics*, 2013, **29**, 845–854.
- 160 F. Wo, R. Xu, Y. Shao, Z. Zhang, M. Chu, D. Shi and S. Liu, *Theranostics*, 2016, **6**, 485–500.
- 161 A. Pallaoro, M. R. Hoonejani, G. B. Braun, C. D. Meinhart and M. Moskovits, *ACS Nano*, 2015, **9**, 4328–4336.
- 162 S. Fleming and R. V. Ulijn, *Chem. Soc. Rev.*, 2014, **43**, 8150–8177.

- 163 C. N. Pace, G. R. Grimsley and J. M. Scholtz, *J. Biol. Chem.*, 2009, **284**, 13285–13289.
- 164 C. P. Shaw, D. G. Fernig and R. Lévy, *J. Mater. Chem.*, 2011, **21**, 12181.
- 165 E. Piccinini, D. Pallarola, F. Battaglini and O. Azzaroni, *Mol. Syst. Des. Eng.*, 2016, **1**, 155–162.
- 166 R. J. Macfarlane, B. Lee, M. R. Jones, N. Harris, G. C. Schatz and C. A. Mirkin, *Science*, 2011, **334**, 204–8.
- 167 J. J. Storhoff, R. Elghanian, R. C. Mucic, C. A. Mirkin and R. L. Letsinger, *J. Am. Chem. Soc.*, 1998, **120**, 1959–1964.
- 168 D. J. Park, C. Zhang, J. C. Ku, Y. Zhou, G. C. Schatz and C. A. Mirkin, *Proc. Natl. Acad. Sci. U. S. A.*, 2015, **112**, 977–81.
- 169 A. M. Hung, C. M. Micheel, L. D. Bozano, L. W. Osterbur, G. M. Wallraff and J. N. Cha, *Nat Nanotechnol*, 2010, **5**, 121–126.
- 170 J. Sharma, R. Chhabra, A. Cheng, J. Brownell, Y. Liu and H. Yan, *Science (80-)*, 2009, **323**, 112–116.
- 171 M. J. Abraham, T. Murtola, R. Schulz, S. Páll, J. C. Smith, B. Hess and E. Lindahl, *SoftwareX*, 2015, **1–2**, 19–25.
- 172 S. Pronk, S. Páll, R. Schulz, P. Larsson, P. Bjelkmar, R. Apostolov, M. R. Shirts, J. C. Smith, P. M. Kasson, D. Van Der Spoel, B. Hess and E. Lindahl, *Bioinformatics*, 2013, **29**, 845–854.
- 173 L. Monticelli, S. K. Kandasamy, X. Periole, R. G. Larson, D. P. Tieleman and S. J. Marrink, *J. Chem. Theory Comput.*, 2008, **4**, 819–834.
- 174 E. R. Draper, K. L. Morris, M. A. Little, J. Raeburn, C. Colquhoun, E. R. Cross, T. O. McDonald, L. C. Serpell and D. J. Adams, *CrystEngComm*, 2015, **17**, 8047–8057.
- 175 X. Wang, T. Zeng, M. Nourrein, B.-H. Lai, K. Shen, C.-L. Wang, B. Sun and M. Zhu, *RSC Adv.*, 2017, **7**, 26074–26081.
- 176 V. Singh, K. Snigdha, C. Singh, N. Sinha and A. K. Thakur, *Soft Matter*, 2015, **11**, 5353–5364.
- 177 K. Tao, A. Levin, L. Adler-Abramovich and E. Gazit, *Chem. Soc. Rev.*, 2016, **45**, 3935–3953.
- 178 C. Bhattacharjee, S. Saha, A. Biswas, M. Kundu, L. Ghosh and K. P. Das, *Protein J.*, 2005, **24**, 27–35.

- 179 M. Malferrari, G. Venturoli, F. Francia and A. Mezzetti, *Spectrosc. An Int. J.*, 2012, **27**, 337–342.
- 180 S. Fleming, P. W. J. M. Frederix, I. Ramos Sasselli, N. T. Hunt, R. V. Ulijn and T. Tuttle, *Langmuir*, 2013, **29**, 9510–9515.
- 181 Z. Gu, R. Zambrano and A. McDermott, *J. Am. Chem. Soc.*, 1994, **116**, 6368–6372.
- 182 D. G. Babar and S. Sarkar, *Appl. Nanosci.*, 2017, **7**, 101–107.
- 183 K. Thornton, Y. M. Abul-Haija, N. Hodson and R. V. Ulijn, *Soft Matter*, 2013, **9**, 9430.
- 184 N. Amdursky and M. M. Stevens, *ChemPhysChem*, 2015, **16**, 2768–2774.
- 185 J. M. Antosiewicz and D. Shugar, *Biophys. Rev.*, 2016, **8**, 163–177.
- 186 A. Rajbhandary, W. W. Brennessel and B. L. Nilsson, *Cryst. Growth Des.*, 2018, **18**, 623–632.
- 187 Z. Yang and B. Xu, *Chem. Commun.*, 2004, **1**, 2424.
- 188 A. M. Smith, R. F. Collins, R. V. Ulijn and E. Blanch, *J. Raman Spectrosc.*, 2009, **40**, 1093–1095.
- 189 B. D. Larsen, D. H. Christensen, R. Zillmer, O. F. Nielsen and A. Holm, *J. Am. Chem. Soc.*, 1993, **115**, 6247–6253.
- 190 A. L. Jenkins, R. A. Larsen and T. B. Williams, *Spectrochim. Acta Part A Mol. Biomol. Spectrosc.*, 2005, **61**, 1585–1594.
- 191 K. M. Eckes, X. Mu, M. A. Ruehle, P. Ren and L. J. Suggs, *Langmuir*, 2014, **30**, 5287–5296.
- 192 C. G. Pappas, R. Shafi, I. R. Sasselli, H. Siccardi, T. Wang, V. Narang, R. Abzalimov, N. Wijerathne and R. V. Ulijn, *Nat. Nanotechnol.*, 2016, **11**, 1–9.
- 193 E. V. Alakpa, V. Jayawarna, A. Lampel, K. V. Burgess, C. C. West, S. C. J. Bakker, S. Roy, N. Javid, S. Fleming, D. A. Lamprou, J. Yang, A. Miller, A. J. Urquhart, P. W. J. M. Frederix, N. T. Hunt, B. Péault, R. V. Ulijn and M. J. Dalby, *Chem*, 2016, **1**, 512.
- 194 E. V. Alakpa, V. Jayawarna, A. Lampel, B. Pé, R. V. Ulijn and M. J. Dalby, *Chem*, 2016, **1**, 298–319.
- 195 J. Casado, J. T. L. Navarrete and F. J. Ramírez, *J. Raman Spectrosc.*, 1995, **26**, 1003–1008.
- 196 E. I. Kamitsos, in *Modern Glass Characterization*, John Wiley & Sons, Inc.,

- Hoboken, NJ, USA, 2015, vol. 47405, pp. 32–73.
- 197 A. Barth, *Biochim. Biophys. Acta - Bioenerg.*, 2007, **1767**, 1073–1101.
- 198 A. Ghosh, M. J. Tucker and F. Gai, *J. Phys. Chem. B*, 2014, **118**, 7799–7805.
- 199 A. Barth, *Prog. Biophys. Mol. Biol.*, 2000, **74**, 141–173.